Site-Resolved Imaging with the Fermi Gas Microscope

Site-Resolved Imaging with the Fermi Gas Microscope

A dissertation presented

by

Florian Gerhard Huber

to

The Department of Physics

in partial fulfillment of the requirements

for the degree of

Doctor of Philosophy

in the subject of

Physics

Harvard University

Cambridge, Massachusetts

May 2014

Dissertation Advisor:
Professor Markus Greiner

Author:
Florian Gerhard Huber

Site-Resolved Imaging with the Fermi Gas Microscope

Abstract

The recent development of quantum gas microscopy for bosonic rubidium atoms trapped in optical lattices has made it possible to study local structure and correlations in quantum many-body systems. Quantum gas microscopes are a perfect platform to perform quantum simulation of condensed matter systems, offering unprecedented control over both internal and external degrees of freedom at a single-site level. In this thesis, this technique is extended to fermionic particles, paving the way to fermionic quantum simulation, which emulate electrons in real solids.

Our implementation uses lithium, the lightest atom amenable to laser cooling. The absolute timescales of dynamics in optical lattices are inversely proportional to the mass. Therefore, experiments are more than six times faster than for the only other fermionic alkali atom, potassium, and more then fourteen times faster than an equivalent rubidium experiment.

Scattering and collecting a sufficient number of photons with our high-resolution imaging system requires continuous cooling of the atoms during the fluorescence imaging. The lack of a resolved excited hyperfine structure on the D2 line of lithium prevents efficient conventional sub-Doppler cooling. To address this challenge we have applied a Raman sideband cooling scheme and achieved the first site-resolved imaging of ultracold fermions in an optical lattice.

Contents

List of Figures

Acknowledgments

I would like to express my gratitude to my advisor Prof. Markus Greiner. Thank you giving me enough freedom to design an experiment according to my own ideas, while still bringing up interesting ideas and being available for discussions at any time.

I also want to thank my thesis committee with Prof. Misha Lukin, Prof. John Doyle, and especially Prof. Ron Walsworth, who made him self available to provide his support during my thesis defense.

Although mostly in the background, would like to express my deepest appreciation to the Harvard physics staff: to Stan Cotreau for teaching me proper machining, to Steve Sansone for teaching me the other machining tricks, to Jim MacArthur for insightful discussions about frequency synthesizers, to Stuart McNeil for keeping everyone entertained with crazy construction projects around the lab, and the janitor Manny for helping me out countless times when I had locked myself out of the lab.

At the time I joined Markus's group the lithium experiment was pretty much a blank slate. Widagdo Setiawan taught me countless things required to build and run such a complex experiment as the Fermi gas microscope. I am indebt for your guidance and patience. The lithium lab would not be where it is today without your influence.

I am also deeply grateful to my coworkers Max Parsons and our postdoc Sebastian Blatt for meticulously proofreading my "rough" thesis and teaching my about topic sentences.

I wish the next generation of very talented graduate students on the lithium experiment best of luck. I am convinced that Max Parsons, Anton Mazurenko, and Christie Chiu are going to study exciting physics with the Fermi gas microscope.

Special thanks also to the former members of the lithium lab, Kate Wooley-Brown and Dylan Cotta, and members of the rubidium quantum gas microscope experiment: Jonathon Gillen, Waseem Bakr, Amy Peng, Eric Tai, Ruichao Ma, Alex Lukin, Matthew Rispoli, Philip Zupancic, and their postdocs Simon Fölling, Jon Simon, and Rajibul Islam. Without you all the Greiner Lab "WG" would have been incomplete. It was always a pleasure to work with you in our tiny office with more than ten students cramped in-between oversized computer

monitors, boxes of lab snacks, and “McMaster surprises”.

In addition, I would like to thank my friends who kept me busy outside the lab: Rob Kassner, Chris “The German Dude” Freudiger, Matthew Freemont, Niklas Jepsen, Garrett Drayna, Eric Tai, Kate Wooley-Brown, Jon Simon, and Maggie Powers.

To my parents

Introduction

Many open questions in physics stem from the quantum nature of matter. Although theoretical models might exist for a particular physical system, it may not be computationally feasible to solve the models on a classical computer due to the complexity of quantum many-body problems.

To illustrate this complexity consider a one-dimensional chain of N $\uparrow$ and $\downarrow$ spins. For classical spins any state can be described as a tuple of spins, for example

$$\mathbf{c} = (\ldots, \uparrow, \downarrow, \ldots) .$$

In total there are $|\Omega_{\mathrm{cl}}| = 2^N$ possible configurations $\mathbf{c} \in \Omega_{\mathrm{cl}}$. Each configuration can be described with just N parameters $(\mathbf{c})_i \in \{\downarrow, \uparrow\}$. Even the state space of the classical problem has exponential scaling in the number of particles N. For the same problem with quantum spins an arbitrary state can be written as a *quantum superposition* of classical basis states, for example

$$\left|\Psi_{\mathrm{qm}}\right\rangle = c_0 \left|\downarrow, \downarrow, \ldots\right\rangle + c_1 \left|\downarrow, \uparrow, \ldots\right\rangle + c_2 \left|\downarrow, \uparrow, \ldots\right\rangle + c_3 \left|\uparrow, \uparrow, \ldots\right\rangle + \ldots$$

Because of the *entanglement*, $2^N - 1$ parameters are needed to describe a single state. Assuming each parameter is stored with eight-bit precision, a 40-spin system requires one terabyte of memory to store a state. 270 spins already require more bits than the estimated number of 10^{80} protons in the universe [2].

In additional to the memory requirements, exact calculation of expectation values also poses a computational problem due to exponential scaling of the number of configurations.

This happens both when computing classical statistical observables

$$\langle O \rangle \propto \sum_{\mathbf{c}} O(\mathbf{c}) p(\mathbf{c}), \tag{1}$$

with the probability $p(\mathbf{c})$ for a given configuration, and quantum statistical observables

$$\left\langle \hat{O} \right\rangle \propto \mathrm{tr}\left(\hat{O} \exp(-\beta \hat{H})\right), \tag{2}$$

with the inverse temperature $\beta^{-1} = k_\mathrm{B} T$ and the Hamiltonian $\hat{H}$. Classical Monte-Carlo methods [3] can calculate expectation values in polynomial time [4].

Quantum Monte-Carlo systems are inefficient for fermionic systems. To apply a Monte-Carlo algorithm to the quantum problem one needs to map it to a classical problem first so that expectation values can be written in a similar fashion as equation (1) [5]. The procedure works well for most bosonic systems (except spin-glasses) and non-frustrated spin-models, because, like in a classical system, the weights $p(\mathbf{c})$ are strictly positive. For fermionic systems the weights $p(\mathbf{c})$ turn out to have varying signs [4], which causes the expectation value to fluctuate wildly depending on how the Hilbert space is sampled. This is called the *sign problem* and prohibits fast calculations of fermionic many-body systems using quantum Monte-Carlo methods. So far no other universal way has been found to do efficient calculation. For some special cases other powerful numerical methods have been applied successfully, like the density matrix renormalization group (DMRG) [6] for one dimensional systems and dynamical mean-field theory (DMFT) [7] in infinite dimensions.

Analog Quantum Simulation

In his seminal keynote speech Feynman [8] proposed to use a (well-understood and controlled) quantum system to simulate another quantum system. In this case one uses a quantum system that can be mapped onto the same Hamiltonian as the one of interest.

Ultracold quantum gases are an ideal platform to study condensed matter models. In particular, there is an analogy between solid-state systems and ultracold atoms in optical lattices. The optical lattice creates a periodic potential for the ultracold atoms, just like ionic

cores create a periodic potential for the electrons in a solid.

Various implementations of condensed matter systems have been demonstrated with ultracold atoms, ranging from the superfluid to Mott insulator transition [9], to the BCS–BEC crossover [10, 11], to classical [12] and quantum magnetism [13]. Additionally experiments have been conducted to study localization in disordered potentials [14, 15, 16]. Optical lattices are not limited to square lattices. Graphene-like [17], triangular, hexagonal [12], and Kagome lattices [18] have been used as well. Recent experiments have also managed to emulate magnetic fields in optical lattices [19, 20, 21] and in bulk [22, 23]. There are proposals to bring ultracold atoms into the quantum Hall regime [24, 25].

But quantum simulators can go beyond just mimicking condensed matter systems. With the creation of artificial gauge fields, for example, it is possible to create new exotic states of matter [26, 27, 28]. There are even some schemes to use ultracold atoms to study problems in high-energy physics [29, 30, 31].

Fermi Gas Microscopy

Ultracold neutral atoms provide a very scalable route to quantum simulation, but they have lacked the controllability of trapped ions or superconducting qubits [32]. Recent developments [33, 34, 35, 36], however, have enabled optical site-resolved imaging and control [37] of ultracold atoms in a single layer of a three dimensional lattice.

While most solid-state experiments and ultracold quantum gas experiments can only do bulk measurements, the ability to directly detect real space correlations in strongly correlated systems can be a big advantage [38, 39, 40, 41]. Furthermore single-site resolved detection makes the study of spatially-resolved dynamics possible.

The locally extremely low entropy in Mott insulating regions [35, 36] in an inhomogenious Bose-Einstein condensate in an optical lattice also has been a starting point for condensed matter quantum simulations [13] and could be used for quantum information processing in future [42]. The possibility to restrict oneself to certain regions within an optical lattice greatly enhances the sensitivity and has allowed to study excitations near a

quantum phase transition [43].

Until now all quantum gas microscopes have used bosonic $^{87}_{37}$Rb. The extension of this technique to a fermionic species will allow to address a whole other class of problems that rely on the fermionic nature of the particles, most prominently the Fermi-Hubbard model [44]. The phase diagram of the Fermi-Hubbard model is theoretically only well understood for the case of one fermion per lattice site, but its properties away from half-filling (in doped Mott insulators) are not fully known [45]. It is believed that the Fermi-Hubbard model is a minimal model that exhibits d-wave superfluidity, a possible explanation for high-temperature superconductivity [46, 47, 48, 49].

Several groups are working on detecting anti-ferromagnetic order at half-filling using bulk techniques [50, 51, 52]. This is a good example where a quantum gas microscope would excel. Since there is a smooth transition from a Mott insulator to a anti-ferromagnet at lower temperatures, with in-situ imaging we will be able to detect anti-ferromagnetic domains in low entropy regions before long-range order would show up in bulk measurements. In inhomogeneous systems the metallic shell surrounding the Mott-insulation anti-ferromagnet in the center also washes out the signature of ordering in bulk experiments, whereas a quantum gas microscope can look at the central region directly.

Why Lithium?

In our Fermi gas microscope we are using $^{6}_{3}$Li. It is the lightest fermionic alkali atom that has a optical transition accessible with conventional lasers. The two key parameters of the Fermi-Hubbard Hamiltonian (1.138), the on-site interaction U and the tunneling t, depend on the mass m via the recoil energy $E_\mathrm{r} \propto 1/m$ (see 1.5). For example, for a given tunnel coupling t in the Hubbard model, the absolute tunneling rate is more than six times faster than for the only other fermionic alkali atom $^{40}_{19}$K. Even in ultra-high vacuum, experiments with ultracold atoms are ultimately limited by background gas collisions. These collisions limit the maximum duration of an experiment to $\mathcal{O}(1\,\mathrm{s})$. The advantage of using a lighter species becomes even more apparent when looking at the superexchange rate

$\propto t^2/U \propto m$ (see 1.5.4.1), the rate of magnetic ordering in the tight binding regime (see 1.5.2). Typically this timescale is on the order of a few Hertz to tens of Hertz [40], close to the experimental limitations mentioned above. In our experiments superexchange rates of more than $\mathcal{O}(100\,\mathrm{Hz})$ are feasible while still being in the single band Hubbard regime.

Furthermore the on-site interaction U can be controlled by means of a magnetic Feshbach resonance (see 1.2). It enables us to tune the scattering length to any value from $-\infty$ to $+\infty$, including the non-interacting case. While bosons suffer from severe three-body losses near a Feshbach resonance, the Pauli exclusion principle allows Fermi mixtures to have long lifetimes.

In addition, it would be possible to switch to the bosonic isotope ${}^{7}_{3}\mathrm{Li}$ with only minor modifications to the laser system to study bosonic systems or combine both isotopes to study Bose-Fermi mixtures in an optical lattice.

The extension of quantum gas microscopy to a fermionic species to study Fermi-Hubbard physics seems straightforward. But with the higher recoil energies $E_\mathrm{r}^{(\lambda)} = \frac{h^2}{2m\lambda^2}$ (with wavelength λ) of the lighter alkali atoms, cooling during fluorescence imaging with the microscope becomes more involved. Each scattered photon imparts a bigger momentum than is the case for ${}^{87}_{37}\mathrm{Rb}$. For typical trap depths each atom can only scatter a handful of photons before it is heated out of the trap.

To circumvent this loss sub-Doppler cooling techniques have been applied to quantum gas microscopes. Polarization gradient cooling might still be an option for ${}^{40}_{19}\mathrm{K}$, but for ${}^{6}_{3}\mathrm{Li}$ the unresolved excited state hyperfine structure of the D_2-line, and therefore the lack of differential ac Stark shifts for the different magnetic sublevels, prevent effective polarization gradient cooling. Other sub-Doppler cooling techniques need to be employed to ${}^{6}_{3}\mathrm{Li}$.

This thesis describes our experimental apparatus and the Raman sideband cooling technique that we have successfully used to image quantum degenerate, fermionic lithium atoms in an optical lattice with single-site resolution.

Synopsis

This work consists of five chapters. In the first chapter I would like to establish a few general theoretical concepts required for the understanding of the interactions of atoms with electromagnetic fields, as well as the physics of optical lattices.

The Raman cooling that allows us to do fluorescence imaging in an optical lattice is explained in a dedicated second chapter.

The following description of the experimental details is split into three parts. First, the different light sources used in the experiment are introduced. Second, the optical setups required for the lasers to serve their functions are illustrated. And finally their functions are described in greater detail in the context of the whole experimental sequence, interspersed with short very specific theoretical sections.

A chapter about the experimental control hard- and software is aimed towards future students. The overview should help them to understand the basics and some of the particularities of our system, so that they can extend its functionality in the future.

Finally I am going to conclude with an outlook on possible future upgrades of the experiment and the problems that could be addressed.

Chapter 1

Theory

1.1 Atomic Physics

Although we are trying to study condensed matter physics, an understanding of the fundamental atomic physics of alkali atoms including the interaction with external fields is nevertheless required. Gehm [53] has written an excellent review for ^{6}Li, which I will refer to in many places. The basic level structure of the 2s states are depicted in figure 1.1.

1.1.1 Magnetic Fields And Microwave Transitions

One of the basic interactions of an atom with an electromagnetic field is the interaction of its permanent magnetic dipole moment $\boldsymbol{\mu}$ with an external magnetic field $\mathbf{B}$. It is described by the following Hamiltonian:

$$\hat{H}_B = -\frac{1}{\hbar}\hat{\boldsymbol{\mu}} \cdot \mathbf{B} = -\frac{\mu_\mathrm{B}}{\hbar} \sum_{\hat{\mathbf{X}} \in \{\hat{\mathbf{L}},\hat{\mathbf{S}},\hat{\mathbf{I}}\}} g_X \hat{\mathbf{X}} \cdot \mathbf{B}, \tag{1.1}$$

where $\hat{\boldsymbol{\mu}}$ denotes the magnetic moment operator consisting of a orbital $\hat{\mathbf{L}}$, electronic spin $\hat{\mathbf{S}}$ and nuclear spin $\hat{\mathbf{I}}$ part. The g-factors g_X can be found in the literature [53, 54].

For fields smaller than the hyperfine splitting the coupled $|F, m_F\rangle$ quantum numbers are the "good quantum numbers". For larger fields the electronic and nuclear spin decouple and $|I, m_I; J, m_J\rangle$ take over. The 2s states are typically labeled by $|1\rangle, |2\rangle, \ldots, |6\rangle$ in increasing

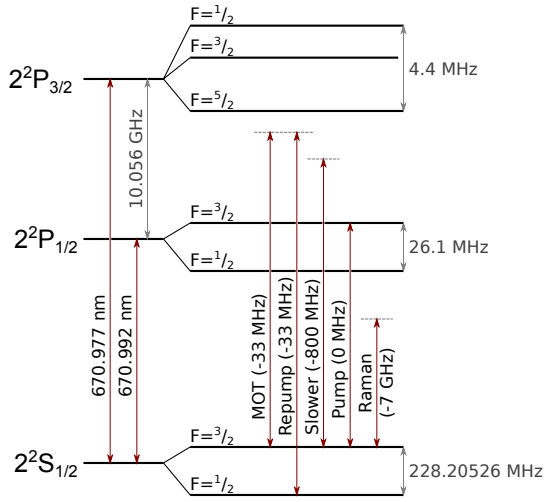

Figure 1.1: Level structure of the $n = 2$ states of $^6_3$Li and some of the laser detunings used in the experiment

energy (see figure 1.2). The Breit-Rabi diagram for the groundstate of ^{6}Li is shown in figure 1.3.

Transitions between the hyperfine states can be driven by applying an oscillation magnetic field perpendicular to the quantization axis. In our experiment this field is generated by a single loop microwave antenna. Since the wavelength at 228 MHz is 1.3 m and therefore a lot larger than the distance of the antenna to the atoms, the magnetic field profile is identical to that of a loop driven with constant current. A microwave field in this orientation can change the magnetic quantum number by ± 1. At low field the relative transitions matrix

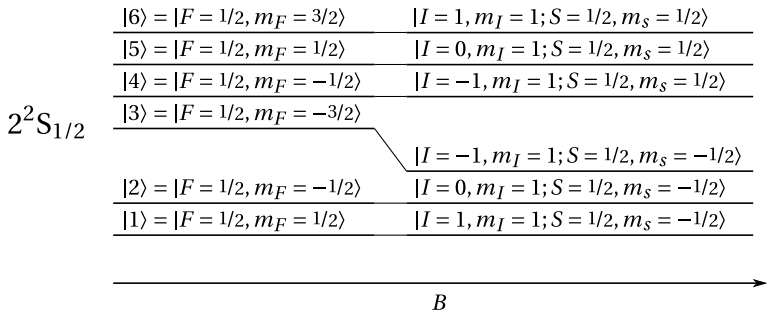

Figure 1.2: Quantum numbers of the 2s groundstate of $^6_3$Li in low and high magnetic field

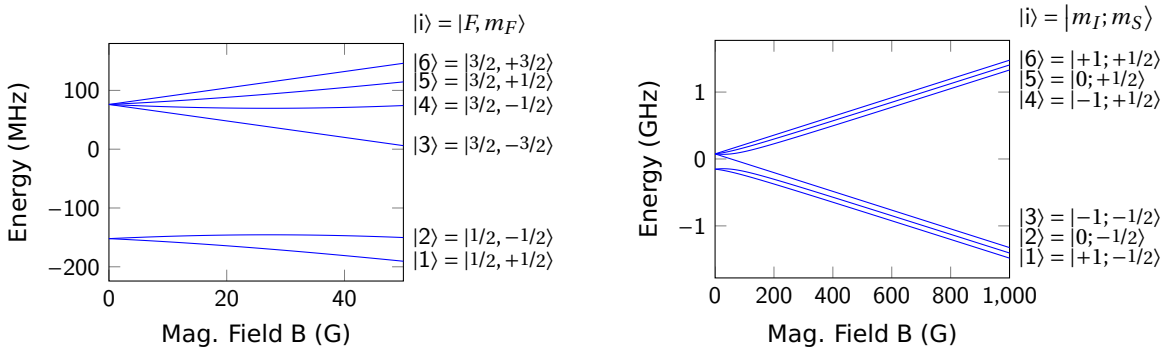

Figure 1.3: Breit-Rabi diagram for the 2s groundstate of ^{6}Li

elements $\langle j \,|\, \hat{\mu}_x \,|\, i \rangle$ in arbitrary units are

$$\begin{array}{c} \\ |1\rangle \\ |2\rangle \\ |3\rangle \\ |4\rangle \\ |5\rangle \\ |6\rangle \end{array} \begin{array}{c} \begin{array}{cccccc} |1\rangle & |2\rangle & |3\rangle & |4\rangle & |5\rangle & |6\rangle \end{array} \\ \begin{pmatrix} & \sqrt{1} & 0 & \sqrt{2} & 0 & -\sqrt{6} \\ \sqrt{1} & & -\sqrt{6} & 0 & \sqrt{2} & 0 \\ 0 & -\sqrt{6} & & \sqrt{3} & 0 & 0 \\ \sqrt{2} & 0 & \sqrt{3} & & \sqrt{4} & 0 \\ 0 & \sqrt{2} & 0 & \sqrt{4} & & \sqrt{3} \\ -\sqrt{6} & 0 & 0 & 0 & 3 & \end{pmatrix} \end{array}. \tag{1.2}$$

At high field one can either flip the electron spin (e.g. $|1\rangle \to |6\rangle$ or flip the nuclear spin (e.g. $|1\rangle \to |2\rangle$) . The coupling is $\epsilon = \sqrt{2}\,|g_I/g_S| \sim 1/3159$ weaker in the latter case. The transition matrix elements at high magnetic field in arbitrary units are approximately

$$\begin{array}{c} \\ |1\rangle \\ |2\rangle \\ |3\rangle \\ |4\rangle \\ |5\rangle \\ |6\rangle \end{array} \begin{array}{c} \begin{array}{cccccc} |1\rangle & |2\rangle & |3\rangle & |4\rangle & |5\rangle & |6\rangle \end{array} \\ \begin{pmatrix} & \epsilon & 0 & 0 & 0 & -1 \\ \epsilon & & -\epsilon & 0 & 1 & 0 \\ 0 & -\epsilon & & -1 & 0 & 0 \\ 0 & 0 & -1 & & \epsilon & 0 \\ 0 & 1 & 0 & \epsilon & & -\epsilon \\ -1 & 0 & 0 & 0 & -\epsilon & \end{pmatrix} \end{array}. \tag{1.3}$$

1.1.2 Light-Matter Interaction

An atom can also be coupled to an oscillating electric field. The Hamiltonian describing a single atom and a time-varying driving electromagnetic field can be separated into three terms

$$\hat{H} = \hat{H}_{\mathrm{A}} + \hat{H}_{\mathrm{L}} + \hat{V}_{\mathrm{AL}}, \tag{1.4}$$

where $\hat{H}_{\mathrm{A}}$ is the atomic Hamiltonian, $\hat{H}_{\mathrm{L}}$ describes the electromagnetic field (i.e. the laser), and the interaction $\hat{V}_{\mathrm{AL}}$ between the two. For this work it is sufficient to consider the driving field as a classical plane wave.

$$E(\mathbf{r}, t) = \frac{1}{2}\mathcal{E} \exp\left(-i\left(\omega_{\mathrm{L}} t - \mathbf{k}\cdot\mathbf{r}\right)\right) + \text{c.c.} \tag{1.5}$$

This is justified for coherent states [55]

$$|\alpha\rangle = \exp\left(-\frac{|\alpha|^2}{2}\right) \sum_{n=0}^{\infty} \frac{\alpha^n}{\sqrt{n!}} |n\rangle \tag{1.6}$$

with large photon numbers. Here $|n\rangle$ denotes photon number state in a single mode, also known as Fock state. Coherent states are an excellent approximation for laser fields used in our experiment. In addition, for large average photon numbers the term $\hat{H}_{\mathrm{L}}$ can be left out of equation (1.4) since the overall photon number stays approximately constant.

Atoms couple to the electric field dominantly via an (induced) electric dipole, so that the interaction reads [56]

$$\hat{V}_{\mathrm{AL}} = -\hat{\mathbf{d}} \cdot \mathbf{E}(\mathbf{r}, t) = e\hat{\mathbf{r}} \cdot \mathbf{E}(\mathbf{r}, t). \tag{1.7}$$

Contributions from higher electric or magnetic multipoles are suppressed and only play a role, when the direct transition is dipole forbidden, e.g. for microwave transitions or in alkali-earth atoms.

1.1.2.1 Two-Level Atom

If a groundstate $|1\rangle$ only couples to one excited state $|2\rangle$, the atom can be modeled as a two-level system. In the two-level approximation the atomic Hamiltonian reduces to

$$\hat{H}_{\mathrm{A}} = \hbar\omega_{\mathrm{A}} |2\rangle \langle 2| , \tag{1.8}$$

where the $\hbar\omega_{\mathrm{A}}$ is equal to the energy difference between the two states. This simplification is valid if all other excitation and decay channels can be neglected.

For now it will be assumed that the electric field does not vary over the length scale of an atom, so that we can approximate $\exp(i\mathbf{k}\cdot\hat{\mathbf{r}}) \approx 1$. This approximation is called the *dipole approximation*.

The situation can be simplified even more if all atomic physics details of the light-matter interaction (like the exact atomic wavefunction or polarization of the laser) are condensed into the matrix elements of the dipole operator $\mu_{i,j} = \langle i| \hat{d} |j\rangle$, which can be calculated or found in the literature [57]. The total Hamiltonian for the two-level system with the matrix elements $\mu = \mu_{1,2} = \mu_{2,1}^*$ reads [58]

$$\hat{H} = \hbar\omega_{\mathrm{A}} |2\rangle \langle 2| - \frac{1}{2} \left(\mu |1\rangle \langle 2| + \mu^* |2\rangle \langle 1|\right) \left(\mathcal{E} \exp\left(-i\omega_{\mathrm{L}} t\right) + \mathcal{E}^* \exp\left(+i\omega_{\mathrm{L}} t\right)\right). \tag{1.9}$$

To solve the time dependent Schrödinger equation

$$i\hbar \frac{\mathrm{d}}{\mathrm{d}t} |\psi\rangle = \hat{H} |\psi\rangle , \tag{1.10}$$

we rewrite the equations in the basis of the bare atomic states

$$|\psi(t)\rangle = c_1(t) |1\rangle + c_2(t) |2\rangle .$$

Additionally, by going into the *rotating frame* [59] of the driving field the equations of motion of the transformed amplitudes read

$$\begin{aligned} i\dot{c}_1(t) &= -\left(\mathcal{E} \exp(-2i\omega_{\mathrm{L}} t) + \mathcal{E}^*\right) \frac{\mu}{2\hbar} c_2(t) \\ i\dot{c}_2(t) &= -\delta c_2(t) - \left(\mathcal{E} + \mathcal{E}^* \exp(2i\omega_{\mathrm{L}} t)\right) \frac{\mu^*}{2\hbar} c_1(t). \end{aligned} \tag{1.11}$$

In the near-resonant case we can neglect the terms oscillating at $2\omega_{\mathrm{L}}$, since the important dynamics happen on a much slower timescale. This approximation is called the *rotating wave approximation*, which is valid as long as $\delta \ll \omega_{\mathrm{L}}, \omega_{\mathrm{A}}$. Equations (1.11) can be rewritten as an effective Hamiltonian

$$\hat{H}_{\mathrm{eff}} = -\hbar\delta \left|2\right\rangle \left\langle 2\right| - \frac{\hbar}{2}\left(\Omega \left|1\right\rangle \left\langle 2\right| + \Omega^{*} \left|2\right\rangle \left\langle 1\right|\right) \tag{1.12}$$

with the *Rabi frequency*

$$\Omega = \frac{\mu\mathcal{E}}{\hbar}. \tag{1.13}$$

In this form the dynamics do not depend on the microscopic details of the interaction, only on the Rabi frequency.

The general solutions in the rotating frame for the initial conditions $c_1(0) = 1$, $c_2(0) = 0$ and in the rotating wave approximation are given by

$$\begin{aligned} c_1(t) &= \exp\left(i\frac{\delta}{2}t\right)\left(\cos\left(\frac{1}{2}\Omega' t\right) - i\frac{\delta}{\Omega'}\sin\left(\frac{1}{2}\Omega' t\right)\right) \\ c_2(t) &= i\exp\left(i\frac{\delta}{2}t\right)\frac{\Omega}{\Omega'}\sin\left(\frac{1}{2}\Omega' t\right), \end{aligned} \tag{1.14}$$

where the *generalized Rabi frequency* is given by

$$\Omega' = \sqrt{\delta^2 + \left|\Omega\right|^2}. \tag{1.15}$$

Experimentally more relevant is the time-evolution of the populations in the bare states $\rho_{jj} = \left|\left\langle j \,|\, j\right\rangle\right|^2$

$$\begin{aligned} \rho_{22}(t) &= \left(\frac{\Omega}{\Omega'}\right)^2 \sin^2\left(\frac{1}{2}\Omega' t\right) \\ \rho_{11}(t) &= 1 - \rho_{22}(t). \end{aligned} \tag{1.16}$$

These solutions describe oscillations is the atomic population at the generalized Rabi frequency, the *Rabi oscillations*.

Instead of continuously driving the system it is also possible to introduce transitions via a single pulse. A short on-resonant ($\delta = 0$) pulse $\Omega(t)$ with the area $\int_{-\infty}^{\infty}\Omega(t)\,\mathrm{d}t = \pi$ (called

a π-pulse) exchanges the population in the two bare states. This can be used to transfer population to an excited state. A $\pi/2$-pulse creates a coherent superposition of the two states.

1.1.2.2 Dressed States

For numerical calculations it is often easier to write the Hamiltonian (1.12) in matrix form in the bare basis $|1\rangle = (1,0), |2\rangle = (0,1)$

$$\mathbf{H} = -\hbar \begin{pmatrix} \delta & \frac{\Omega}{2} \\ \frac{\Omega^*}{2} & 0 \end{pmatrix}. \tag{1.17}$$

The eigenstates of the coupled two-level systems, the *dressed states*, are given by

$$\begin{aligned} |-\rangle &= \mathcal{N}_- \left(|1\rangle - \frac{\Omega^*}{\delta + \Omega'} |2\rangle \right) \\ |+\rangle &= \mathcal{N}_+ \left(\frac{\delta - \Omega'}{\Omega^*} |1\rangle + |2\rangle \right) \end{aligned} \tag{1.18}$$

with the energies

$$E_\pm = -\frac{\hbar}{2} \left(\delta \pm \Omega' \right) \tag{1.19}$$

and normalization constants $\mathcal{N}_\pm$. The detuning dependence of their energies is depicted in figure 1.4.

1.1.2.3 Dipole Force

In the far-detuned limit $\delta \gg \Omega$ (while still in the regime where the rotating wave approximation is valid) the dressed states

$$|-\rangle \approx |1\rangle + \frac{1}{2}\frac{\Omega}{\delta} |2\rangle, |+\rangle \approx -\frac{1}{2}\frac{\Omega}{\delta} |1\rangle + |2\rangle$$

and the generalized Rabi frequency

$$\Omega' = \delta + \frac{1}{2}\frac{|\Omega|^2}{\delta^2} + \mathcal{O}(\frac{|\Omega|^4}{\delta^4})$$

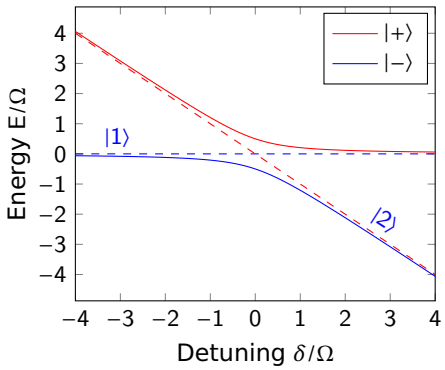

Figure 1.4: Dressed state energies for varying detuning

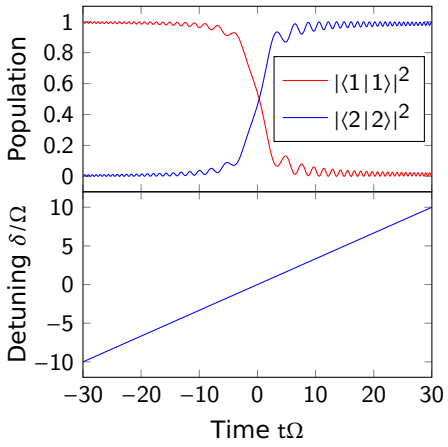

Figure 1.5: Populations during a rapid adiabatic passage

can be expanded to second order in Ω/δ. It becomes evident that for large detunings most of the atomic population stays in the ground (excited) state with only a small $\propto (\Omega/\delta)^2$ admixture of the excited (ground) state. The energies of these states

$$E_- = \frac{|\Omega|^2}{4\delta}, E_+ = -\delta - \frac{|\Omega|^2}{4\delta}$$

are shifted up (down) by the *ac Stark shift*

$$\Delta E_{\mathrm{ac}} = \frac{|\Omega|^2}{4\delta}. \tag{1.20}$$

In the two-level system the ground and excited state always get shifted the opposite direction, whereas for "real" multilevel atoms the ac Stark shift has to be calculated taking all states including the continuum into account (for example see [60]).

For a spatially varying electric field/Rabi frequency $\Omega(\mathbf{r})$ this can be used to apply a force to atoms, the so-called *dipole force*. For a *red-detuned* ($\delta < 0$) laser the potential is attractive and atoms get pulled towards the intensity maximum, whereas for a *blue-detuned* ($\delta > 0$) lasers atoms get repelled.

Since there is only a small admixture of the excited state in the $|-\rangle$ state, for sufficient detuning coherent and incoherent scattering can be neglected (see also section 2.3), yielding a conservative potential to good approximation. If one is not limited by laser power $P_{\mathrm{L}} \propto |\Omega|^2$,

the excited state population can be reduced by detuning further, because $\Delta E_{\mathrm{ac}} \propto \delta^{-1}$ decays more slowly than the $\propto \delta^{-2}$ dependence of the population admixture. The full expression for the dipole force without the rotating wave approximation is given in 1.79.

1.1.2.4 Rapid Adiabatic Passage

The coupling $|1\rangle$ and $|2\rangle$ via the dressed states (1.18) can be used to move population from on state into another. This technique is more robust against uncertainties in detuning, Rabi frequency, and timing than a π-pulse (see 1.1.2.1). If the detuning is ramped slowly compared to the splitting Ω of the avoided crossing, the atom adiabtically follows the $|-\rangle$ state from $|-(\delta = -\infty)\rangle = |1\rangle$ to $|-(\delta = +\infty)\rangle = |2\rangle$ (see figure 1.5). This procedure is called a *rapid adiabatic passage* and is used in several places in our experiment, for example to reliably transfer population into excited hyperfine states of the groundstate manifold.

The condition for a linear sweep $\delta(t) = \alpha t$ to be adiabatic is given by the Landau-Zener criterion [61, 62]

$$\frac{|\Omega|^2}{\frac{\mathrm{d}}{\mathrm{d}t}\delta(t)} \ll 1. \tag{1.21}$$

This also gives this technique its alternative name, a *Landau-Zener sweep*.

1.1.2.5 Spontaneous Emission

The formalism described in 1.1.2.1 is sufficient to describe coherent dynamics, but is inconvenient for including *spontaneous emission*. Better suited are *density matrices* [63], a concept from quantum statistical mechanics, that allows to "trace out" unwanted states of the system, for example the modes into which a photon is spontaneously emitted. Formally density matrices are defined as

$$\hat{\rho} = \sum_i p_i \left|\psi_i\right\rangle \left\langle\psi_i\right|, \tag{1.22}$$

where $|\psi_i\rangle$ is a "pure" state and p_i the probability to find the system in this state.

The density matrix of a two-level atom is given by

$$\rho = \begin{pmatrix} |c_1|^2 & c_1 c_2^* \\ c_1^* c_2 & |c_2|^2 \end{pmatrix} \tag{1.23}$$

and its equation of motion by [59]

$$\begin{aligned} \dot{\rho}_{11} &= \gamma\rho_{11} - \frac{i}{2}\left(\Omega\rho_{12} - \Omega^*\rho_{21}\right) \\ \dot{\rho}_{22} &= -\gamma\rho_{22} + \frac{i}{2}\left(\Omega\rho_{12} - \Omega^*\rho_{21}\right) \\ \dot{\rho}_{12} &= -\left(\frac{\gamma}{2} + i\delta\right)\rho_{12} + i\frac{\Omega^*}{2}\left(\rho_{22} - \rho_{11}\right) \\ \dot{\rho}_{21} &= -\left(\frac{\gamma}{2} - i\delta\right)\rho_{21} + i\frac{\Omega^*}{2}\left(\rho_{22} - \rho_{11}\right). \end{aligned} \tag{1.24}$$

These equations are also known as the *optical Bloch equations* and include decay and dephasing caused by finite excited state lifetime giving rise to the natural linewidth γ.

In steady state ($\dot{\rho} \to 0$) the excited state population is given by

$$\rho_{22} = \frac{s_0/2}{1 + s_0 + (2\delta/\gamma)^2}, \tag{1.25}$$

with the *on-resonant saturation parameter*

$$s_0 = 2\frac{|\Omega|^2}{\gamma^2}. \tag{1.26}$$

For the every day lab use it is often more convenient to write the on-resonant saturation parameter [57]

$$s_0 \equiv \frac{I}{I_{\text{sat}}}$$

as the ratio of the light intensity I to the saturation intensity given by

$$I_{\text{sat}} = \frac{2\pi^2}{3}\frac{hc\gamma}{\lambda^3}. \tag{1.27}$$

The excited state population (1.25) can also be written in a dimensionless form

$$\rho_{22} = \frac{1}{2}\frac{s}{1+s}, \tag{1.28}$$

with the *generalized saturation parameter*

$$s \equiv \frac{s_0}{1 + (2\delta/\gamma)^2} \tag{1.29}$$

As a function of the detuning δ equation (1.25) follows a Lorentzian profile with a FWHM of $\gamma' = \gamma\sqrt{1 + s_0}$. When driven with a large Rabi frequency Ω the width increases from the natural linewidth γ. This effect is known as *power broadening*. Another important feature of equation (1.25) is that the excited state population saturates at $\rho_{22} \to \frac{1}{2}$ for $\delta = 0$ and $\Omega \to \infty$. In other words it is not possible to create a steady state population inversion in a two level system.

In the weak driving limit the amount of population is the excited state is proportional to the saturation parameter s

$$\rho_{22} = \frac{1}{2}s + \mathcal{O}(s^2) = \frac{\Omega^2}{\gamma^2 + (2\delta)^2} + \mathcal{O}(\Omega^4). \tag{1.30}$$

Hence, the exited state population can be kept small by either detuning or by reducing the incident laser power. In both cases the total rate at which a driven atom is scattering photons (coherently and incoherently) is given by

$$\gamma_S = \gamma\rho_{22}. \tag{1.31}$$

Each time an atom absorbs a photon it gets a directed momentum kick $\hbar\mathbf{k}_L$, the spontaneous emission on the other hand is uniform over the whole 4π solid angle. So on average the momentum of an atom is increasing by $\hbar\mathbf{k}_L\gamma\rho_{22}t$ with gives rise to the *radiation force*

$$\mathbf{F}_{\text{rad}} = \hbar\mathbf{k}_L\gamma\rho_{22}. \tag{1.32}$$

Together with the dipole force (1.20), the radiation force set the foundation for all laser cooling and trapping experiments.

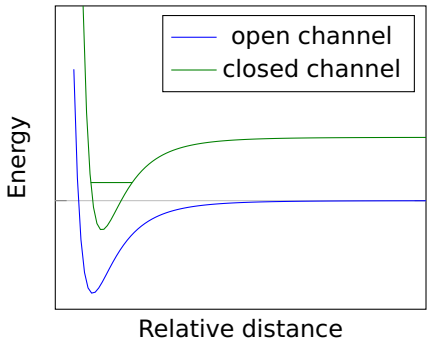

Figure 1.6: Simplified two-channel model for a Feshbach resonance (from [1])

1.2 Feshbach Resonances

Feshbach resonances offer an unique way to tune and control the interactions between particles. Köhler et al. [64] and Chin et al. [1] have written an excellent review paper on the physics of Feshbach resonances.

If the energy of the two colliding atoms is near a molecular bound state (see figure 1.6), the scattering between the two is resonantly enhanced. For atoms with non-zero nuclear spin the magnet moment of the dimer differs from the one of a bare atom. The relative position of the molecular bound state with respect to the atomic energies can therefore be tuned with an external static magnetic field.

Near the s-wave scattering resonance (ignoring inelastic decay channels) the scattering length can be parametrized by [65]

$$a(B) = a_{\mathrm{bg}} \left(1 - \frac{\Delta}{B - B_0}\right), \tag{1.33}$$

with the background scattering length a_{bg}, the magnetic field where the resonance appears B_0, and the width of the resonance Δ. For homo-nuclear Feshbach molecules the binding energy of the dimers near the resonance ($a > 0$) can be approximated by

$$E_{\mathrm{b}} = \frac{\hbar^2}{2m} a^2. \tag{1.34}$$

The molecules are typically in their highest rovibrational state, which has an extent of $\sim a$ and a dimer-dimer scattering length of $a_{\mathrm{dd}} = 0.6a$ [66].

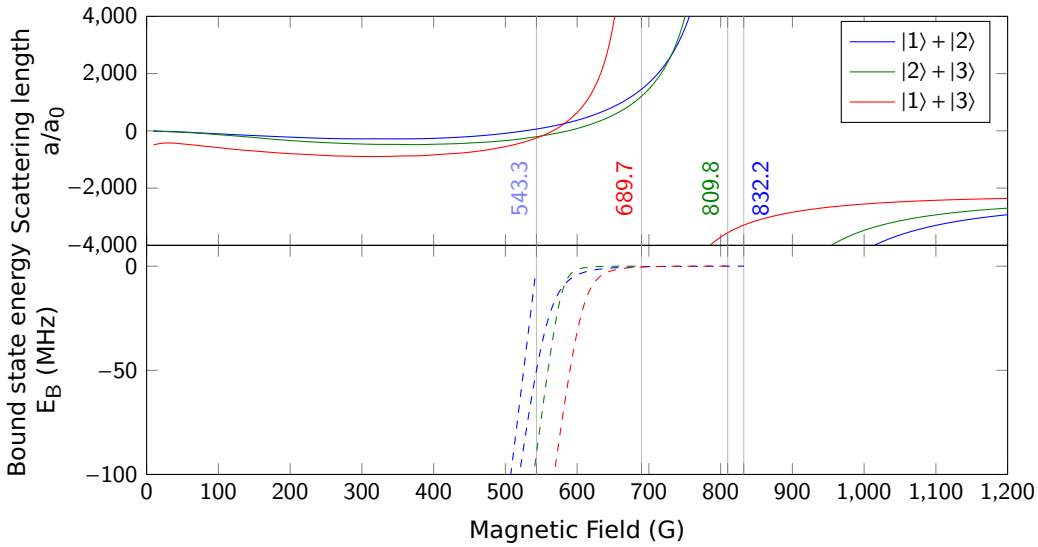

Figure 1.7: Scattering length and molecular binding energy for $^6_3$Li

In fermionic $^6_3$Li several resonances between different hyperfine states have been observed (see figure 1.7, data from [67]). The broad resonance between the $|1\rangle$ and $|2\rangle$ states at $B_0 = 832.18(8)\,\mathrm{G}$ with a width of $\Delta = 262.3(3)\,\mathrm{G}$ [67] (see 1.1.1 for labeling of the states) is most commonly used. Near this resonance there are further resonances between the $|2\rangle$ and $|3\rangle$ ($B_0 = 809.76(5)\,\mathrm{G}$ [67]) states and $|1\rangle$ and $|3\rangle$ states ($B_0 = 689.68(8)\,\mathrm{G}$ [67]). This makes $^6_3$Li a perfect candidate to study three-state systems with tunable interactions [68].

A narrow ($\Delta = 0.1\,\mathrm{G}$ [1]) resonance at $B_0 = 543.26(10)\,\mathrm{G}$ [69] between $|1\rangle$ and $|2\rangle$ is less frequently used directly, but it provides a zero-crossing of the scattering length at $B_{a=0} = 527.5(2)\,\mathrm{G}$ [70, 71]. This zero-crossing allows us to turn off interactions between the $|1\rangle$ and $|2\rangle$ states to study non-interacting Fermi gases.

On the repulsive side ($a > 0$) of the 830 G resonance molecule formation can occur via inelastic three-body collisions. For bosonic atoms this causes large losses which limit the usefulness of the Feshbach resonance [72], but for fermions the relaxation to more deeply bound molecules is suppressed by the Pauli exclusion principle [66]. We have used this fact to create a molecular condensate of Li_2 dimers (see 3.36).

1.2.1 Feshbach Resonances In Reduced Dimensions

With ultracold atoms in optical traps it is possible to study lower dimensional physics. For example, in an ellipsoidal optical dipole trap or in "tubes" created by a two-dimensional optical lattice created by two orthogonal lattices the system behaves effectively as a one-dimensional system. Because the trap frequencies in the transverse/radial directions are significantly higher than in the longitudinal/axial direction, the scattering into final states with excitations along the radial are suppressed.

The coupling constant g_{1d} replaces the three-dimensional scattering length in an effective Hamiltonian in one-dimension. It exhibits a singularity similar to the conventional Feshbach resonance. This *confinement induced resonance* [73] appears at a slightly shifted magnetic field [74, 75].

Two dimensional systems exhibit a similar behavior [76].

In three dimensional optical lattices, strong interactions between two atoms on a single lattice site alter the energy levels. If the scattering length a becomes comparable to the extent of the wavefunction (i.e. the harmonic oscillator length a_{QHO} (1.36) in deep lattices) the energy levels in the trap shift [77] due to coupling between different bands. This has been demonstrated experimentally by Stöfele et al. [78]. Strong interactions need be taken into account, when the system should be approximated by a Hubbard model (see 1.5.4). These effects can be incorporated into a generalized Hubbard model for both atoms and molecules [79, 80].

1.3 Quantum Harmonic Oscillator

The basic problem of a quantum harmonic oscillator is omni-present in physics (e.g. [81]). Since most optical traps can be approximated as a harmonic trap near their minimum, harmonic oscillators are of great importance for the understanding the physics of trapped ultracold atoms. Especially for the Raman cooling technique (see 2) the quantized motional states of trapped atoms are an essential ingredient.

1.3.1 One-Dimensional Harmonic Oscillator

The Hamiltonian for a single particle of mass m in a harmonic oscillator potential with a trap frequency ω is given by

$$\hat{H} = \frac{\hat{p}^2}{2m} + \frac{1}{2}m\omega^2\hat{x}^2. \tag{1.35}$$

It is possible to make it dimensionless by rewriting the position in multiples of the harmonic oscillator length

$$a_{\mathrm{QHO}} = \sqrt{\frac{\hbar}{m\omega}} \tag{1.36}$$

and rescaling the energy by $\hbar\omega$. The eigenfunction of the quantum harmonic oscillator in position space are

$$\psi_\nu(x) = \sqrt{\frac{1}{2^n\nu!}}\left(\frac{m\omega}{\hbar\pi}\right)^{1/4}\exp\left(-\frac{1}{2\hbar}m\omega x^2\right)\mathrm{H}_\nu\left(\sqrt{\frac{m\omega}{\hbar}}x\right), \tag{1.37}$$

where $\nu = 0, 1, \ldots, \infty$ labels the vibrational levels and $\mathrm{H}_\nu(x)$ are Hermite polynomials [82].

The energy levels in a harmonic oscillator

$$E_n = \hbar\omega\left(\nu + \frac{1}{2}\right) \tag{1.38}$$

are equally spaced by $\hbar\omega$.

Alternatively (1.35) can be solved by introducing the latter operators $\hat{a}$ and $\hat{a}^\dagger$, so that

$$\hat{x} = \frac{a_{\mathrm{QHO}}}{\sqrt{2}}\left(\hat{a}^\dagger + \hat{a}\right) \qquad\qquad \hat{p} = \frac{i\hbar}{\sqrt{2}a_{\mathrm{QHO}}}\left(\hat{a}^\dagger - \hat{a}\right). \tag{1.39}$$

With those operators the Hamiltonian reads

$$\hat{H} = \hbar\omega\left(\hat{n} + \frac{1}{2}\right), \tag{1.40}$$

where the number operator is given by $\hat{n} = \hat{a}^\dagger\hat{a}$. It counts the number of excitations in the oscillator, whereas $\hat{a}^\dagger$ ($\hat{a}$) creates (annihilates) an excitation. The normalized eigenstates (also known as *Fock states*) are given by

$$|\nu\rangle = \frac{\left(\hat{a}^\dagger\right)^n}{\sqrt{n!}}|0\rangle, \tag{1.41}$$

with the vacuum state $|0\rangle$.

1.3.2 Ensembles In A Harmonic Oscillator

If we add multiple indistinguishable particles, the physics depends on the quantum statistics of the particles. Ensembles of non-interaction bosons (integer total spin) or fermions (half-integer total spin) are described by the *Bose distribution* and the *Fermi-Dirac distribution* respectively. The fraction of the population found occupying an energy level E_i is given by [63]

$$n_{\substack{\mathrm{B}\\\mathrm{F}}}(E_i) = \frac{1}{\exp\left(\left(E_i - \mu\right) / \left(k_\mathrm{B} T\right)\right) \mp 1}. \tag{1.42}$$

The chemical potential μ is implicitly given by the normalization condition $\sum_i n(E_i) = N$ with the total atom number N.

In the limit of large numbers and when the "discrete-ness" of the trap levels does not play a role $k_\mathrm{B} T \gg \hbar\omega_i$, one can apply the *Thomas-Fermi approximation* and introduce the number density in phase-space [83]

$$f_{\substack{\mathrm{B}\\\mathrm{F}}}(\mathbf{r}, \mathbf{p}) = \frac{1}{\exp\left(\left(\frac{\mathbf{p}^2}{2m} + V(\mathbf{r}) - \mu\right) / \left(k_\mathrm{B} T\right)\right) \mp 1}. \tag{1.43}$$

Again, the chemical potential is given by the normalization condition

$$N_{\substack{\mathrm{B}\\\mathrm{F}}} = \frac{1}{(2\pi\hbar)^3} \int \mathrm{d}^3\mathbf{r}\, \mathrm{d}^3\mathbf{p}\, f_{\substack{\mathrm{B}\\\mathrm{F}}}(\mathbf{r}, \mathbf{p}). \tag{1.44}$$

The real (or momentum) space density distribution follows by integrating over the unwanted phase-space dimension [84]

$$n_{\substack{\mathrm{B}\\\mathrm{F}}}(\mathbf{r}) = \frac{1}{(2\pi\hbar)^3} \int \mathrm{d}^3\mathbf{p}\, f_{\substack{\mathrm{B}\\\mathrm{F}}}(\mathbf{r}, \mathbf{p}) = \pm \frac{1}{\lambda^3} \mathrm{Li}_{3/2}\left(\pm \exp\left(\frac{\mu - V(\mathbf{r})}{k_\mathrm{B} T}\right)\right), \tag{1.45}$$

with the thermal wavelength given by $\lambda = \sqrt{2\pi\hbar^2 / (m k_\mathrm{B} T)}$.

For a three-dimensional anisotropic harmonic oscillator $V(\mathbf{r}) = \sum_{i=1}^{3} \frac{1}{2} m\omega_i^2 r_i^2$ (with the geometric mean $\bar{\omega}^3 = \prod_{i=1}^{3} \omega_i$) the integral in (1.44) can be evaluated as well, yielding

$$N_{\substack{\mathrm{B}\\\mathrm{F}}}^{(\mathrm{QHO})} = \pm \left(\frac{k_\mathrm{B} T}{\hbar\bar{\omega}}\right)^3 \mathrm{Li}_3\left(\pm \exp\left(\frac{\mu}{k_\mathrm{B} T}\right)\right), \tag{1.46}$$

where $\mathrm{Li}_\nu(z)$ denotes the polylogarithm [82].

1.3.2.1 Thermal Cloud

In the high-T limit we reproduce the classical result (i.e. ignoring ∓ 1 in (1.43) or assuming the *Maxwell-Boltzmann distribution*). In this case (1.46) simplifies to

$$N_{\mathrm{th}} = \left(\frac{k_{\mathrm{B}}T}{\hbar\bar{\omega}}\right)^3 \exp\left(\frac{\mu}{k_{\mathrm{B}}T}\right), \tag{1.47}$$

giving rise to

$$\mu_{\mathrm{th}} = k_{\mathrm{B}}T \log\left(\frac{1}{N}\left(\frac{\hbar\bar{\omega}}{k_{\mathrm{B}}T}\right)^3\right) \tag{1.48}$$

and

$$n_{\mathrm{th}}(\mathbf{r}) = \frac{N}{\pi^{3/2}\bar{\sigma}^3} \exp\left(-\sum_{i=1}^{3}\left(\frac{r_i}{\sigma_i}\right)^2\right), \tag{1.49}$$

where $\bar{\sigma}^3 = \prod_{i=1}^{3}\sigma_i$ denotes the geometric mean of the rms cloud sizes

$$\sigma_i = \sqrt{2k_{\mathrm{B}}T/(m\omega_i^2)}. \tag{1.50}$$

Therefore the FWHM cloud size is

$$d_{\mathrm{th}}^{(i)} = 2\sigma_i\sqrt{\log 2} \approx 2.35\sqrt{\frac{k_{\mathrm{B}}T}{m\omega_i^2}}. \tag{1.51}$$

At first it seems surprising that the cloud size does not depend on the atom number, but an ensemble off non-interacting particles without spin statistics behaves identically to a single particle.

In a harmonic trap the phase space density for a thermal gas, an important quantity for optimizing evaporative cooling, is given by

$$\rho = N\left(\frac{\hbar\bar{\omega}}{k_{\mathrm{B}}T}\right)^3. \tag{1.52}$$

1.3.2.2 Degenerate Fermi Gas

For a fully degenerate gas at $T = 0$ the normalization defines the *Fermi energy*

$$E_{\mathrm{F}} = \mu(T = 0) = \hbar\bar{\omega}\sqrt[3]{6N}, \tag{1.53}$$

the highest occupied energy in the system. The in-trap real-space density near the trap center ($r_i \ll R_i$) is then given by

$$n_{\mathrm{F}}^{(T=0)}(\mathbf{r}) \approx \frac{8N}{\pi^2\bar{R}^3}\left(1 - \sum_{i=1}^{3}\frac{r_i^2}{R_i^2}\right)^{3/2}, \tag{1.54}$$

with the *Fermi radii* $R_i = \sqrt{2E_{\mathrm{F}}/(m\omega_i)^2}$ and their geometric mean $\bar{R}$. This can also be derived using the *local density approximation* with a spatially dependent chemical potential/Fermi energy $E_{\mathrm{F}}^{(\mathrm{free})}(\mathbf{r}) = E_{\mathrm{F}} - V(\mathbf{r})$ with the Fermi energy for a untrapped Fermi gas $E_{\mathrm{F}}^{(\mathrm{free})} = \frac{\hbar^2}{2m}\left(3\pi^2 n\right)^{3/2}$ [63], where the density is assumed to be locally constant $n \approx n(\mathbf{r})$.

The FWHM of the exact solution of (1.45) is given by

$$d_{\mathrm{F}}^{(i)}(T = 0) = 1.22R_i \approx 1.72\sqrt{\frac{E_{\mathrm{F}}}{m\omega_i^2}}. \tag{1.55}$$

Using definition (1.53) and the *Fermi temperature* $T_{\mathrm{F}} = E_{\mathrm{F}}/k_{\mathrm{B}}$ equation (1.46) can be rewritten in a universal form to simplify numerical calculations

$$\left(\frac{T}{T_{\mathrm{F}}}\right)^3 \mathrm{Li}_3\left(-\exp\left(\frac{\mu}{E_{\mathrm{F}}}\frac{T_{\mathrm{F}}}{T}\right)\right) = -\frac{1}{6}. \tag{1.56}$$

The atom number dependency now is absorbed into the Fermi energy.

Equation (1.48), which is a good approximation in the high temperature limit ($T \gtrsim 0.5T_{\mathrm{F}}$), can be rewritten in a similar fashion

$$\frac{\mu(T \gtrsim 0.5T_{\mathrm{F}})}{E_{\mathrm{F}}} \approx \frac{T}{T_{\mathrm{F}}}\log\left(\frac{1}{6}\left(\frac{T_{\mathrm{F}}}{T}\right)^3\right). \tag{1.57}$$

The low (but finite) temperature expansion this gives a Sommerfeld-like expression [83] for the chemical potential inside a harmonic trap

$$\frac{\mu_{\mathrm{F}}(T \ll T_{\mathrm{F}})}{E_{\mathrm{F}}} \approx \left(1 - \frac{\pi^2}{3}\left(\frac{T}{T_{\mathrm{F}}}\right)^2\right). \tag{1.58}$$

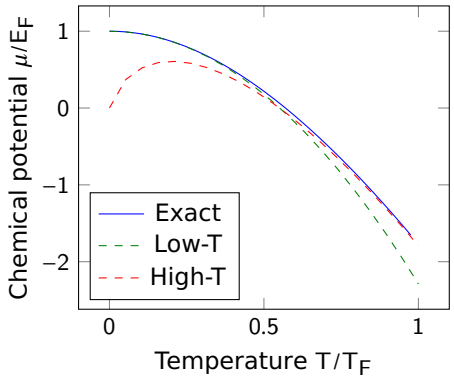

Figure 1.8: Chemical potential for a Fermi gas in a harmonic trap

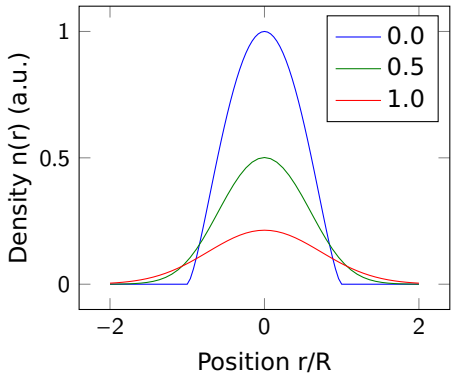

Figure 1.9: Density profiles for different T/T_F

The exact solution and the approximations are all plotted in figure 1.8 in agreement with Butts et al. [83].

1.3.2.3 Bose-Einstein Condensate

While fermions all occupy different states, at $T = 0$ all atoms in a non-interacting Bose-Einstein condensate occupy the ground of the trap. For a harmonic trap the wavefunctions are given by equation (1.37). Therefore the density distribution in the ground state $\nu = 0$ is

$$n_B^{(T=0)}(\mathbf{r}) = N\left(\frac{m\bar{\omega}}{\hbar\pi}\right)^{3/2} \exp\left(-\sum\left(\frac{r_i}{\sigma_B^{(i)}}\right)^2\right) \tag{1.59}$$

with an rms cloud size equal to the harmonic oscillator length

$$\sigma_B^{(i)} = \sqrt{\frac{\hbar}{m\omega_i}} \tag{1.60}$$

and FWHM of

$$d_B^{(i)}(T=0) = 2\sigma_B^{(i)}\sqrt{\log 2} \approx 1.67\sqrt{\frac{\hbar}{m\omega_i}}. \tag{1.61}$$

The cloud size of a Bose-Einstein condensate has a weaker dependence on the trap frequency ($\propto \omega_i^{-1/2}$) than for the degenerate Fermi gas or a thermal cloud ($\propto \omega_i^{-1}$) . A more detailed description of trapped (and also interacting) Bose-Einstein condensates can

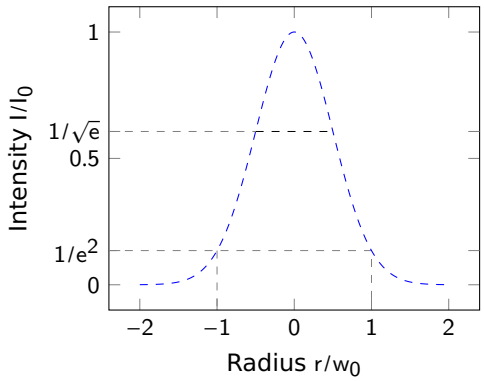

Figure 1.10: Radial intensity profile of a Gaussian beam at the focus

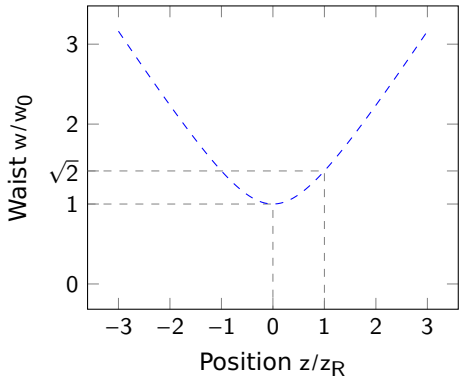

Figure 1.11: Gaussian beam waist along the optical axis

be found in Ketterle et al. [85].

1.4 Optical Potentials

1.4.1 Gaussian Beams

Laser beams can be well described as Gaussian beams. Gaussian beams are the solutions to the paraxial scalar Helmholtz equation and their electric field for a beam propagation along the z-axis and focused at is given by [86]

$$\tilde{E}(\rho, z) = E_0 \frac{w_0}{w(z)} \exp\left(-\left(\frac{\rho}{w(z)}\right)^2 - ik\left(z - \frac{\rho}{2R(z)}\right) + i\zeta(z)\right), \tag{1.62}$$

with a *Gaussian beam waist*

$$w(z) = w_0 \sqrt{1 + \left(\frac{z}{z_\mathrm{R}}\right)^2}. \tag{1.63}$$

The electric field here is written as a complex field, but the physical field is only its the real part $E(\rho, z) = \mathrm{Re}\left(\tilde{E}(\rho, z)\right)$.

The Gaussian beam waist is the *radius,* where the electric field amplitude has dropped to $1/e$ and the intensity to $1/e^2$ (see figure 1.10). The distance z_R where the waist has increased

by a factor of $\sqrt{2}$ of its minimum w_0 is called the *Rayleigh length*

$$z_{\mathrm{R}} = \frac{\pi w_0^2}{\lambda}. \tag{1.64}$$

The radius of curvature of the wave front is

$$R(z) = z\left(1 + \left(\frac{z_{\mathrm{R}}}{z}\right)^2\right). \tag{1.65}$$

Another related quantity is the *Gouy phase*

$$\zeta(z) = \arctan\frac{z}{z_{\mathrm{R}}}, \tag{1.66}$$

which describes the fact that the field undergoes a π phase shift when going through a focus. This plays a significant role in the design of resonators, but is irrelevant for the intensity profiles of propagating Gaussian beams.

In the far field ($z \gg z_{\mathrm{R}}$) the beam is well described by geometric optics: the beam radius increases linearly and gives rise to a divergence angle (half-angle)

$$\theta = \frac{w_0}{z_{\mathrm{R}}}. \tag{1.67}$$

The radius of curvature approaches $R(z \gg z_{\mathrm{R}}) = z$ as one would expect geometrically.

The intensity profile of a Gaussian beam is given by

$$I(\rho, z) = I_0\left(\frac{w_0}{w(z)}\right)^2 \exp\left(-2\left(\frac{\rho}{w(z)}\right)^2\right). \tag{1.68}$$

For a known total power P the peak intensity can be expressed as

$$I_0 = \frac{2P}{\pi w_0^2}. \tag{1.69}$$

The paraxial scalar Helmholtz equation is valid as long as the numerical aperture of the angle is small and as long as polarization effects do not play a role. For example when projecting a pattern through a high *numerical aperture* objective lens this assumption can be violated and the contrast of the pattern reduced. The numerical aperture (NA) is defined as

$$\mathrm{NA} = n\sin\theta, \tag{1.70}$$

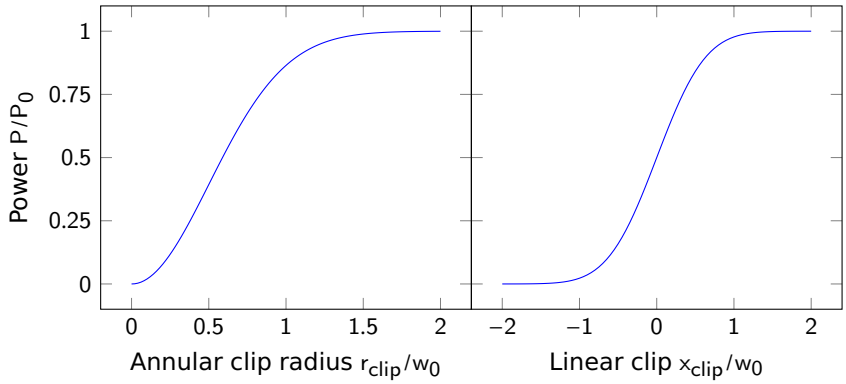

Figure 1.12: Transmitted power of a clipped Gaussian beam

where n is the index of refraction of the medium (typically $n \sim 1.0$ for air/vacuum) and θ is the largest angle ray that can be collected by the imaging system. In the paraxial limit the NA can also be written as the ratio of focal length f and the diameter D of entrance pupil: $\mathrm{NA} = n\frac{f}{2D}$.

1.4.1.1 Beam Collimation

A Gaussian beam is said to be *collimated,* when the wavefront is flat, which is the case at the *focus* of the beam ($\lim_{z\to 0} R(z) = \infty$). It is a common misconception that a beam can be collimated by focusing at "infinity". In fact with a lens of focal length f a Gaussian beam of given waist w_0 and Rayleigh length z_R can only be focused/collimated at a maximum distance of

$$d_\mathrm{max} = f\left(\frac{f}{z_\mathrm{R}} + 1\right) \overset{f \gg z_\mathrm{R}}{\approx} \frac{f^2}{z_\mathrm{R}}, \tag{1.71}$$

which for typical fiber collimation parameters is roughly equivalent to one meter. Doing so will result in a more tightly focused waist that is $1/\sqrt{2}$ smaller as the naively expected waist of $w_0' = \frac{\lambda f}{\pi w_0}$. A consistent way is to collimate the beam interferometrically, for example using a shearing interferometer. A more detailed discussion based on the transfer matrix method can be found in A.2.1.

1.4.1.2 Clipped Beams

The aperture of optical components in the experiment is always limited. This aperture could, for example, be the active area of an acousto-optical modulator, an iris, a vacuum window or even just the clear aperture of a lens. In case of a Gaussian beam with a waist of w_0 and a circular aperture with radius r_{clip} that is centered on the optical axis and only transmits the part of the beam where $\rho < r_{\text{clip}}$, the fraction of the transmitted power is given by

$$\frac{P}{P_0} = \exp\left(-2\left(\frac{r_{\text{clip}}}{w_0}\right)^2\right). \tag{1.72}$$

If, on the other hand, the beam is clipping on a linear edge, so that only light in the region $x > x_{\text{clip}}$ and $y \in \mathbb{R}$ is transmitted, the fraction is given by

$$\frac{P}{P_0} = \frac{1}{2}\left(1 + \operatorname{erf}\left(\frac{\sqrt{2}x_{\text{clip}}}{w_0}\right)\right), \tag{1.73}$$

with the error function $\operatorname{erf}(x)$ [82]. This can be useful to measure the waist of a laser beam by moving a razor blade into the beam and measuring the transmission as a function of the razor blade position. This method is particularly useful for beams larger than the typical size of a CCD/CMOS based laser beam profiler. The fractional transmitted power for the two cases of clipping is depicted in figure 1.12.

1.4.1.3 Measuring Beam Parameters

The quality of a laser beam is often quantified by the M^2 parameter [87], which is defined as

$$M_i^2 = \frac{\pi}{\lambda} d_i^{(\text{ISO})} \Theta, \tag{1.74}$$

where λ denotes the wavelength, $d^{(\text{ISO})}$ the beam *diameter* at the focus, and Θ the full far-field divergence angle. The International Organization of Standardization defines the beam diameter along the $i \in \{x, y\}$ axis (which are assumed to be the principal axes) as

$$d_i^{(ISO)} = 4\sigma_i, \tag{1.75}$$

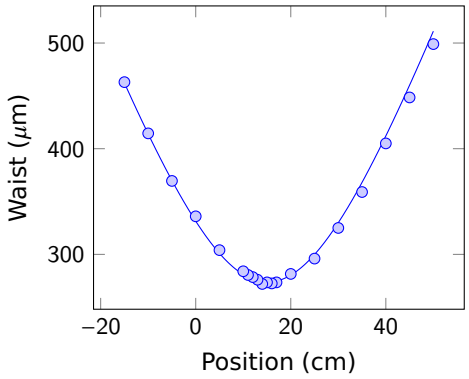

Figure 1.13: Example of measured beam waists at different positions and fitted data with $w_0 = 274(1)\,\mu\text{m}$ and $M^2 = 0.98(1)$.

with the square of the standard deviation of the power/intensity distribution

$$\sigma_x^2 = \left\langle x^2 - \langle x \rangle^2 \right\rangle = \iint \left(x^2 - \langle x \rangle^2 \right) I(x,y)\,\mathrm{d}x\,\mathrm{d}y \Big/ \iint I(x,y)\,\mathrm{d}x\,\mathrm{d}y \tag{1.76}$$

and σ_y^2 at the focus of each direction. This definition of the beam diameter is sometimes also called D4σ.

For a Gaussian beam described by (1.68) the beam diameter is

$$d^{(\mathrm{ISO})} = 2w_0 \tag{1.77}$$

and together with the far-field divergence $\Theta = 2\theta$ of (1.67) this yields an

$$M^2 = 1.$$

This is the lowest physically possible value. For a non-diffraction limited Gaussian spot with spot size w' in the focus

$$M'^2 = \frac{w'^2}{w_0^2} \geq 1.$$

Determining the beam parameters the ISO norm 11146-1 [87] requires the beam profile to be measured five times near the focus ($|z| < z_\mathrm{R}$) and five times in the far-field ($|z| > z_\mathrm{R}$). The beam parameters can then be extracted using a non-linear fit of the data points (see figure 1.13). We found that using the second moment to obtain a beam diameter gave more reliable results than trying to fit a Gaussian distribution to the profiles acquired with a

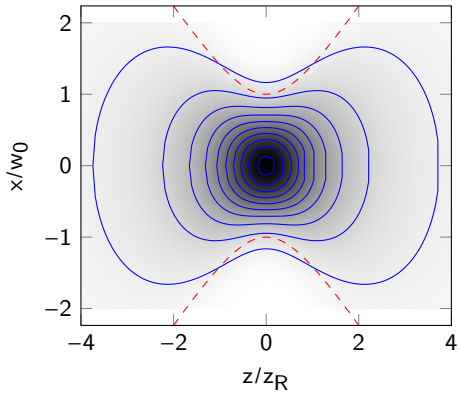

Figure 1.14: Intensity distribution of a Gaussian beam propagating along the z axis

CMOS beam profiler.

1.4.2 Travelling Wave Potentials

As seen in section 1.1.2.3 a laser beam far detuned from the atomic resonance(s) can provide a conservative potential. The strength of the potential is proportional to the intensity of the laser beam (1.68). A single red-detuned Gaussian beam alone can already confine sufficiently cold atoms in all three spatial dimensions [88], since they get attracted to the intensity maximum (see figure 1.14). The potential then has the following form

$$V_{\mathrm{odt}}(\mathbf{r}) = -V_0 \left(\frac{w_0}{w(z)}\right)^2 \exp\left(-2\frac{x^2+y^2}{w(z)^2}\right). \tag{1.78}$$

The rotating wave approximation used in 1.1.2.1 might not be justified for very large detunings when $\omega_0 + \omega_{\mathrm{L}} \sim \omega_0 - \omega_{\mathrm{L}}$. In general the trap depth taking only a single excited state into account can be obtained with the following formula [89]:

$$V_0 = \frac{3Pc^2}{w_0^2\omega_0^3}\left(\frac{\gamma}{\omega_0-\omega_{\mathrm{L}}} + \frac{\gamma}{\omega_0+\omega_{\mathrm{L}}}\right). \tag{1.79}$$

Here the counter-rotating terms are included as well and the transition matrix element is expressed as a function of the natural linewidth γ and the transition frequency ω_0. The laser frequency is denoted by ω_{L}. For lithium in a far off-resonant dipole potential created by 1064 nm light the correction due to the counter-rotating term is 23%.

As stated above for a red-detuned laser ($\omega_L < \omega_0$) the potential is attractive. Repulsive blue-detuned lasers can used for trapping as well, although this requires more complicated setups to, for example, create light sheets [90], a doughnut beam [91], or holographically generated traps [92].

Expanding the potential (1.78) around the minimum to second order and comparing it to harmonic oscillator potentials $V_{\mathrm{QHO}}(x) = \frac{1}{2}m\omega_x^2 x^2$, one can read off the trap frequencies in the longitudinal (z) and transverse (x, y) directions:

$$\omega_{\mathrm{odt,long,x}} = 2\pi\sqrt{\frac{1}{2m}\frac{V_0}{\pi^2 z_R^2}} = 2\pi\sqrt{\frac{1}{2m}\frac{V_0\lambda^2}{\pi^4 w_0^4}}, \tag{1.80}$$

$$\omega_{\mathrm{odt,trans},y} = 2\pi\sqrt{\frac{1}{m}\frac{V_0}{\pi^2 w_0^2}}. \tag{1.81}$$

The ratio of the transverse to longitudinal trap frequency is given by

$$\frac{\omega_{\mathrm{odt,trans},y}}{\omega_{\mathrm{odt,long,x}}} = \sqrt{2}\frac{\pi w_0}{\lambda}.$$

For typical low numerical aperture geometries $w_0 \gg \lambda$ and thus the trap is very elongated.

One way around this limitation is to combine two perpendicular laser beams focused onto the same position to form a crossed optical dipole trap [93]. This way it is possible to achieve a nearly spherical trap. Care must be taken to avoid interference between the two distinct beams by choosing orthogonal polarizations or better by detuning the two beams from each other. The interference pattern is then modulated with the relative detuning (see (1.86)) and averages out when this modulation is a lot faster than all trap frequencies.

Another possibility to avoid interference is to use a light source with a short coherence length such as a superluminescent diode (see 3.2.4). Superluminescent diodes are best choice of incoherent lightsources. Some other broadband lasers (e.g. pulsed lasers) might have coherence revivals or just slowly jump between discrete modes, which could heat atoms in the trap.

It is important to note that most of those lasers are temporarily incoherent, but spatially single mode. Therefore different parts of the wavefront at a given z can still perfectly

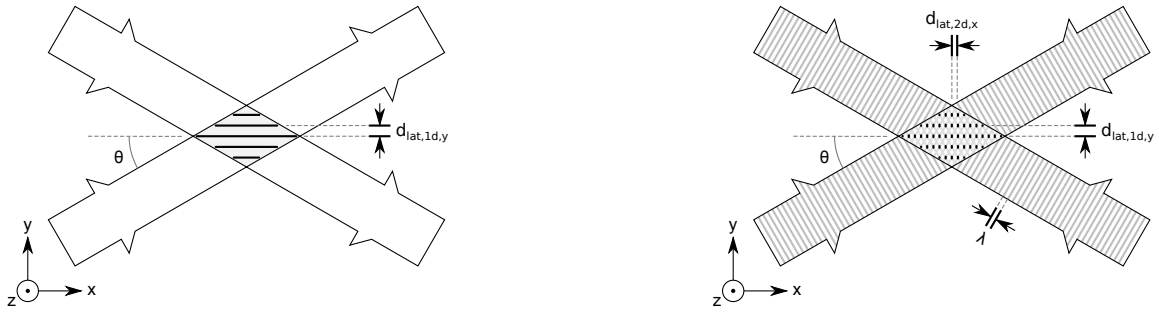

(a) Two interfering laser beams

(b) Four interfering laser beams

Figure 1.15: Geometries for standing wave potentials

interfere. This can pose a problem when an incoherent laser beam, although having short longitudinal coherence length, reflects of a surface under a shallow angle, for example the optical dipole trap used to transport atoms near the superpolished substrate in our experiment (see 3.4.5 and 3.4.7).

Another concern when designing optical traps is heating caused by scattering of the trapping laser. Although the trapping laser is usually far detuned from any atomic resonance, the atoms can still scatter that light at a rate of [89]

$$\gamma_{\mathrm{sc}}(\mathbf{r}) = -\frac{V_{\mathrm{dip}}(\mathbf{r})}{\hbar}\left(\frac{\omega_{\mathrm{L}}}{\omega_0}\right)^3\left(\frac{\gamma}{\omega_0-\omega_{\mathrm{L}}}+\frac{\gamma}{\omega_0+\omega_{\mathrm{L}}}\right). \tag{1.82}$$

This is the more general form of equation (1.31). The ratio of trap depth to scattering rate $V_{\mathrm{dip}}/(\hbar\gamma_{\mathrm{sc}})$ can be increased by going to longer wavelengths, although the laser power required to achieve a given trap depth increases as well.

1.4.3 Standing Wave Potentials

The possible feature size of traps created with a single beam is limited by the numerical aperture. To produce smaller patterns one can use two beams with a constant phase relation and let them interfere. Rather than just adding up the intensities incoherently, the electric fields add up coherently and form a *standing wave*. Its periodicity is on the order of the wavelength with a minimum value of $\lambda/2$.

1.4.3.1 Two Interfering Beams

In the simplest case we have two beams with a constant phase relation. This, for example, can be achieved by retro-reflecting a single beam back into itself. For two counter propagating plane waves with amplitudes and polarizations $\mathbf{E}_i = \hat{\epsilon}_i E_i$, angular frequency ω_i, and wavevector $k_i = 2\pi/\lambda_i = \omega/c$, the complex field is given by

$$\tilde{\mathbf{E}}(x,t) = \mathbf{E}_1 \exp\left(ik_1 x - i\omega_1 t - i\phi_1\right) + \mathbf{E}_2 \exp\left(-ik_2 x - i\omega_2 t - i\phi_2\right) \tag{1.83}$$

or the real electric field by

$$\mathbf{E}(x,t) = \mathbf{E}_1 \cos\left(k_1 x - \omega_1 t - \phi_1\right) + \mathbf{E}_2 \cos\left(-k_2 x - \omega_2 t - \phi_2\right). \tag{1.84}$$

The resulting intensity as defined via the Poynting vector [94] is

$$\begin{aligned}\mu_0 c I(x,y,t) = \mathbf{E}_1^2 \cos^2\left(k_1 x - \omega_1 t - \phi_1\right) + \mathbf{E}_2^2 \cos^2\left(-k_2 x - \omega_2 t - \phi_2\right) + \\ \mathbf{E}_1 \cdot \mathbf{E}_2 \left(\cos\left(\left(k_1 - k_2\right) x - \left(\omega_1 + \omega_2\right) t - \left(\phi_1 + \phi_2\right)\right) + \right. \\ \left. \cos\left(\left(k_1 + k_2\right) x - \left(\omega_1 - \omega_2\right) t - \left(\phi_1 - \phi_2\right)\right)\right).\end{aligned} \tag{1.85}$$

Let us assume that the two frequencies are almost equal $\omega_\mathrm{L} \equiv \omega_1, \omega_2 = \omega_1 + \Delta\omega$, $k_\mathrm{L} = k_1, k_2 = k_1 + \Delta k$ and $\phi_1 = 0, \phi_2 \equiv \phi$. Then the interference term can be written as

$$\mathbf{E}_1 \cdot \mathbf{E}_2 \left(\cos\left(2\omega_\mathrm{L} t + \phi + \Delta k x + \Delta\omega t\right) + \cos\left(2k_\mathrm{L} x + \phi + \Delta k x + \Delta\omega t\right)\right).$$

In the short-time ($\Delta\omega^{-1} \gg t \gg \omega_\mathrm{L}^{-1}$) average the time dependencies in the incoherently added fields drop out $\left\langle \cos^2(\omega_i t)\right\rangle_t = \frac{1}{2}$. The fast-oscillating term of the interference term $\left\langle \cos(2\omega_\mathrm{L} t)\right\rangle_t = 0$ (see figure 1.16) vanishes as well, so that the intensity averaged over short times is given by

$$2\mu_0 c \left\langle I(x,y,t)\right\rangle_t = \mathbf{E}_1^2 + \mathbf{E}_2^2 + 2\mathbf{E}_1 \cdot \mathbf{E}_2 \cos\left((2k_\mathrm{L} + \Delta k)x - \Delta\omega t + \phi\right). \tag{1.86}$$

To get a stationary interference pattern, a standing wave, it is required that the frequencies are equal ($\Delta\omega = 0$) and that the two polarizations have a parallel component

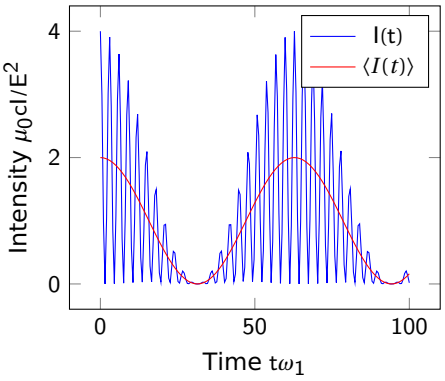

Figure 1.16: Time dependent intensity of two counterpropagating beams with $\omega_2 = 1.1\omega_1$.

($\mathbf{E}_1 \cdot \mathbf{E}_2 \neq 0$). The interference contrast is simply given by the peak-to-peak modulation

$$h \equiv 2\frac{\mathbf{E}_1 \cdot \mathbf{E}_2}{\mathbf{E}_1^2 + \mathbf{E}_2^2}. \tag{1.87}$$

In general one does not need a retro-reflector, but can use two separate actively or passively phase stabilized beams that intersect under an arbitrary angle θ (see figure 1.15a). In the following sections the symmetry axis of the two beams defines the x axis and the beams span the $x-y$ plane with the z direction perpendicular to this plane. The standing wave is modulated along the y direction, which will also be called the *longitudinal* or axial direction. The $x-z$ plane defines the *transverse* or radial directions.

In the following we will drop the assumption of infinitely large plane waves and assume Gaussian beams with linear polarization along the z axis, but still require that $w_0 \gg d_{\mathrm{lat,1d}}$ (which could easily be violated for $\theta \to 0$, see (3.17)).

Most commonly two counterpropagating beams ($\theta = \pi/2$) are used, giving rise to the potential

$$V(y,\rho) = \tilde{V}(y,\rho)\cos^2(ky), \tag{1.88}$$

with a slowly varying envelope

$$\tilde{V}(y,\rho) = V_{\mathrm{lat,1d}} \exp\left(-2\frac{\rho^2}{w(y)^2}\right) \tag{1.89}$$

and $\rho^2 = x^2 + z^2$. The second order expansion of this envelope is often called the *harmonic*

confinement.

For two coherent beams with identical wavelength λ, the intensity at the maximum is enhanced by a factor of four over a single beam trap (independent of the angle, provided that $w_0 \gg d_{\mathrm{lat,1d}}$)

$$V_{\mathrm{lat,1d}} = 4V_0. \tag{1.90}$$

This factor originates from coherent addition of the electric fields instead of intensities as shown explicitly for the counterpropagating case (1.86).

Only the parallel components of the wave vectors will interfere, leading to a lattice spacing of

$$d_{\mathrm{lat,1d,y}} = \frac{1}{2}\frac{\lambda}{|\sin\theta|}. \tag{1.91}$$

In the limit of two counterpropagating beams ($\theta = \pi/2$) the lattice spacing is $\lambda/2$, typical for most optical lattice experiments.

An important derived quantity is the so called *recoil energy*

$$E_{\mathrm{r}} = \frac{\hbar^2 k_{\parallel}^2}{2m}, \tag{1.92}$$

where $k_{\parallel} = k_\lambda \sin\theta$ and $k_\lambda = 2\pi/\lambda$. The recoil energy is the gain in kinetic energy an atom at rest of mass m would experience, if it absorbed a photon with the momentum $\hbar k_{\parallel}$. For counterpropagating beams ($\theta = \pi/2$), $k_{\parallel}$ turns into k_λ.

As in section 1.4.2 the trap frequency can be read off from the quadratic term of the expansion around the potential minimum (see also section 1.5.1.4):

$$\omega_{\mathrm{1d,long,x}} = 2\pi\sqrt{\frac{V_{\mathrm{lat,1d}}}{2md_{\mathrm{lat,1d}}^2}} = 2\pi\sqrt{\frac{2V_0}{m}}\frac{|\sin\theta|}{\lambda}. \tag{1.93}$$

Using the lattice recoil energy the trap frequency can also be written in a dimensionless form as

$$\frac{\hbar\omega_{\mathrm{1d,long,x}}}{E_{\mathrm{r}}} = 2\sqrt{\frac{V_{\mathrm{lat,1d}}}{E_{\mathrm{r}}}}. \tag{1.94}$$

In the direction of the strong transverse confinement (along the y axis) the geometrical waist is still given by the beam waist w_0. Thus the trap frequency in that direction just

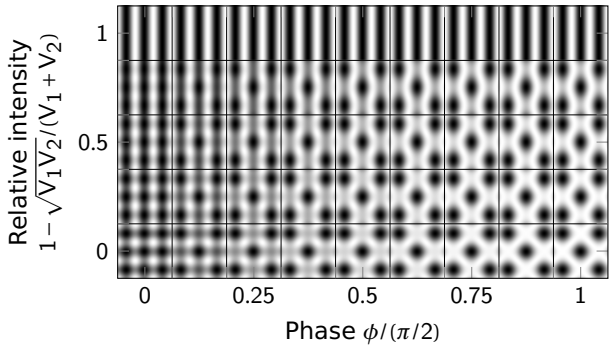

Figure 1.17: Optical potentials for different interference contrast and relative depth

corresponds to a single beam trap with a fourfold deeper trap:

$$\omega_{1\mathrm{d,trans,strong,y}} = \sqrt{4}\omega_{\mathrm{odt,trans}} = 2\pi\sqrt{\frac{1}{m}\frac{V_{\mathrm{lat,1d}}}{\pi^2 w_0^2}}. \tag{1.95}$$

The confinement in the other transverse direction is weaker:

$$\omega_{1\mathrm{d,trans,weak,x}} = 2\pi\sqrt{\frac{1}{m}\frac{V_{\mathrm{lat,1d}}}{\pi^2 z_\mathrm{R}^2}\left(\frac{1}{2}\cos^2\theta + \left(\frac{z_\mathrm{R}}{w_0}\right)^2\sin^2\theta\right)}. \tag{1.96}$$

This trap frequency approaches $\omega_{1\mathrm{d,trans,strong},y}$ in the limit of two counterpropagating beams ($\theta = \pi/2$) and $2\omega_{\mathrm{odt,long,x}}$ for near copropagating beams ($\theta \to 0$).

1.4.3.2 Four Interfering Beams

The situation gets more complex, when there are four laser beams involved. In typical optical lattice experiments with two pairs (or more) of lattice beams, interference between different axes is avoided by choosing orthogonal polarizations and sufficiently large relative detuning. This leads to the well-known egg-crate style lattice potential.

Allowing for interference between two axes can greatly enhance the lattice depth for a given laser power and also generate interesting lattice structures (see figure 1.17). For example, Uehlinger et al. [17] took advantage of the mutual interference to adiabatically double the number of lattice sites. To achieve a stationary lattice pattern, the phase between the interfering axes needs to be actively or passively stabilized.

In general the optical potential created by two pairs of interfering *plane waves* of equal

intensity with a relative phase ϕ can be described by

$$-V(\mathbf{r}) = V_{\text{lat,1d}}^{(1)} \cos^2(\mathbf{k}_1 \cdot \mathbf{r}) + V_{\text{lat,1d}}^{(2)} \cos^2(\mathbf{k}_2 \cdot \mathbf{r}) + 2\sqrt{V_{\text{lat,1d}}^{(1)} V_{\text{lat,1d}}^{(2)}} \sin\phi \cos(\mathbf{k}_1 \cdot \mathbf{r}) \cos(\mathbf{k}_2 \cdot \mathbf{r}). \tag{1.97}$$

The lattice spacing in the y direction remains unchanged from the two beam interference and is given by equation (1.91). In the perpendicular x direction the spacing is given by

$$d_{\text{lat,2d},x} = \frac{1}{2} \frac{\lambda}{|\cos\theta|}. \tag{1.98}$$

Overall the lattice depth is enhanced by the interference term in equation (1.97), which in the case of perfect interference ($\phi = \pi/2$) leads to

$$V_{\text{lat,2d}} = 16V_0 = 4V_{\text{lat,1d}}. \tag{1.99}$$

This is a significant improvement of the achievable trap frequency for a given laser power and is used in our experiment to create sufficiently deep optical lattices for fluorescence imaging (see 2.9).

Provided that the beams can be approximated as plane waves ($w_0 \gg \lambda$), the trap frequencies on each lattice site for perfect interference ($\phi = \pi/2$) are given by

$$\omega_{\text{2d},y} = 2\pi \sqrt{\frac{2V_{\text{lat,2d}}}{m}} \frac{|\cos\theta|}{\lambda} \tag{1.100}$$

and

$$\omega_{\text{2d},x} = 2\pi \sqrt{\frac{2V_{\text{lat,2d}}}{m}} \frac{|\sin\theta|}{\lambda}. \tag{1.101}$$

1.4.4 Noise-Induced Heating

Needing to hold atoms in an optical trap for a long time imposes stringent requirements on the lasers. Both frequency and amplitude fluctuations in the trapping laser can motionally excite the trapped atoms and in the worst case heat them out of the trap. Especially for quantum simulation of the Hubbard model (see 1.5.4) one has to ensure that the atoms stay in the lowest band of the optical lattice for the duration of the experiment.

Savard et al. [95] modeled the effect of the amplitude noise by looking at the rate at which a single atom in an harmonic trap with a fluctuating trap frequency $\omega_{\text{trap}}(1+\epsilon(t))$ gets excited. For small fluctuations the rate at which atoms get excited from the ground vibrational state to the second excited vibrational state is

$$\Gamma^{(\text{AM})}_{\nu=0\to\nu=2} = \frac{\pi}{8}\omega^2_{\text{trap}} S_{\text{AM}}(2\omega_{\text{trap}}). \tag{1.102}$$

Here $S_{\text{AM}}(2\omega_{\text{trap}})$ is the single-sided relative power-spectral density of the laser intensity (often also called *residual intensity noise*, given in units of $^{\text{dBc}}/_{\text{Hz}}$) at the twice the trap frequency. There is no contribution to heating from noise directly at the trap frequency. In the perturbative regime modulation of the potential with even parity cannot drive transitions between adjacent vibrational levels. Heating caused by intensity fluctuations causes an exponential rise of the temperature since the rate increases for higher excited states $\nu > 0$.

Another source of noise are pointing fluctuations of the trap center $V(x) = \frac{1}{2}m\omega_{\text{trap}}(x - \epsilon_x(t))^2$. Besides mechanical vibrations on optical components that alter the transverse pointing of a laser beam, frequency fluctuations of the laser itself can cause a shift in the longitudinal position of an optical lattice. For a counterpropagating one-dimensional optical lattice the nth lattice site is $x_0 = n\lambda/2 = \pi nc/\omega_{\text{L}}$ away from the retro-reflector. To first order a small fluctuation $\delta\omega_{\text{L}}$ shifts that position by

$$\delta x = x_0 \frac{\delta\omega_{\text{L}}}{\omega_{\text{L}}}. \tag{1.103}$$

The rate at which pointing noise drives transitions between the ground and the first excited vibrational state is [96]

$$\Gamma^{(\text{XM})}_{\nu=0\to\nu=1} = \frac{\pi}{2\hbar} m\omega^3_{\text{trap}} S_{\text{XM}}(\omega_{\text{trap}}). \tag{1.104}$$

Here $S_{\text{XM}}(\omega)$ is the power-spectral density of the position fluctuations (in units of $^{\text{m}^2}/_{\text{Hz}}$) which is connected to the frequency power-spectral density $S_{\text{FM}}(\omega)$ (in units of $^{(2\text{ßHz})^2}/_{\text{Hz}}$) via equation (1.103):

$$S_{\text{XM}}(\omega) = \left(\frac{x_0}{\omega_{\text{L}}}\right)^2 S_{\text{FM}}(\omega). \tag{1.105}$$

The frequency fluctuations of a laser can be modelled as white Gaussian noise $\epsilon_\omega(t)$

(up to a certain bandwidth). This kind of frequency noise corresponds to the $1/f^2$ term in the phase noise and gives rise to a Lorentzian frequency profile with linewidth $\Delta\omega$. The frequency noise power spectral density is given by [97]

$$S_{\mathrm{FM}}(\omega) = \frac{2}{\pi}\int_0^\infty \mathrm{d}\tau\, \cos(\omega\tau)\, \langle \epsilon_\omega(t)\epsilon_\omega(t+\tau)\rangle = \Delta\omega. \tag{1.106}$$

Frequency noise can get converted to amplitude noise by components that have a frequency/wavelength dependence of their transfer function (for example cavities). Unintentional reflections off optical componentents can act as resonator as well.

For ^{6}Li atoms in an optical lattice with a 1 MHz trap frequency and a distance of 10 cm from the retro-reflector created by a laser with 1 MHz linewidth and 100 $^{\mathrm{dBc}}/_{\mathrm{Hz}}$ residual amplitude noise would experience heating at a rate of $\Gamma^{(\mathrm{AM})}_{\nu=0\to\nu=2} = 2\pi\cdot 248\,\mathrm{Hz}$ and $\Gamma^{(\mathrm{XM})}_{\nu=0\to\nu=1} = 2\pi\cdot 117\,\mathrm{Hz}$. These results emphasize the importance of having lasers with extremely low residual amplitude noise ($< -130\,^{\mathrm{dBc}}/_{\mathrm{Hz}}$) and small distance between the atoms and the retro reflector, when one is working with high trap frequencies. Acoustic noise become less of a problem.

1.5 Physics Of Optical Lattices

Optical lattices are more than just arrays of microtraps. The symmetry of the system drastically changes: the continous translation symmetry is broken by the lattice potential.

1.5.1 Band Structure Calculation

This broken symmetry changes the dispersion (i.e. relations between momentum and energy) of a single delocalized particle in an optical lattice.

1.5.1.1 d-Dimensional Square Lattice

For infinite systems described by the Hamiltonian

$$\hat{H} = \frac{1}{2m}\hat{\mathbf{p}}^2 + \hat{V}(\hat{\mathbf{r}}), \tag{1.107}$$

with a potential energy term that is periodic in space

$$\hat{V}(\mathbf{r}) = \hat{V}(\mathbf{r}+\mathbf{R}), \tag{1.108}$$

the wavefunctions $\phi_{\mathbf{q}}^{(n)}(\mathbf{r})$ inherit the periodicity

$$\phi_{\mathbf{q}}^{(n)}(\mathbf{r}) = \phi_{\mathbf{q}}^{(n)}(\mathbf{r}+\mathbf{R}) \tag{1.109}$$

and can be written in the following form (known as BLOCH'S THEOREM [98]):

$$\phi_{\mathbf{q}}^{(n)}(\mathbf{r}) = \exp\left(\frac{i}{\hbar}\mathbf{q}\cdot\mathbf{r}\right) u_{\mathbf{q}}^{(n)}(\mathbf{r}). \tag{1.110}$$

Here $\mathbf{R}$ denotes a Bravais lattice vector. For a three-dimensional square lattice with lattice spacing a it is given by

$$\mathbf{R}_{\square} = a\left(i\hat{\mathbf{e}}_x + j\hat{\mathbf{e}}_y + k\hat{\mathbf{e}}_z\right)\ \forall i,j,k \in \mathbb{Z}. \tag{1.111}$$

Using Bloch's theorem, the Schrödinger equation reads

$$\hat{H}' u_{\mathbf{q}}^{(n)}(\mathbf{r}) = E_{\mathbf{q}}^{(n)} u_{\mathbf{q}}^{(n)}(\mathbf{r}), \tag{1.112}$$

with a slightly modified Hamiltonian

$$\hat{H}' = \frac{1}{2m}(\hat{\mathbf{p}}+\mathbf{q})^2 + V(\mathbf{r}). \tag{1.113}$$

On a square lattice the periodicity of the problem suggests to switch to a d-dimensional discrete Fourier basis to get a general solution numerically.

$$u_{\mathbf{q}}^{(n)}(\mathbf{r}) = \sum_{l_1=-\infty}^{\infty}\sum_{l_2=-\infty}^{\infty}\cdots\sum_{l_D=-\infty}^{\infty} c_{\mathbf{q},\mathbf{l}}^{(n)} \exp\left(i\sum_{i=1}^{d} l_i\kappa_i r_i\right)$$

$$V(\mathbf{r}) = \sum_{s_1=-\infty}^{\infty}\sum_{s_2=-\infty}^{\infty}\cdots\sum_{s_D=-\infty}^{\infty} V_{\mathbf{s}} \exp\left(i\sum_{i=1}^{d} s_i\kappa_i r_i\right)$$

It can be seen that the potential term couples different $\mathbf{l}$ because of the $\exp(is_i\kappa_i r_i)$ phase factors, (i.e. resulting in off diagonal terms in the Hamiltonian matrix in the $\{\exp(in_i\kappa_i r_i)\,|$

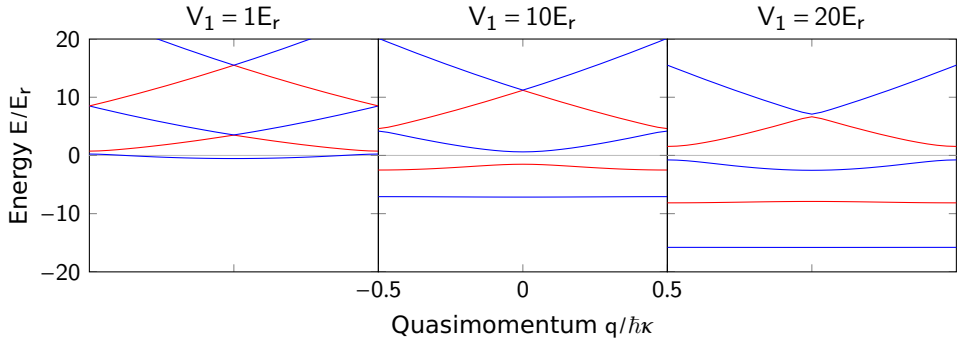

Figure 1.18: Bandstructure of an one-dimensional lattice for various depths

$i \in \{1, 2, \ldots, d\}, n_i \in \mathbb{Z}\}$ basis), but most $V_{\mathbf{r}}$ are going to be equal to zero.

$$V(\mathbf{r}) u_{\mathbf{q}}^{(n)}(\mathbf{r}) = \sum_{\mathbf{l},\mathbf{s}} V_{\mathbf{s}} c_{\mathbf{q},\mathbf{l}}^{(n)} \exp\left(i \sum_{i=1}^{d} (l_i + s_i) \kappa_i r_i \right)$$

In this basis the kinetic term turns into

$$\frac{1}{2m} (\hat{\mathbf{p}} + \mathbf{q})^2 u_{\mathbf{q}}^{(n)}(\mathbf{r}) = \sum_{\mathbf{l}} \sum_{j=1}^{d} \frac{\hbar^2 \kappa_j^2}{2m} \left(l_j + \frac{q_j}{\hbar \kappa_j} \right)^2 c_{\mathbf{q},\mathbf{l}}^{(n)} \exp\left(i \sum_{i=1}^{d} l_i \kappa_i r_i \right).$$

The variable $\mathbf{q}$ is called the *quasimomentum.*

1.5.1.2 One-Dimensional Lattice

In the case of a one-dimensional optical lattice, such as the lattice described in section 1.4.3.1, the potential along the direction of the optical lattice is typically written as

$$-V(x) = V_1 \cos^2(kx) = V_1 \left(\frac{1}{2} + \frac{1}{4} \exp(i2kx) + \frac{1}{4} \exp(-i2kx) \right), \tag{1.114}$$

where $k = 2\pi/\lambda$ for counterpropagating beams or $k = 2\pi/(2d_{\mathrm{lat,1d}})$ in the general case (see equation (1.91)). By substituting $\kappa = 2k$ one can calculate the elements of the Hamiltonian matrix:

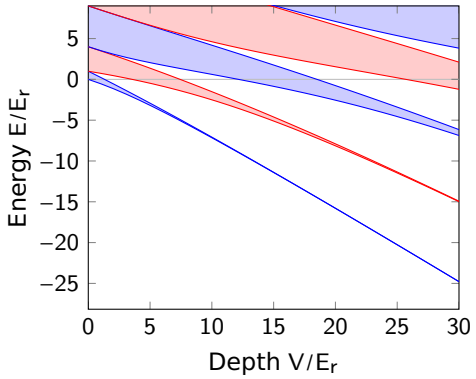

Figure 1.19: Bands for various lattice depths in an one-dimensional lattice

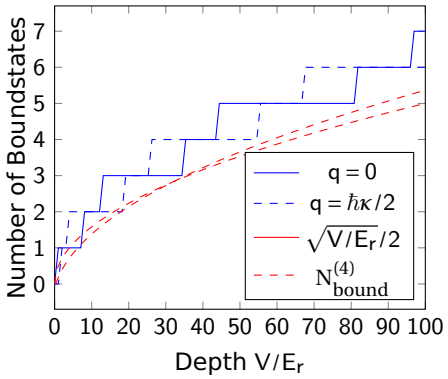

Figure 1.20: Number of bound states in a one-dimensional lattice

$$\mathbf{H}_{l,l'} = \begin{cases} 4E_\mathrm{r}\left(l_j + \frac{q_j}{\hbar\kappa}\right)^2 - \frac{V_1}{2} & \forall l = l' \\ -\frac{1}{4}V_1 & |\Delta l| = 1 \\ 0 & \text{else} \end{cases} \tag{1.115}$$

with a lattice recoil energy of $E_\mathrm{r} = \frac{\hbar^2 k^2}{2m} = \frac{1}{4}\frac{\hbar^2\kappa^2}{2m}$. The first Brillouin zone extends from $-\hbar\kappa/2$ to $\hbar\kappa/2$. To perform numeric calculations the Hamiltonian matrix needs to be truncated by only including elements for $l = -l_\mathrm{max} \ldots + l_\mathrm{max}$.

For weak lattices the bands are still very similar the parabolic free particle dispersion

$$E_\mathrm{free} = \frac{p^2}{2m}$$

folded into the first Brillouin zone. The lattice potential then couples the quasimomentum parabolas differing by $|\Delta l| = 1$ and opens up gaps at the intersections. Now only certain bands of energies levels are allowed (figure 1.19), hence the name *band structure* . In the limit of very deep lattices the bands become flat and approach equally spaced quantum harmonic oscillator levels (figure 1.18).

Number Of Bound States The fact that band become flat can be used to approximate the number of bound states in deep lattices. For a given trap depth V_1 and a harmonic oscillator

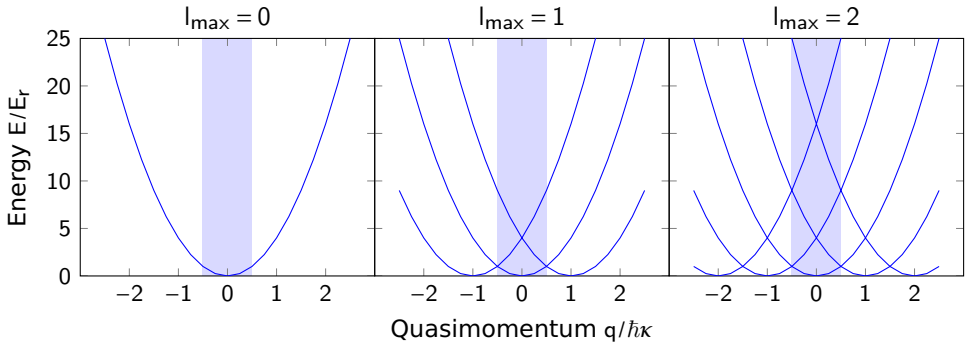

Figure 1.21: Energy spectrum for almost free particles at $V_0 \to 0$, calculated for different cutoffs $l_{\max} = 0, 1, 2$. The first Brillouin zone is highlighted.

trap frequency of ω_{1d} (equation (1.94)) there are roughly

$$N^{(2)}_{\text{bound}} = \frac{V_1}{\hbar\omega_{1d}} = \frac{1}{2}\sqrt{\frac{V_1}{E_r}} \tag{1.116}$$

energy levels below the threshold, neglecting the zero-point energy and anharmonicity. This equation slightly underestimates the exact number of bound states (figure 1.20). Including the quartic term (see 1.5.1.4) in this calculation yields

$$N^{(4)}_{\text{bound}} = \frac{1}{2}\left(4\sqrt{\frac{V_1}{E_r}} - \sqrt{8\frac{V_1}{E_r} - 1} - 1\right), \tag{1.117}$$

which improves the accuracy, but is less useful for "back-off-the-envelope" calculations.

The Meaning Of $l_{\max}$ As stated above the lattice potential couples the neighboring parabolas and creates avoided crossings. Since the number of states is conserved, there will be $2l_{\max} + 1$ states. Hence, to get accurate bound state energies $l_{\max}$ should be chosen such that

$$l_{\max} > \frac{1}{4}\sqrt{\frac{V_1}{E_r}}. \tag{1.118}$$

1.5.1.3 Two-Dimensional Square Lattice

Most optical lattice experiments are setup such that orthogonal lattice beams do not mutually interfere. The Hamiltonian then is separable and can be solved independently for each

lattice direction. Allowing mutual interference between two lattice axes gives rise to a potential of the form

$$\begin{aligned} -V(\mathbf{r}) &= V_1\cos^2(k_1r_1) + V_2\cos^2(k_2r_2) + 2\sqrt{V_1V_2}\sin\phi\cos(k_1r_1)\cos(k_2r_2) = \\ &= \frac{V_1+V_2}{2} + \frac{V_1}{4}\left[\exp\left(2ik_1r_1\right) + \exp\left(-2ik_1r_1\right)\right] + \frac{V_2}{4}\left[\exp\left(2ik_2r_2\right) + \exp\left(-2ik_2r_2\right)\right] + \\ &\qquad \frac{\bar{V}\sin\phi}{2}\left[\exp\left(ik_1r_1 + ik_2r_2\right) + \exp\left(ik_1r_1 - ik_2r_2\right) + \right. \\ &\qquad \left. \exp\left(-ik_1r_1 + ik_2r_2\right) + \exp\left(-ik_1r_1 - ik_2r_2\right)\right], \end{aligned} \tag{1.119}$$

where $\bar{V} = \sqrt{V_1V_2}$ denotes the geometric mean of the two potential depths. The relative phase between the lasers of the two axes is denoted by ϕ. Reading of the matrix elements, we can write the Hamiltonian in matrix form:

$$\mathbf{H}_{\mathbf{l},\mathbf{l}'} = \begin{cases} \sum_{j=1}^{2}\left(\frac{\hbar^2k_j^2}{2m}\left(l_j + \frac{q_j}{\hbar k_j}\right)^2 - \frac{V_j}{2}\right) & \forall \mathbf{l} = \mathbf{l}' \\ -\frac{1}{2}\bar{V}\sin\phi & |\Delta l_1| = 1 \wedge |\Delta l_2| = 1 \\ -\frac{1}{4}V_1 & |\Delta l_1| = 2 \wedge \Delta l_2 = 0 \\ -\frac{1}{4}V_2 & \Delta l_1 = 0 \wedge |\Delta l_2| = 2 \\ 0 & \text{else} \end{cases} . \tag{1.120}$$

In comparison to equation (1.120) the kinetic energy is parameterized with the laser wavevectors k_i. The first Brillouin zone now extends from $-\hbar k_i$ to $\hbar k_i$.

In the special case of $\phi = 0$ we only have terms oscillating at $2k_i$. Thus the primitive unit cell is effectively halved and the Hamiltonian factorizes into two decoupled subspaces per spatial dimension, one for even and one for odd l_is. In other words, we are solving the same problem twice, but shifted by $k_i/2$ in quasimomentum space, and yields the same result as the one dimensional lattice.

Similar to the one dimensional case we truncate our Hilbert space by limiting the maximum $\mathbf{l}$ and numerically solve the problem by diagonalizing the truncated Hamiltonian matrix. Figure 1.22 shows the density of states in a two dimensional lattice as a function of the interference between the two lattice beams $\sin\phi$.

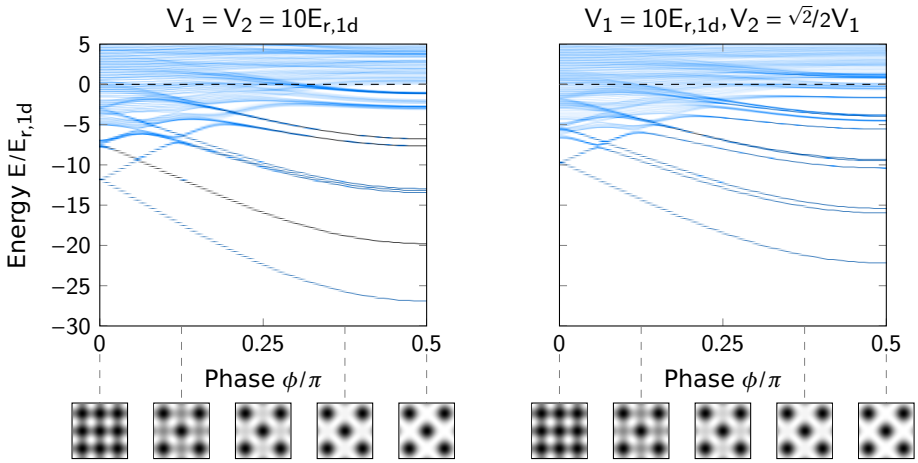

Figure 1.22: Density of states in a two-dimensional square lattice for varying interference

1.5.1.4 Anharmonicity

Only for deep lattices ($V_1 \gg \hbar\omega_{1d} \gg E_r$ or $V_1/E_r \gg 1$) and only in the lowest bands the energy levels can be approximated as quantum harmonic oscillator eigenenergies.

Expanding the potential energy of a one dimensional lattice (see equation 1.114) around a minimum yields:

$$V(x) = -V_1 \cos^2(kx) = -V_1 + V_1 k^2 x^2 - \frac{1}{3} V_1 k^4 x^4 + \mathcal{O}(x^6) \tag{1.121}$$

The trap frequency can be read off by comparing the quadratic coefficient with the potential energy term in the Hamiltonian of the quantum harmonic oscillator (equation (1.35)):

$$\omega = \sqrt{\frac{2V_1}{m}} k \qquad\qquad \frac{\hbar\omega}{E_r} = 2\sqrt{\frac{V_1}{E_r}} \tag{1.122}$$

In second order perturbation theory the unperturbed harmonic oscillator eigenstates $\psi_\nu(x)$ (see equation (1.37)) get shifted by

$$\Delta E_\nu = -\frac{1}{3} V_1 k^4 \langle \psi_\nu | x^4 | \psi_\nu \rangle = -\frac{1}{8} \left(\nu^2 + \nu + \frac{1}{2} \right) \frac{\hbar^2 \omega^2}{V_1} \tag{1.123}$$

by the quartic term. In dimensionless units this shift reads

$$\frac{\Delta E_\nu}{E_r} = -\frac{1}{2}(\nu^2 + \nu + \frac{1}{2}). \tag{1.124}$$

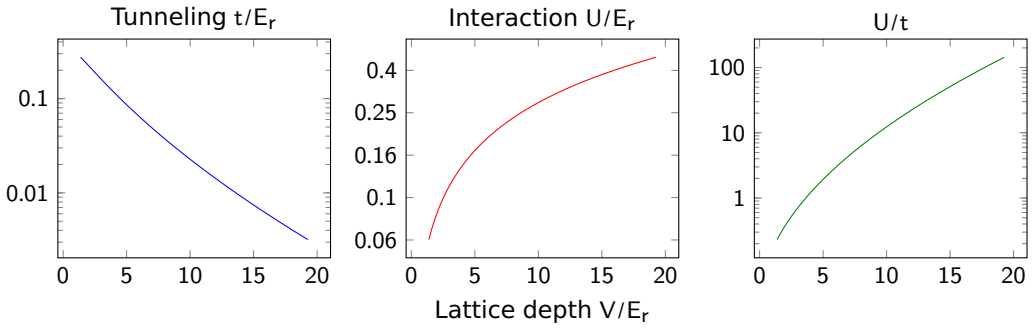

Figure 1.23: Tunneling and interaction for various lattice depths. For the interaction isotropic trap frequencies and a scattering length of $a = 100a_0$ were assumed.

That, in turn, means that the transition frequencies between two states $|\nu\rangle \rightarrow |\nu+1\rangle$ are red shifted by

$$\frac{\Delta E_\nu - \Delta E_{\nu+1}}{E_\mathrm{r}} = \nu + 1. \tag{1.125}$$

1.5.2 Tight Binding Model

For most optical lattice experiments the atoms are (more or less) localized to a lattice site with only little (but not negligible) wavefunction overlap with its nearest neighbor. Rather than describing the state with periodic Block waves $\phi_\mathbf{q}^{(n)}(\mathbf{r})$ of infinite extend, it is more intuitive to choose wave functions that are well localized on each lattice site $\mathbf{R}$. A common choice are the so-called *Wannier functions*, which are connected to the Bloch waves via a discrete Fourier transformation and are also an orthogonal basis:

$$w^{(n)}(\mathbf{r}-\mathbf{R}) = \frac{1}{\sqrt{\mathcal{N}}} \sum_{\mathbf{q}\in\mathrm{BZ}} \exp\left(-\frac{i}{\hbar}\mathbf{q}\cdot\mathbf{R}\right) \phi_\mathbf{q}^{(n)}(\mathbf{r}). \tag{1.126}$$

Here $\mathcal{N}$ is a normalization constant.

Assuming we already know the Wannier functions we can now calculate the band structure by simply evaluating the expectation values of the Hamiltonian (1.107) [99].

$$\begin{aligned} E^{(n)}(\mathbf{q}) = \int \mathrm{d}\mathbf{r}\, \phi_\mathbf{q}^{(n)}(\mathbf{r})^* \hat{H} \phi_\mathbf{q}^{(n)}(\mathbf{r}) &= \sum_\mathbf{R} \exp\left(\frac{i}{\hbar}\mathbf{q}\cdot\mathbf{R}\right) \int \mathrm{d}\mathbf{r}\, w^{(n)}(\mathbf{r}-\mathbf{R})^* \hat{H} w^{(n)}(\mathbf{r}) \\ &= E_0^{(n)} + \sum_{\mathbf{R}\neq 0} t^{(n)}(\mathbf{R}) \exp\left(\frac{i}{\hbar}\mathbf{q}\cdot\mathbf{R}\right), \end{aligned} \tag{1.127}$$

with the *tunneling amplitude* t between sites that are $\mathbf{R} \neq 0$ apart

$$t^{(n)}(\mathbf{R}) = \int \mathrm{d}\mathbf{r}\, w^{(n)}(\mathbf{r}-\mathbf{R})^*(\frac{\hat{\mathbf{p}}^2}{2m} + V(\mathbf{r}))w^{(n)}(\mathbf{r}) \tag{1.128}$$

and the diagonal term

$$E_0^{(n)} = \int \mathrm{d}\mathbf{r}\, w^{(n)}(\mathbf{r})^*(\frac{\hat{\mathbf{p}}^2}{2m} + V(\mathbf{r}))w^{(n)}(\mathbf{r}). \tag{1.129}$$

Vice versa the tunneling amplitudes are given by the Fouier coefficients of the band structure (1.127). The nearest-neighbor tunneling is described by the coefficient $t_{\mathrm{nn}}^{(n)} \equiv t^{(n)}(\mathbf{R} = \pm\hat{e}_i)$. In a d-dimensional lattice the band structure (1.127) can be expanded in orders of the tunnel coupling:

$$E^{(n)}(\mathbf{q}) = E_0^{(n)} - 2t_{\mathrm{nn}}^{(n)} \sum_{i=1}^{d} \cos(q_i R_i/\hbar) + \mathcal{O}(\text{next-nearest neighbor tunneling}).$$

In the *tight-binding* limit, where the tunneling is dominated by the direct nearest-neighbor tunneling, the tunneling rate is given by the band width $\Delta E^{(n)}$

$$t_{\mathrm{nn}}^{(n)} = \frac{1}{4d}\Delta E^{(n)}. \tag{1.130}$$

An alternative derivation using second quantized notation can be found in [100]. There also exists an analytic expression for the nearest-neighbor tunneling in the ground band that is valid for one-dimensional lattices deeper than $V_1 > 15E_\mathrm{r}$ [101]:

$$\frac{t_{\mathrm{nn}}^{(0)}}{E_\mathrm{r}} \approx \frac{4}{\sqrt{\pi}} \left(\frac{V_1}{E_\mathrm{r}}\right)^{3/4} \exp\left(-2\sqrt{\frac{V_0}{E_\mathrm{r}}}\right). \tag{1.131}$$

For the purpose of calculating the energy offset $E_0^{(n)}$, Wannier functions can be approximated as harmonic oscillator eigenstates. For an one dimensional lattice (1.121) this yields

$$\frac{E_0^{(n)}}{E_\mathrm{r}} \approx 2\sqrt{\frac{V_1}{E_\mathrm{r}}}n - \frac{V_1}{E_\mathrm{r}}. \tag{1.132}$$

To calculate tunneling rates the harmonic oscillator approximation is insufficient [102]. The probability amplitude on neighboring lattice sites would be underestimated.

If we limit ourselves to the ground band with only nearest-neighbor tunneling $t \equiv t_{\mathrm{nn}}^{(0)}$,

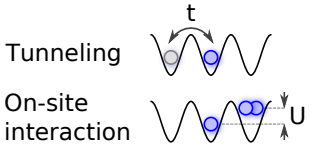

Figure 1.24: Processes in the Bose-Hubbard model

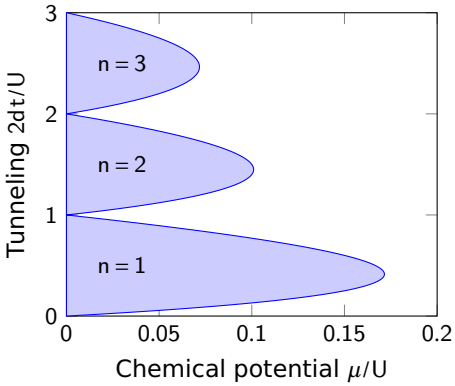

Figure 1.25: Phase diagram of the Bose-Hubbard model. The blue area represents the Mott insulating phase.

we can collapse all the single-particle physics into a second quantized Hamiltonian, the basis for the Hubbard model,

$$\hat{H}_0 = -t \sum_{\langle i,j \rangle} \hat{a}_i^\dagger \hat{a}_j, \tag{1.133}$$

where $\hat{a}_i$,$\hat{a}_i^\dagger$ are the annihilation and creation operator of Wannier functions on site i. The sum runs over all nearest neighbor pairs i, j, where i, i is excluded.

1.5.3 Bose-Hubbard Model

Extending this problem to the many-body world we need to distinguish between fermions and bosons. In the latter case we get the *Bose-Hubbard model*, which is described by the following Hamiltonian [103]:

$$\hat{H}_{\mathrm{BH}} = -t \sum_{\langle i,j \rangle} \hat{b}_i^\dagger \hat{b}_j + \frac{U}{2} \sum_i \hat{n}_i(\hat{n}_i - 1) + \sum_i \epsilon_i \hat{n}_i. \tag{1.134}$$

The tunneling amplitude t is identical to the single particle case above. U describes the *on-site interaction* of $\hat{n}_i = \hat{b}_i^\dagger \hat{b}_i$ with each other on lattice site i. $\hat{b}, \hat{b}^\dagger$ are the bosonic annihilation and creation operators obeying the commutator relation $[\hat{b}_i, \hat{b}_j^\dagger] = \delta_{i,j}$. The Hamiltonian also allows the lattice sites to have an external potential that manifests itself as different energy

offsets (without modifying the tunneling amplitudes)

$$\epsilon_i = \int \mathrm{d}\mathbf{r}\, w^{(0)}(\mathbf{r}-\mathbf{R}_i)^* V_{\mathrm{ext}}(\mathbf{R}_i) w^{(0)}(\mathbf{r}-\mathbf{R}_i) \approx V_{\mathrm{ext}}(\mathbf{R}_i). \tag{1.135}$$

The last approximation assumed that the external potential only varies slowly over the extent of the Wannier function. In optical lattices the external potential is usually present and gives rise to the harmonic confinement caused by the Gaussian envelope of the lattice potential given in equation (1.89). It can be approximately cancelled with a blue-detuned laser creating a repulsive potential in the center of the lattice or by shaping the envelope of a red-detuned potential.

The on-site interaction for a short-range δ pseudo-potential (see 1.2) is given by

$$U = a\frac{4\pi\hbar^2}{m}\int \mathrm{d}\mathbf{r}\, \left|w^{(0)}(\mathbf{r})\right|^4. \tag{1.136}$$

Here a denotes the interparticle scattering length. In the tight-binding regime we, again, can approximate the Wannier functions as harmonic oscillator eigenstates with the trap frequencies $\omega_x, \omega_y, \omega_z$, which are a good approximation for the on-site density distribution. In this limit the on-site interaction reads

$$U \approx a\frac{4\pi\hbar^2}{m}\left(\frac{m}{2\pi\hbar}\right)^{3/2}\sqrt{\omega_x\omega_y\omega_z}. \tag{1.137}$$

In the uniform case ($\epsilon_i = 0$), at low temperatures ($T \ll t^2/U$), and for *repulsive* interactions this system exhibits a quantum phase transition from a superfluid (Bose-Einstein condensate) to a Mott insulator [103]. As long as the kinetic energy dominates ($t \gg U$) the system will stay superfluid with a delocalized Bloch wavefunction. In the interaction dominated regime ($U \gg t$) atoms prefer to localize on each lattice site and form an insulating state with a fixed atom number per lattice site. This phase transition has been extensively studied in various experiments [9, 104, 35] and really set off quantum simulation with ultracold atoms in optical lattices.

The choice of U and t is not completely arbitrary. The Hubbard model is a single band model, therefore the admixture of the excited bands needs to be negligible, i.e. $U, t \ll \omega_i$.

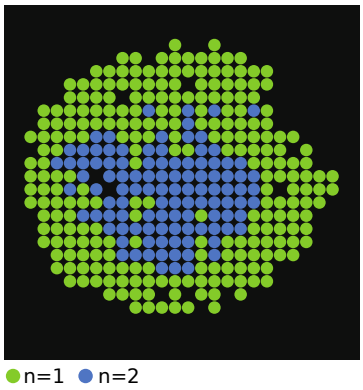

Figure 1.26: In-situ images of bosonic atoms in a two-dimensional lattice in the Mott insulating phase (from [106])

In an inhomogenious system, as it usually is the case in optical lattice experiments, the two phases coexists. If the harmonic confinement is small compared to all the other energy scales, the system can be interpreted as being locally uniform. Mathematically the consequence of the local density approximation is that we can introduce a local chemical potential $\mu(\mathbf{r}) = \mu - V_{\text{ext}}(\mathbf{r})$ (see also 1.3.2.2). Therefore a single experimental representation has information about both phases (cut through the phase diagram, see figure 1.25, equations from [105]) and results in the so-called *wedding cake structure* of the density distribution [103] (see figure 1.26).

1.5.4 Fermi-Hubbard Model

Whereas the bosonic version of the Hubbard model (1.5.3) is typically written for a single species, the original Hubbard model, the Fermi-Hubbard model for spin-1/2 particles [44] adds an additional spin degree of freedom $\sigma \in \{\uparrow, \downarrow\}$:

$$\hat{H}_{\text{FH}} = -t \sum_{\langle i,j\rangle,\sigma} \hat{c}_i^\dagger \hat{c}_j + U \sum_i \hat{n}_{i,\uparrow}\hat{n}_{i,\downarrow} + \sum_i \epsilon_i(\hat{n}_{i,\uparrow} + \hat{n}_{i,\downarrow}). \tag{1.138}$$

Here the creation and annihilation operators $\hat{c}_{i,\sigma}^\dagger, \hat{c}_{i,\sigma}$ obey the fermionic anti-commutator relations $\{\hat{c}_{i,\sigma}, \hat{c}_{j,\sigma'}^\dagger\} = \delta_{i,j}\delta_{\sigma,\sigma'}$. The on-site interaction only describes the interaction between atoms with opposite spin $U \equiv U_{\uparrow\downarrow}$. Having atoms with identical spins on the same lattice site (in the same band) is not permitted by the Pauli exclusion principle.

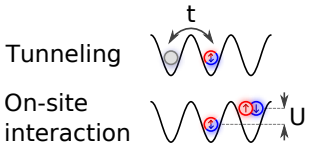

Figure 1.27: Processes in the Fermi-Hubbard model

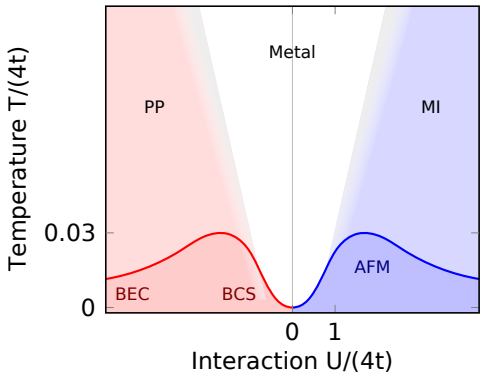

Figure 1.28: Qualitative phase diagram of the two-dimensional Fermi-Hubbard Model at half filling [107, 46]

Even in the non-interacting case $U = 0$ the system has an insulating phase at *unity filling*, the band insulator, *i.e.* $\langle \hat{n}_{i,\sigma} \rangle = 1$ atom per site per spin state, but with $\langle \hat{n}_{i,\uparrow} + \hat{n}_{i,\downarrow} \rangle = 2$ atoms per site in total. To add another particle the energy on the order the band spacing is required. For every other filling factor the system is a metal.

The regime that is theoretically well understood is at *half filling*, i.e. $\langle n_{i,\sigma} \rangle = \frac{1}{2}$ atom per site per spin state, $\langle \hat{n}_{i,\uparrow} + \hat{n}_{i,\downarrow} \rangle = 1$ atom per site. For small *attractive* interactions ($U < 0$, $t > |U|$) and low temperatures (in two-dimensions $k_B T \lesssim 4t \exp(-8t/|U|)$ [46]) the system is a BCS superfluid on a lattice. On the other hand for large attractive interactions ($t < |U|$) the atoms preferentially form bound pairs of fermions, which behave as composite bosons with (repulsive) hard-core interactions that only pair tunnel in a second order process at a rate $\propto t^2/|U|$. Below a critical temperature of $k_B T \lesssim t^2/|U|$ these pairs Bose-condense and form a charge-density wave (CDW) [108]. Above that temperature atoms are believed to form pre-formed pairs [107].

On the *repulsive* side interactions are governed by the *superexchange* interactions, where one atom virtually hops to its neighboring site at a rate t, interacts with the atom on that site with the interaction energy U (provided it has the opposite spin), and hops back at a rate t. This can also be interpreted as an off-resonantly driven two-level system with an effective Rabi frequency of $\propto t^2/U$. In a two dimensional square lattice an atom can interact with

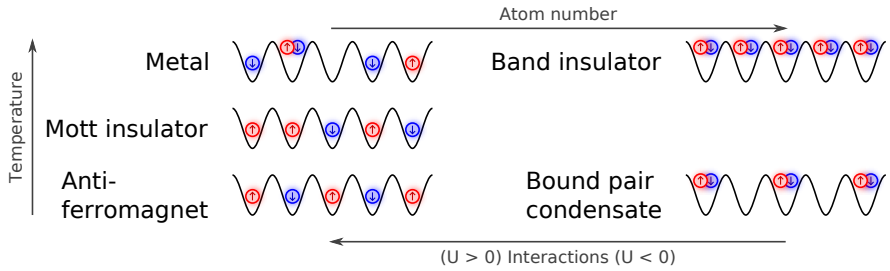

Figure 1.29: Various phases of the Fermi-Hubbard model

its $2d = 4$ nearest neighbors. Strong interactions $t > U$ are going to drive the system into a *Mott insulator* with one atom per site. This has experimentally been first studied in the groups of Tilman Esslinger [109] and Immanuel Bloch [110]. For low enough temperatures ($T < T_{\text{Neel}}$, see [111]) the Mott insulator is going to exhibit spin ordering as well and form an *anti-ferromagnet* with a checker-board pattern, which has yet to be demonstrated in an optical lattice experiment. Several groups are working on detection schemes that do not rely on single-site imaging [112, 50]. As mentioned in the introductory chapter the main experimental focus is on the repulsive Fermi Hubbard model, as it may exhibit a *d*-wave superfluidic phase for hole-doped samples [49].

Mathy and Huse [111] also predict a phase separated ferro-magnetic phase for strong interactions in shallow lattices, where the direct nearest-neighbor interaction caused by the Wannier function overlap between neighboring lattice sites favors same spins on neighboring sites. This is one example of an effect that could be observed in our experiment and that goes beyond the Fermi-Hubbard description with only on-site interactions.

1.5.4.1 Spin Mapping: The Heisenberg Model

At half-filling and at low temperatures ($T < t^2/U$) the atoms in the repulsive Fermi Hubbard model can be also understood as localized spins, that only interact via the superexchange interaction $J = 4t^2/U$. The spin model is a convenient picture for quantum information processing. For fermions this gives rise to an isotropic anti-ferromagnetic Heisenberg (XXX)

Hamiltonian [113]

$$\hat{H}_J = J \sum_{\langle i,j \rangle} \hat{\mathbf{S}}_i \cdot \hat{\mathbf{S}}_j, \tag{1.139}$$

with the spin-1/2 operator in site i $\hat{\mathbf{S}}_i = \frac{1}{2}\left(\hat{\sigma}_x, \hat{\sigma}_y, \hat{\sigma_z}\right)$ and the Pauli spin matrices $\hat{\sigma}_i$.

This mapping can be easily seen for two-fermions $(\uparrow, \downarrow)$ in a double well (L, R):

$$\hat{H}^{(2)}_{\mathrm{FH}} = -t\left(\hat{c}^{\dagger}_{\mathrm{L},\uparrow}\hat{c}_{\mathrm{R},\uparrow} + \hat{c}^{\dagger}_{\mathrm{R},\uparrow}\hat{c}_{\mathrm{L},\uparrow} + \hat{c}^{\dagger}_{\mathrm{L},\downarrow}\hat{c}_{\mathrm{R},\downarrow} + \hat{c}^{\dagger}_{\mathrm{R},\downarrow}\hat{c}_{\mathrm{L},\downarrow}\right) + U\left(\hat{n}_{\mathrm{L},\uparrow}\hat{n}_{\mathrm{L},\downarrow} + \hat{n}_{\mathrm{L},\uparrow}\hat{n}_{\mathrm{L},\downarrow}\right). \tag{1.140}$$

The ground state for $t = 0$ and $U > 0$ is given by $|\psi_0\rangle = \left(|\uparrow,\downarrow\rangle - |\downarrow,\uparrow\rangle\right)/\sqrt{2}$. For now let us just consider the $|\uparrow,\downarrow\rangle$ component. Finite tunneling admixes the excited states $|\uparrow\downarrow, 0\rangle, |0, \uparrow\downarrow\rangle$. In second order perturbation theory [81] in t the energy shift is given by

$$\Delta E = t^2 \sum_{|\psi\rangle,|\psi'\rangle} \frac{\left|\left\langle \psi' \right| \hat{c}^{\dagger}_{\mathrm{L},\uparrow}\hat{c}_{\mathrm{R},\uparrow} + \hat{c}^{\dagger}_{\mathrm{R},\uparrow}\hat{c}_{\mathrm{L},\uparrow} + \hat{c}^{\dagger}_{\mathrm{L},\downarrow}\hat{c}_{\mathrm{R},\downarrow} + \hat{c}^{\dagger}_{\mathrm{R},\downarrow}\hat{c}_{\mathrm{L},\downarrow} \left| \psi \right\rangle\right|^2}{\left\langle \psi \right| \hat{H}_{\mathrm{FH}}(t=0) \left| \psi \right\rangle - \left\langle \psi' \right| \hat{H}_{\mathrm{FH}}(t=0) \left| \psi' \right\rangle} = -\frac{2t^2}{U} \tag{1.141}$$

For two identical spins ($|\uparrow,\uparrow\rangle$ or $|\downarrow,\downarrow\rangle$) in the double well there is no shift due to the Pauli exclusion principle. Comparing this two the energies of the two-site Heisenberg model

$$\hat{H}^{(2)}_J = J\hat{\mathbf{S}}_{\mathrm{L}} \cdot \hat{\mathbf{S}}_{\mathrm{R}} \tag{1.142}$$

and ignoring the constant energy offset we obtain

$$J = 4\frac{t^2}{U}. \tag{1.143}$$

Chapter 2

Raman Cooling

In the early days of Bose-Einstein condensation it was attempted to laser-cool below the condensation temperature. Under typical conditions for ultracold dilute quantum gases the transition temperature is $T_{\mathrm{BEC}} \sim \mathcal{O}(100\,\mathrm{nK})$. Typical Doppler-cooling techniques are limited to the Doppler temperature (3.13) which for the alkali atoms is $T_{\mathrm{D}} = \frac{\hbar\gamma}{k_{\mathrm{B}}2} \sim \mathcal{O}(100\,\mu\mathrm{K})$. Sub-Doppler cooling techniques like polarization gradient cooling [114] in turn is only limited by the recoil energy of the cooling photons: $T_{\mathrm{r}} = \frac{\hbar^2 k^2}{2mk_{\mathrm{B}}} \sim \mathcal{O}(1\,\mu\mathrm{K})$ [115], still above the transition temperature. A promising candidate for sub-recoil cooling is the so called *motional sideband cooling*, where one explicitly drives transitions between resolved vibrational levels in a trap. Although pure laser-cooling to quantum degeneracy of alkali atoms[1] has not been achieved in neutral atoms, sideband cooling is the standard technique to cool trapped ions to their vibrational ground state [117].

2.1 Vibrational Transitions

For sideband cooling we need to treat the motion of a trapped atom quantum-mechanically. In the derivation of the driven two-level system (1.1.2.1) we neglected the motion of the atom by approximating $\exp\left(i\mathbf{k}\cdot\hat{\mathbf{r}}\right) \approx 1$. This assumption becomes invalid once the extent

[1] Recently Stellmar et al. [116] have laser-cooled the alkaline-earth atom ^{84}Sr to degeneracy via narrow-line Doppler cooling.

of the wavefunction is on the order of the optical wavelength. For simplicity let us assume that an atom is trapped in a harmonic trap (1.3) in the *resolved sideband regime*, where the trap frequency ω is larger than the natural linewidth of the optical transition $\gamma \ll \omega$ and the Rabi frequency $\Omega \ll \omega$. Its wavefunction then is a product of the electronic state $|i\rangle$ and motional state $|\nu\rangle$

$$|\psi\rangle = |i\rangle\,|\nu\rangle \equiv |i,\nu\rangle\,. \tag{2.1}$$

The frequency of the driving field is chosen such that it is resonant with the $|1,\nu\rangle$ to $|2,\nu'\rangle$ transition, i.e. $\omega_{\mathrm{L}} = \omega_{\mathrm{A}} + \omega(\nu' - \nu)$. Taking the vibrational states into account the transition matrix element is given by

$$\left\langle 2,\nu' \,\middle|\, \hat{d}\mathcal{E}^* \exp\left(-i\mathbf{k}\cdot\hat{\mathbf{r}}\right) \,\middle|\, 1,\nu \right\rangle = \hbar\Omega_0 \left\langle \nu' \,\middle|\, \exp\left(-i\mathbf{k}\cdot\hat{\mathbf{r}}\right) \,\middle|\, \nu \right\rangle = \hbar\Omega_0 \mu_{\nu',\nu}, \tag{2.2}$$

with the free space Rabi frequency Ω_0 (1.13).

For a single beam and an isotropic trap we can assume that $\mathbf{k}$ is along the x-direction. Using the ladder operator formalism (1.39) we can rewrite the motional part of the matrix element as

$$\mu_{\nu',\nu} = \left\langle \nu' \,\middle|\, \exp\left(-i\eta\left(\hat{a} + \hat{a}^\dagger\right)\right) \,\middle|\, v \right\rangle, \tag{2.3}$$

with the *Lamb-Dicke parameter*

$$\eta = \frac{1}{\sqrt{2}} k a_{\mathrm{QHO}} = \sqrt{\frac{E_{\mathrm{r}}}{\hbar\omega}}. \tag{2.4}$$

The definition of recoil energy $E_{\mathrm{r}} = \frac{\hbar^2 k^2}{2m}$ is identical to the recoil energy in an optical lattice (see 1.5.1.2 for example), *but* the wavelength is the resonant atomic wavelength (671 nm), not the lattice wavelength (1064 nm)! In our experiment with a trap frequency of about 1 MHz the Lamb-Dicke-parameter is on the order of $\eta \sim 0.27$.

The total Rabi frequency can be calculated analytically [118]

$$\Omega_{\nu',\nu} = \Omega_0 \exp\left(-\frac{\eta^2}{2}\right) (i\eta)^{|\nu'-\nu|} \sqrt{\frac{\nu_<!}{\nu_>!}} \mathrm{L}_{\nu_<}^{|\nu'-\nu|}(\eta^2), \tag{2.5}$$

where $\nu_<$ ($\nu_>$) is the level of the lower (higher) excited state and $\mathrm{L}_n^\alpha(x)$ are nth-order

generalized Laguerre polynomials [82]. But it is more instructive to only look at the leading order term for $\eta \ll 1$. For example the transition from $|\nu = 0\rangle$ to $|\nu' = 1\rangle$ has a matrix element $\mu^{(1)}_{1,0} = -i\eta$. The transition $|\nu\rangle$ to $|\nu' = \nu + 1\rangle$ has an enhanced amplitude due to the Bose enhancement of

$$\mu^{(1)}_{\nu+1,\nu} = -i\sqrt{\nu+1}\eta. \tag{2.6}$$

Transitions spanning two vibrational levels are based on a higher order process. Therefore the transition matrix element is reduced by another order in η

$$\mu^{(2)}_{\nu+2,\nu} = -\frac{1}{2}\sqrt{\frac{(\nu+2)!}{\nu!}}\eta^2.$$

Transitions to a lower vibrational level are called the *red sideband*, to a higher vibrational level the *blue sideband*. The transition frequency that does not change the vibrational state is called the *carrier*.

On the one hand being deeper in the Lamb-Dicke regime ($\eta \ll 1$) means that it gets harder to drive transitions between motional states, but on the other hand it is less likely to change the vibrational state during a spontaneous emission event! As pointed out by Kerman [119] this does not mean that recoil heating is suppressed. In free space the kinetic energy of an atom at rest increases by E_r, when it spontaneously emits a photon. If the spontaneous emission happens inside a tight trap the probability to change into an excited state is $\approx \eta^2$, but when it does its energy increases by $\hbar\omega = E_\mathrm{r}/\eta^2 > E_\mathrm{r}$, so that on average the energy increase again is E_r.

2.2 Raman Transitions

In typical experiments with neutral alkali atoms the linewidth γ ($\sim 2\pi \cdot 6\,\mathrm{MHz}$) is much larger than the trap frequency ω ($\sim 2\pi \cdot 1\,\mathrm{MHz}$). Hence it is not possible to directly resolve the motional sidebands with a single laser. By using a two-photon scheme the effective linewidth can be made (almost) arbitrarily narrow, so that the sidebands can be resolved nevertheless.

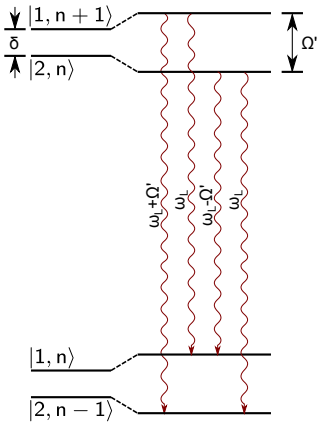

Figure 2.1: Spontaneous emission in the dressed-atom model

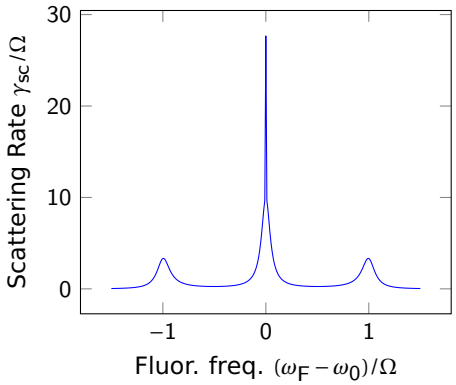

Figure 2.2: Resonance fluorescence spectrum of a strongly-driven two-level system ($\gamma = \Omega/10$, $\delta = 0$). The coherent peak is displayed with a device resolution of $\Delta\nu_{\text{measurement}} = \Omega/100$. atom

A three-level system in a Λ configuration is described by the Hamiltonian in the rotating-wave approximation [58] (see (1.12))

$$\hat{H} = -\hbar\delta_{13}\left|3\right\rangle\left\langle 3\right| - \hbar\delta_2\left|2\right\rangle\left\langle 2\right| - \frac{\hbar}{2}\left(\Omega_{13}\left|3\right\rangle\left\langle 1\right| + \Omega_{23}\left|3\right\rangle\left\langle 2\right| + \text{h.c.}\right), \tag{2.7}$$

where $\Omega_{13,23}$ denote the coupling between the groundstates $\left|1\right\rangle, \left|2\right\rangle$ and the excited state $\left|3\right\rangle$, δ_{i3} the detuning of the laser $\omega_{\text{L},i3}$ from the resonance $\omega_{\text{A},i3}$, and the two-photon detuning

$$\delta_2 = \delta_{23} - \delta_{13}. \tag{2.8}$$

In the limit where $\left|1\right\rangle$ and $\left|2\right\rangle$ are almost degenerate $\delta_{23} \approx \delta_{13} = \delta$ and the laser is far detuned from the excited state $\left|3\right\rangle$, the excited state can be adiabatically eliminated and the problem reduces to a two-level system with an effective *two-photon Rabi frequency*

$$\Omega_2 = \frac{\Omega_{23}^{*}\Omega_{13}}{4\delta}. \tag{2.9}$$

2.3 Optical Pumping: Coherent Vs. Incoherent Scattering

Using the dressed-atom picture [120] we can quickly gain some intuition about the spectrum of the light scattered by a single two-level atom. The dressed-atom model assumes a quantized driving electromagnetic field with the Hamiltonian

$$\hat{H}_{\mathrm{L}} = \hbar\omega_{\mathrm{L}}\left(\hat{n} + \frac{1}{2}\right). \tag{2.10}$$

The coupling of an atom to the light field with n photons mixes the ground and excited states $|1, n\rangle, |2, n'\rangle$ for photon numbers differing by 1. In the weak driving limit the states are given by

$$\begin{aligned} |+, n\rangle &\approx |2, n\rangle + \epsilon\,|1, n+1\rangle \\ |-, n\rangle &\approx |1, n+1\rangle - \epsilon\,|2, n\rangle\,, \end{aligned} \tag{2.11}$$

with the energies

$$E_{\pm,n} = \hbar\omega_{\mathrm{L}}(n + \frac{1}{2}) + \frac{\hbar\delta}{2} \pm \frac{\hbar\Omega'}{2}. \tag{2.12}$$

The dressed states are split by the generalized Rabi frequency (1.15) $\Omega' = \sqrt{\Omega^2 + \delta^2} = \delta + \frac{\Omega^2}{2\delta} + \mathcal{O}(\Omega^4)$ (see figure 2.1). Spontaneous emission couples the bare states $|2\rangle \to |1\rangle$. Hence there exist four transitions with three distinct frequencies ω_{L}, $\omega_{\mathrm{L}} - \Omega'$, and $\omega_{\mathrm{L}} + \Omega'$ for the decay between the n and $n-1$ manifold. The whole spectrum is composed of a *elastic* (*coherent*) δ-like peak at the laser frequency ω_{L} and *inelastic* (*incoherent*) peaks with widths on the order of the natural linewidth γ. In the limit of strong driving $\Omega' \gg \gamma$ the three incoherent peaks give rise to the *Mollow triplet* [121, 122] (also see figure 2.2).

The full fluorescence spectrum can be obtained solving the Master equation (see, for example, Scully and Zubairy [59]). The ratio of incoherently to coherently scattered total intensity is given by [121]

$$\frac{I_{\mathrm{incoherent}}}{I_{\mathrm{coherent}}} = 2\frac{\Omega^2}{\gamma^2 + (2\delta)^2}. \tag{2.13}$$

The inelastic/incoherent part is uniformly scattered into the whole 4π solid angle, whereas the elastic/coherent emission pattern depends on the incident polarization and the atomic

structure of the scattering atom [123].

For multiple atoms in an optical lattice the coherent nature of the *elastically* scattered light produces sharp interference features, *Bragg peaks*, which can be seen in the far-field or in the Fourier plane of an imaging system. Some groups use this as a technique to study the ordering in the lattice without single-site imaging [50, 112]. Bragg scattering has also been observed with a quantum gas microscope [124]. The angles under which the nth-order peak appear are given by [124]

$$\sin\theta_n = 1 + \frac{\lambda}{d_{\text{lat}}}, \tag{2.14}$$

where the periodicity of the lattice is given by d_{lat} and the atoms are coherently scattering light of the wavelength λ. Only one peak is captured by the imaging system of our experiment. Since the Bragg peak is narrow in Fourier space it contributes to a smooth background in the image plane.

Even for a single two-level atom (with only a single cycling transition) coherent scattering dominates for weak drive, but in a multi-level system coherent Raman-like transitions to non-degenerate ground state levels wash out the interference between multiple scattering for observation times longer than the inverse level spacing [123]. The transitions can be understood as a Raman transition, where the down leg is stimulated by a vacuum photon in a similar fashion as for normal elastic scattering.

2.4 Raman Sideband Cooling In A Bias Field

Commonly Raman cooling uses a magnetic field to break the degeneracy of the magnetic sublevels in the ground state [125, 126, 127, 128, 129]. In the case of degenerate sideband cooling the Zeeman magnetic field is tuned to bring $|\nu\rangle$ and $|\nu-1\rangle$ of different magnetic sublevels into resonance ($\mu B = \hbar\omega_{\text{trap}}$). Conceptually even easier is the case where one uses two phase-coherent laser beams that are detuned such that the Raman transition covers the Zeeman splitting and the vibrational splitting for the $|\nu\rangle \rightarrow |\nu-1\rangle$ transition. One needs to ensure that the Stark shift of the Raman lasers, i.e. the two-photon Rabi frequency, is

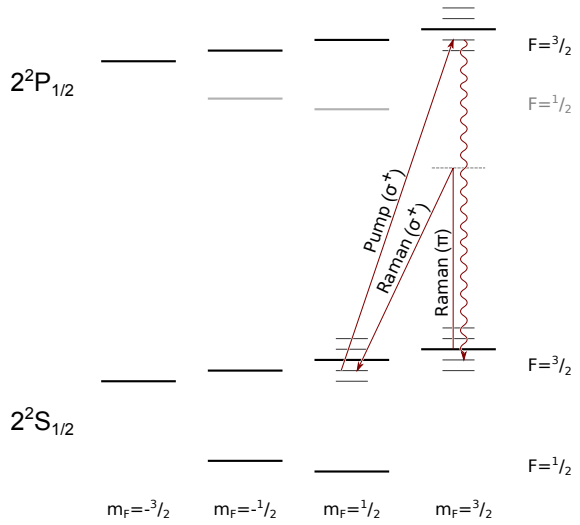

Figure 2.3: Raman sideband cooling scheme for $^6_3$Li using a bias magnetic field to Zeeman-shift the magnetic sublevels

smaller than the Zeeman splitting.

Our scheme for ^{6}Li is depicted in figure 2.3. Here the two Raman beams are 7 GHz red-detuned of the D_1 transition and couple the $|6,\nu\rangle = \left|2^2S_{1/2}(F=\frac{3}{2}, m_F=\frac{3}{2})\right\rangle |\nu\rangle$ to the $|5,\nu-1\rangle = \left|2^2S_{1/2}(F=\frac{3}{2}, m_F=\frac{1}{2})\right\rangle |\nu-1\rangle$ state. The optical pumping laser then brings the atoms back into the initial electronic state, while preserving the vibrational state $|5,\nu-1\rangle \rightarrow |6,\nu-1\rangle$. The probability of decay into a different vibrational state is suppressed by the Lamb-Dicke parameter η. The scattered photon plays an important role in our imaging process (see 2.9). With the given choice of polarizations the $|6\rangle$ state is dark for the pumping beam limited only by the purity of the polarization.

Because of the unfavorable branching ratios an additional repumping beam is necessary to bring the atoms back from the $\left|2^2S_{1/2}(F=\frac{1}{2})\right\rangle$ manifold into the $\left|2^2S_{1/2}(F=\frac{3}{2})\right\rangle$ manifold. This is achieved with a weak laser resonant with the $\left|2^2S_{1/2}(F=\frac{1}{2})\right\rangle$ to $\left|2^2P_{3/2}\right\rangle$ transition.

Although the $\left|2^2S_{1/2}(F=\frac{3}{2})\right\rangle$ manifold is not a closed two-level system, we were able to observe Rabi oscillations between the $|6\rangle$ and $|5\rangle$ state, but the revival is not perfect because of the coupling to the $|4\rangle$ and $|3\rangle$ states. From the timescale of the depletion of the $|6\rangle$ state we estimate our two-photon Rabi frequency to be $\Omega_2 \sim 20$ kHz on the carrier transition

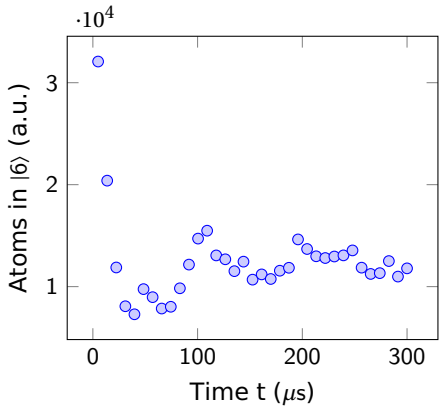

Figure 2.4: Rabi-like oscillations in the driven four-level system $|3 \ldots 6\rangle$

($\Delta\nu = 0$) for laser power of .

From a cooling perspective any of the $|4\rangle$, $|5\rangle$, $|6\rangle$ states is suitable for a Raman transition that takes out a vibrational quanta. So in principle even under imperfect optical pumping the cooling can still work, except that an atom needs to scatter multiple until it is pumped into the dark state. A Raman spectrum taken with a bias field of $B \sim 150\,\text{mG}$ can be seen in figure 2.5. Here the atoms were first optically pumped into the $|6\rangle$ state and the driven into the $|5\rangle$ state via the Raman transition.

2.5 Three-Dimensional Cooling

To cool all three motional degrees of freedom one needs to make all the trap frequencies degenerate or address all trap frequencies individually, one at a time. In our experiment the two-photon detuning is sequentially tuned onto the red sideband of the radial and axial lattices and then swept over the width of the resonance features to allow for spatial inhomogeneity in the trap frequencies (see figure 2.5).

In addition to tuning to the correct frequency, there needs to be momentum transfer along the direction one attempts to cool. This can be seen from the $\hat{\mathbf{x}} \cdot \mathbf{k}$ term in the vibrational coupling (2.2). If $\hat{\mathbf{x}}$ and $\mathbf{k}$ are not aligned, the Lamb-Dicke parameter (2.4) is reduced by $|\cos\theta|$, where θ is the angle between the two vectors. For a two-photon transition

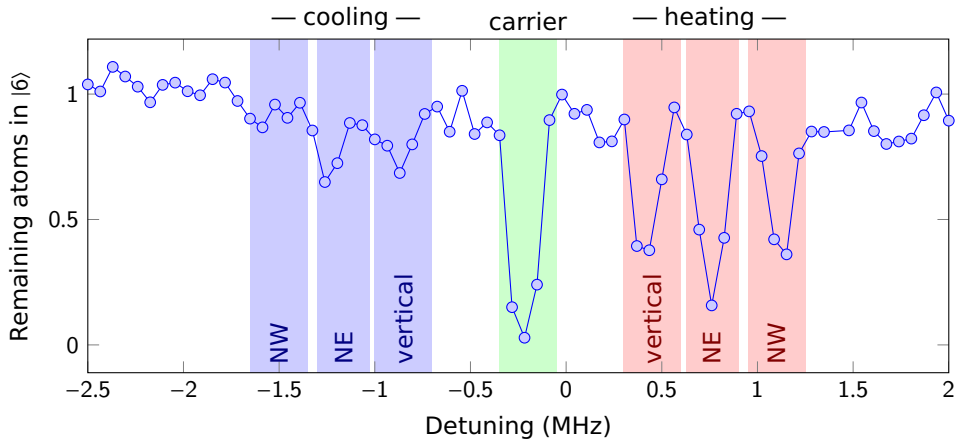

Figure 2.5: Raman spectrum taken by driving $|6\rangle \rightarrow |5\rangle$ at a bias field of 150 μG

the effective momentum kick $\mathbf{k}$ that the atom experiences from absorption ($\mathbf{k}_1$) followed by stimulated emission ($-\mathbf{k}_2$) is

$$\mathbf{k} = \mathbf{k}_1 - \mathbf{k}_2. \tag{2.15}$$

To maximize the coupling to all three lattice axes with a single pair of Raman beams one needs to choose $\mathbf{k}$ such that it spans a 45° angle with all the lattice axes. Due to space constraints in our experiment the angle between the direction of the momentum transfer and the vertical lattice (z) is only ∼75° so that the coupling is reduced by a factor of 25%. The coupling to the radial lattice axes is only reduced by $1/\sqrt{2}$.

2.6 Alignment

Since the $|6\rangle$ state is dark for the optical pumping, the polarization of the optical pumping can easily be optimized by maximizing the lifetime in the stretched state. The $|6\rangle$ state can be prepared with a microwave sweep driving the $|1\rangle \rightarrow |6\rangle$ transition. When completely optimized we can achieve a ratio of the lifetimes for the two circular polarizations of

$$\frac{\tau_{\sigma+}}{\tau_{\sigma-}} \sim 10 \ldots 100. \tag{2.16}$$

All polarization assume a certain quantization axis set by the magnetic bias field. The

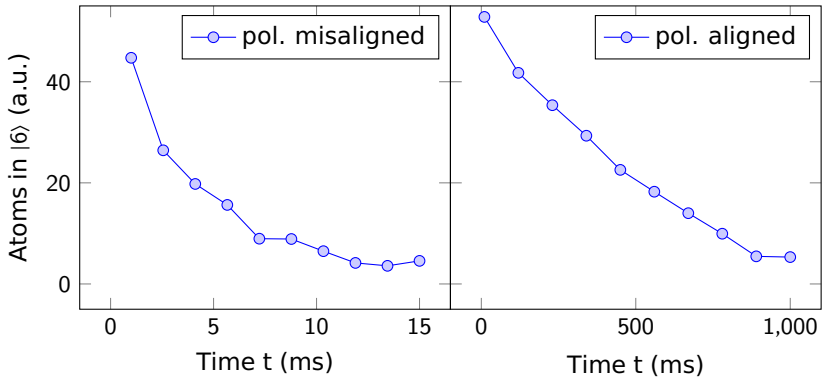

Figure 2.6: Decay out of $|6\rangle$ while exposed to optical pumping light with and without optimized polarization

direction of the magnetic field has to be optimized as well, so that it points along the σ^+-Raman and optical pumping beam. The wrong circular polarization can in principle drive a wrong sideband (i.e. a blue sideband), but that transition is detuned by the Zeeman shift and thus suppressed.

The polarization of the linearly polarized π-Raman beam is set to minimize the reflection off the glass cell. This procedure is roughly equivalent to setting the polarization to be vertical (along z). The polarization of the σ^+-Raman beam is optimized by transferring population out of the $|6\rangle$ state via the carrier Raman transition.

The pointing for all the Raman and optical pumping beams is optimized by heating trapped atoms out of the lattice with one beam at a time. For the fine alignment the beams need to be attenuated further with neutral density filters.

2.7 Raman Sideband Cooling At Zero Field

The problem of the finite "darkness" of the $|6\rangle$ state due to imperfect polarizations can be avoided by altering the cooling scheme and working at negligible bias field ($\mu_B B \ll \hbar\Omega_2 \ll \omega_{trap}$). Without the Zeeman field all the magnetic sublevels are degenerate and we can drive Raman transitions between the $\left|2^2S_{1/2}(F=\frac{3}{2})\right\rangle$ and $\left|2^2S_{1/2}(F=\frac{1}{2})\right\rangle$ manifold while tuning to the red sideband. An optical pumping beam pumps the atoms back into the

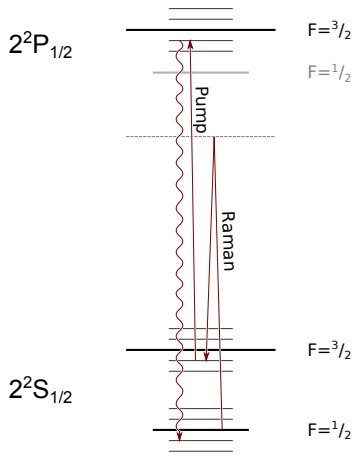

Figure 2.7: Raman sideband cooling scheme for $^6_3$Li without a bias field

$\left|2^2S_{1/2}(F=\frac{3}{2})\right\rangle$ manifold. The upper manifold is 228 MHz detuned from the pumping light so that the scattering rate (1.30) is suppressed by $\approx \Omega^2/\delta^2 \sim \mathcal{O}(10^{-4})$ (for a $s_0 = 0.1$). The Raman spectrum acquired in the $B = 0$ configuration is given in figure 2.8. Without the bias field the carrier is exactly at zero detuning. Within the noise there are no transitions on the cooling sidebands. This is a strong indication that the atoms are in the lowest band of our optical lattice.

2.8 Heating Mechanisms

During the cooling atoms in the optical lattice are subject to several heating mechanisms. The most severe one is the loss of pairs of atoms due to *light-assisted collisions* [130][2]. The potential curves for scattering of a $\left|2^2S_{1/2}\right\rangle$ ground state atom with an excited state $\left|2^2P_{1/2}\right\rangle$ are altered by the long range dipole interaction. In case of red-detuned (blue-detuned) light the atoms experience a long range attractive (repulsive) interaction $\propto 1/r^3$. Atoms can either end in a bound-state (photoassociation) with the photon carrying away the excess energy or the excess energy is released as kinetic energy after the excited state decays back to the ground state. Due to the repulsive nature of the interaction for blue-detuned light inelastic

[2]In the context of magneto-optical traps light-assisted collisions are also called radiative escape [131]

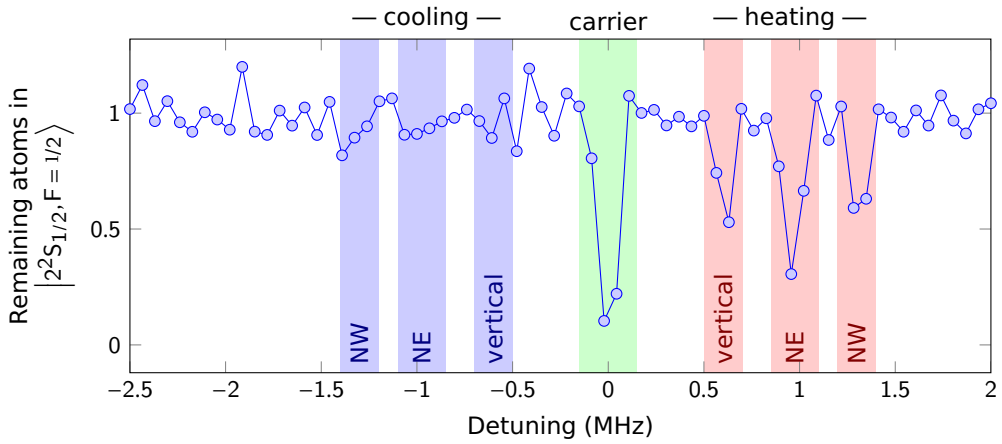

Figure 2.8: Raman spectrum taken by driving atoms into the $|2^2S, F = 3/2\rangle$ manifold with a single sweep over $\pm 50\,\text{kHz}$ in $500\,\mu\text{s}$

processes are suppressed [130].

Additionally mixtures of different magnetic sublevels of the two groundstate manifolds $|2^2S_{1/2}(F = \frac{3}{2})\rangle$ and $|2^2S_{1/2}(F = \frac{1}{2})\rangle$ can release energy on the order of the hyperfine splitting via *spin-changing collisions*. This effect together with the light-assisted collisions makes it impossible to have two atoms tightly confined to a single lattice site while scattering resonant photons, which will most likely result in *parity imaging*, where one can only detect the atom number per site modulo two [35]

For a single atom on a lattice site the following other heating mechanisms remain. Single photon scattering imparts the photon momentum onto the atom it scatters of. In the case of an atom at rest its energy increases by up to $2E_\text{r}$ and $1E_\text{r}$ on average for incoherent scattering. This *recoil heating* can occur both for optical pumping and the Raman beams. Because of the small fine structure of ^{6}Li of only 10 GHz the optimum detuning of the Raman beam coupling different magnetic sublevels is on that order [132]. In this regime the ratio of single photon scattering rate to two-photon Rabi frequency is on the order of $1/100$.

In addition, atoms in an excited state experience a different trapping potential due to its different polarizability. For cooling of ^{6}Li on the $2s$ to $2p$ transitions in a trap at 1064 nm luckily this effect is rather small. The polarizability of the ground state $|2^2S_{1/2}\rangle$ is $\alpha_{2s} = 271\,\text{au}$, for $|2^2P_{1/2}\rangle$ $\alpha_{2p,\text{D1}} = 202\,\text{au}$, for $|2^2P_{3/2}(m_F = |\frac{1}{2}|)\rangle$ $\alpha_{2p,\text{D2},1/2} = 221\,\text{au}$, and

for $\left|2^2P_{3/2}(m_F = \left|\frac{3}{2}\right|)\right\rangle$ $\alpha_{2p,\mathrm{D2},3/2} = 183\,\mathrm{au}$, where the atomic polarizability unit is defined as $\mathrm{au} = 4\pi\epsilon_0 a_0^3$ [60].

A classical estimation for the *fluctuating dipole force heating/stochastic heating* is given in [100]. Taking the finite excited state decay rate γ into account the fractional energy increase per excitation is given by

$$\epsilon = \frac{E_3 - E_1}{E_1} = \frac{\left(\omega_1^2 - \omega_2^2\right)^2}{\omega_1^2\left(\gamma^2 + 4\omega_2^2\right)}. \tag{2.17}$$

For ^{6}Li atoms in a 1064 nm lattice with a ground state trap frequency of $\omega_1 = 2\pi \cdot 1\,\mathrm{MHz}$ subject to D_1 cooling light this results in a fractional energy increase of $\epsilon = 0.0018$ per excitation. Assuming that the initial energy E_1 is on the order of $\hbar\omega_1 \approx 13.5 E_\mathrm{r}^{(671\,\mathrm{nm})}$ the energy gain is only 0.024 times the resonant photon recoil energy of $E_\mathrm{r}^{(671\,\mathrm{nm})} = h \cdot 73.9\,\mathrm{kHz}$. Besides choosing a (near-)magic wavelength for the optical trap, this kind of heating can also be minimized by keeping the saturation parameter low, so that there is negligible population in the excited state. While this kind of heating has little effect for cooling on the $D_{1,2}$ transitions, it could be a problem, for example, if one would want to directly resolve the vibrational sidebands by using the narrow ultraviolet $2s$ to $3p$ transition. Although there is a magic wavelength near 1070 nm, the $3p$ state decays predominantly via the $3s$ state as intermediate state which has large polarizability with opposite sign [100].

As for all optical traps technical noise, like residual amplitude modulation, can cause *parametric heating* as well (see 1.4.4). This becomes especially problematic during the imaging when the lattice depth is maximal with high trap frequencies, since heating rates scale super-linearly with the trap frequency (ω^α, $\alpha \geq 2$).

2.9 Raman Imaging

We would like to use the scattered photons of the optical pumping process for fluorescence imaging. Because of the second order nature of the Raman process, we are going to need significantly higher laser powers for the Raman transitions than for the optical pumping.

For a 100 µs long Raman pulse with 1 mW and a hypothetical uniform intensity over

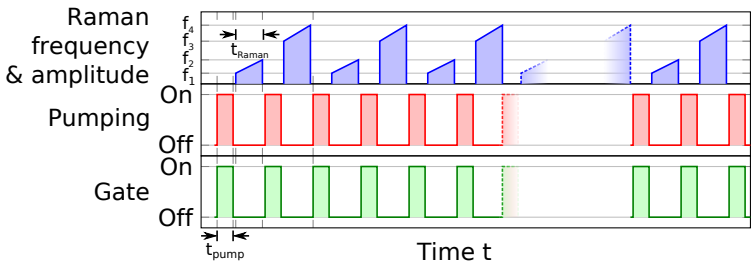

Figure 2.9: Gated imaging during the Raman cooling

100×100 lattice sites the atoms are illuminated with 3×10^{11} photons at 671 nm in total. If we assume we only see Rayleigh scatter on the order of 10 ppm off the superpolished substrate, 3×10^6 photons get scattered in total and 300 photons per lattice site. During the optical pumping pulse each atom only scatters $\mathcal{O}(1)$ photons before it gets optically pumped into a dark-state. This scenario would result in a signal-to-noise ratio of $\sim 1 : 100$, which is far from being enough to resolve individual atoms (for a rather low overall count rate).

2.9.1 Pulsed Raman Imaging

Due to the small fine-structure splitting of only 10 GHz it is virtually impossible to spectroscopically filter the cooling light from the imaging light with, for example, a dichroic mirror. Instead of trying to separate the light spectroscopically, we are separating the Raman from the pumping light temporally by performing up to 6000 two-step cooling processes and only exposing the camera during the optical pump pulse.

For the initial tests with the low-resolution imaging we used a mechanical chopper (Thorlabs MC2000 with MC1F30 blade) in the intermediate imaging plane (see figure 3.18) to block the camera during the Raman pulses. The rotation of the chopper is phase-locked to the experiment with the blades opening and closing at 2 kHz.

Because of the finite aperture of the chopper blades, it is not possible to use this setup in the high resolution imaging described in section 3.3.1.5. It might be possible to create an intermediate demagnified image with another long working distance microscope objective,

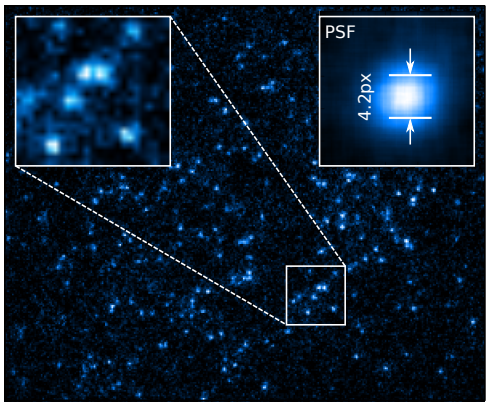

Figure 2.10: Resolving individual atoms in at sparsely filled optical lattice

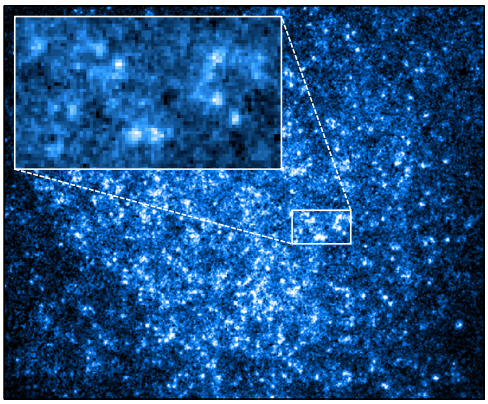

Figure 2.11: Fluorescence image of a dense thermal cloud in an optical lattice

but we had concerns that turbulent airflow caused by the edges of the fast spinning blade would distort the images.

The way around this limitation is to shutter the camera by other means, in our case by the use of a gated camera. In our experiment we are using an ANDOR iStar 334T intensified CCD camera. The intensifier, a HAMAMATSU V8070x, consists of a light-sensitive photo-cathode that produces electrons that in turn get amplified with a micro-channel plate. Electrons leaving the micro-channel plate produce fluorescence on a phosphor screen that is imaged by the CCD chip of the camera. By turning the photo cathode voltage (and optionally the micro-channel plate voltage) on and off we can gate the camera during the acquisition with pulse widths down to 2 ns. Due to the moderate quantum efficiency of the photo-cathode in the red, the overall quantum efficiency drops by about a factor of two to ∼45% compared to the ANDOR iXon 888, the EMCCD camera we were previously using.

We have sucessfully demonstrated the first imaging of ultracold fermions in an optical lattice using our Raman cooling and gated imaging technique. From images of a sparsely filled lattice (figure 2.10) we extracted at averaged point spread function with a FWHM of ∼4.2 px. The lattice spacing itself is about 5 px and therefore we are clearly in the site-resolved regime. Images of a more densely populated optical lattice (figure 2.11) reveal a large uniform background. This is most likely caused by some atoms that are not cooled

enough and tunnel during the imaging process. An additional effect could be the Bragg scattering for denser clouds (see 2.3) that is expected to produce a smooth background as well. But these shortcomings are being addressed right now, while this work is being written.

2.9.2 Fidelity: Imaging A 3×3 Plaquette Or Single Atom Minesweeper

In this section I want to demonstrate the effect of overlapping point spread functions when imaging single atoms in an optical lattice. As a model I am going to use a 3×3 plaquette with variable filling factor and focus on the central lattice site. The particles are non-interacting with a maximum occupation of one per site. This would be valid model for a spin polarized Fermi gas in the ground band of an optical lattice or one spin state of a non-interacting multi-component Fermi gas. Effects like electronic noise or photon counting statistics will be ignored here. It is assumed that the fluorescence image gets analyzed by integrating up the fluorescence of each lattice site.

The nine lattice sites are labeled with the following indices

$$\begin{array}{|c|c|c|} \hline 8 & 1 & 5 \\ \hline 4 & 0 & 2 \\ \hline 7 & 3 & 6 \\ \hline \end{array} \,. \tag{2.18}$$

Using those indices we can write all $2^9 = 512$ possible states encoded as a binary number, for example

$|000000000_2\rangle =$  , $|000000001_2\rangle =$  , $|000000010_2\rangle =$  ,

$|101010011_2\rangle =$  $|111111110_2\rangle =$  $|111111111_2\rangle =$  .

The sites can be grouped into three categories: the center site 0, the nearest neighbors $1, 2, 3, 4$, and the next-nearest neighbors $5, 6, 7, 8$. Atoms in each category are going to have a different contribution of their point spread function to the total intensity in the square of

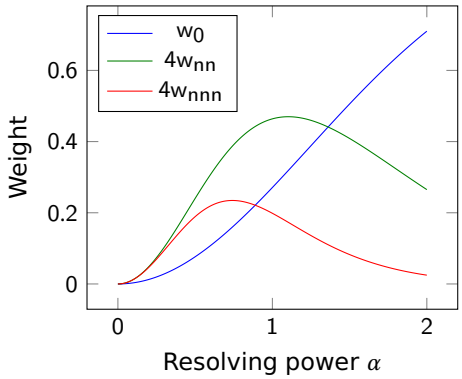

Figure 2.12: Contribution to the fluorescence on the center site from nearest neighbors and next-nearest neighbors

site 0. For simplicity the point spread function is approximated as a Gaussian of the form

$$\mathrm{psf}(x,y) = \frac{1}{\pi s^2}\exp\left(-\frac{x^2+y^2}{s^2}\right). \tag{2.19}$$

With that we can get analytic expressions for the "leakage" of the point spread function onto the center site from the nearest and next-nearest neighbors w_{nn}, w_{nnn} (see figure 2.12):

$$\begin{aligned} w_0 &= \int_{-\alpha s/2}^{\alpha s/2}\mathrm{d}x\int_{-\alpha s/2}^{\alpha s/2}\mathrm{d}y\,\mathrm{psf}(x,y) = \mathrm{erf}^2\left(\frac{1}{2}\alpha\right) \\ w_{\mathrm{nn}} &= \int_{\alpha s/2}^{3\alpha s/2}\mathrm{d}x\int_{-\alpha s/2}^{\alpha s/2}\mathrm{d}y\,\mathrm{psf}(x,y) = \frac{1}{2}\mathrm{erf}\left(\frac{1}{2}\alpha\right)\left(\mathrm{erf}\left(\frac{3}{2}\alpha\right)-\mathrm{erf}\left(\frac{1}{2}\alpha\right)\right) \\ w_{\mathrm{nnn}} &= \int_{\alpha s/2}^{3\alpha s/2}\mathrm{d}x\int_{\alpha s/2}^{3\alpha s/2}\mathrm{d}y\,\mathrm{psf}(x,y) = \frac{1}{4}\left(\mathrm{erf}\left(\frac{3}{2}\alpha\right)-\mathrm{erf}\left(\frac{1}{2}\alpha\right)\right)^2. \end{aligned} \tag{2.20}$$

Here the lattice spacing is assumed to be αs. The total probability to collect fluorescence from the center site for any state can be written as

$$w(n_0, n_{\mathrm{nn}} n_{\mathrm{nnn}}) = n_0 w_0 + n_{\mathrm{nn}} w_{\mathrm{nn}} + n_{\mathrm{nnn}} w_{\mathrm{nnn}},$$

with $n_0 \in \{0,1\}$ atoms on the center site, $n_{\mathrm{nn}} \in \{0,1,\ldots,4\}$ on the nearest neighbor sites, and $n_{\mathrm{nnn}} \in \{0,1,\ldots,4\}$ on the next-nearest neighbor sites. In total there are $2\cdot 5\cdot 5 = 50$ different values for fluorescence level w, but some of these stem from different states/configurations. For example  ,  ,  , , ,and will have identical fluorescence. In general each w is $\binom{2}{n_0}\binom{4}{n_{\mathrm{nn}}}\binom{4}{n_{\mathrm{nnn}}}$ fold degenerate.

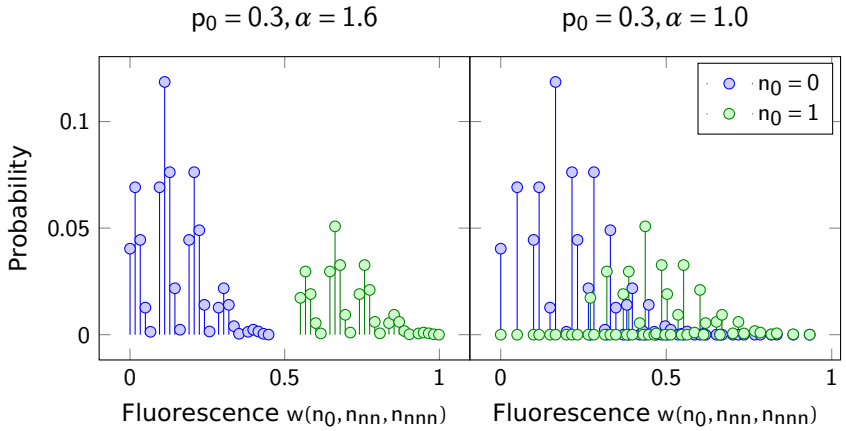

Figure 2.13: Total fluorescence in the central lattice site for different optical resolutions

The probability to find an atom on a given site is denoted by p_0. If the 3×3 plaquette is considered to be part of a larger system, p_0 can also be interpreted as the filling factor. The probability to find the plaquette in a given state/configuration with $n = n_0 + n_{\mathrm{nn}} + n_{\mathrm{nnn}}$ atoms is given by

$$p_n = p_0^n (1 - p_0)^{9-n}. \tag{2.21}$$

Combining all this we find that the probability to get $w(n, n_{\mathrm{nn}}, n_{\mathrm{nnn}})$ is

$$p\left(w(n_0, n_{\mathrm{nn}}, n_{\mathrm{nnn}})\right) = \binom{2}{n_0}\binom{4}{n_{\mathrm{nn}}}\binom{4}{n_{\mathrm{nnn}}} p_0^{n_0+n_{\mathrm{nn}}+n_{\mathrm{nnn}}} (1 - p_0)^{9-n_0-n_{\mathrm{nn}}-n_{\mathrm{nnn}}}. \tag{2.22}$$

The distribution is visualized for a sparse lattice in figure 2.13.

The fidelity of the imaging (with this particular way of analyzing the images) depends on whether we can distinguish configurations with a hole in center from the ones with an atom. For realistic parameters the worst case is trying to separate and . The two fluorescence levels $w(0,4,4)$ and $w(1,0,0)$ can be resolved for

$$\alpha > \alpha_0 \approx 1.48. \tag{2.23}$$

Around this point the "fidelity" defined as $F = \frac{1}{2}(w(1,0,0) - w(0,4,4) + 1)$ scales linearly with the resolving power α

$$F(\alpha) = \frac{1}{2}(w(1,0,0) - w(0,4,4) + 1) \approx 0.500 + 0.447(\alpha - \alpha_0) - 0.025(\alpha - \alpha_0)^2 + \mathcal{O}((\alpha - \alpha_0)^3).$$

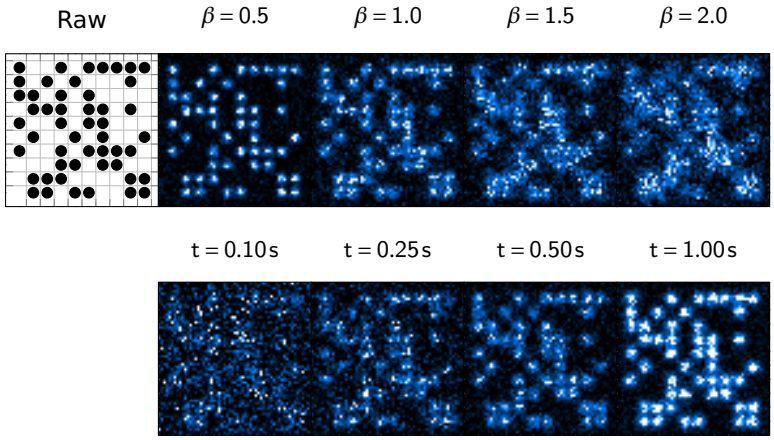

Figure 2.14: Simulation of fluorescence imaging for a scattering rate of 3 kHz

This limit can be circumvented by using more an advanced analysis algorithm that takes the surrounding lattice sites into account instead of looking at each site individually and I would like to emphasize that the model described in this section does not take the actual photon detection including counting uncertainty and noise into account.

2.9.3 Monte-Carlo Imaging Simulation

To get a feel for how fluorescence images are going to look as a function the imaging parameters, like resolution, exposure time, noise, etc. it is helpful to simulate the imaging process. I have done this as a Monte-Carlo simulation, where for every small time interval Δt the following probabilities are calculated for each site: probability that the atom is lost (loss rate), has scattered a photon (scattering rate), and the scattered photon is detected (numerical aperture, quantum efficiency of sensor, transmission of optical setup). Each detected photon is added to the sensor with a Gaussian probability distribution centered on the originating lattice site. This is emulating the point spread function of the imaging setup. In addition, dark-counts get added to the sensor each time step. At the end of the simulation readout noise is added to the sensor following a normal distribution.

With this (admittedly brute-force) Monte-Carlo approach one can already study the effect of dark-counts, scattering rate, and resolution to determine parameters that would

allow imaging with sufficient fidelity. Figure 2.14 shows simulated images for a filling factor of $p_0 = 0.5$ and varying spot sizes β (with $t = 0.5\,\mathrm{s}$) and exposure times t (with $\beta = 1$). The standard deviation of the point spread function is $\beta/2$ times the lattice spacing.

Chapter 3

Experimental Setup

3.1 Vacuum System

Besides the atomic beam source and pumping sections the experiment consists of two connected vacuum chambers, the main chamber and the science chamber (3.1). This two-chamber design has the advantage that there is not direct line-of-sight to the hot source, which could potentially reduce the trap lifetime. In addition, the secondary chamber can be swapped out relatively easy to accommodate different very specialized setups.

In the former, slow atoms from the Zeeman slower (see section 3.4.2) get captured and cooled in a magneto-optical trap (see section 3.4.3). With the aid of a high power optical dipole trap (3.3.7) and magnetic field coils [100] that allow to increase the interparticle scattering cross section by the use of a Feshbach resonance (1.2), the atoms can be cooled further, even to a point where the lithium atoms condense into a molecular Bose-Einstein condensate (3.36). This is an ideal starting point to perform cutting edge experiments with the ultracold atoms.

Because a quantum gas microscope (3.3.1) requires a large amount of optical access, the science chamber is a fused silica glass cuvette (3.1.2). Additionally using glass avoids eddy currents caused by switching magnetic fields and changing magnetic fields due to magnetizable materials.

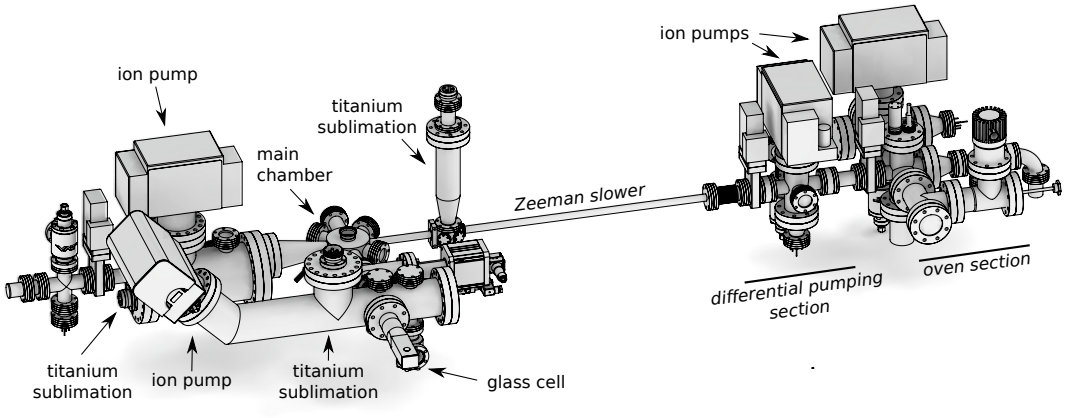

Figure 3.1: Overview of the vacuum chamber

To achieve a low background pressure in the science chamber, it is pumped by the combination of a GammaVacuum TiTan DIX 75S diode-style ion pump and a GammaVacuum titanium sublimation pump connected via an intermediate pumping chamber. A large gas load in a glass cell comes from helium diffusion through the glass. A differential diode-style ion pump is more efficient at pumping noble gasses (He, Ar, ...) than the typical diode pumps while sacrificing a little in overall pumping speed [133].

In addition to the ion pump, the titanium sublimation pump is helps pumping the remaining reactive gasses (CO, CO_2, O_2, etc.) in the system and to some extent even hydrogen H_2 [133]. After degassing during the bake out, each of its filaments has been fired multiple times for 1 min at a current of 48 A to sputter titanium onto the walls of the pump chamber. To avoid shorting the ion pump cells the pump chamber has a smooth 45° before it attaches to the pump. In this configuration there is no direct line-of-sight between the ion pump and the titanium filaments.

We found that ion gauges significantly contribute to the gas load. Therefore the pressure is only measured at a single point of the experiment, reading $3 \cdot 10^{-12}$ torr. This number is consistent with the lifetimes measured in the main chamber.

During the bake-out we had a residual gas analyzer (RGA) attached to the chamber (on the UHV side of the pump). The idea was to more accurately measure the pressure once the chamber has been sealed of from the turbo pump, but it turned out that, although the

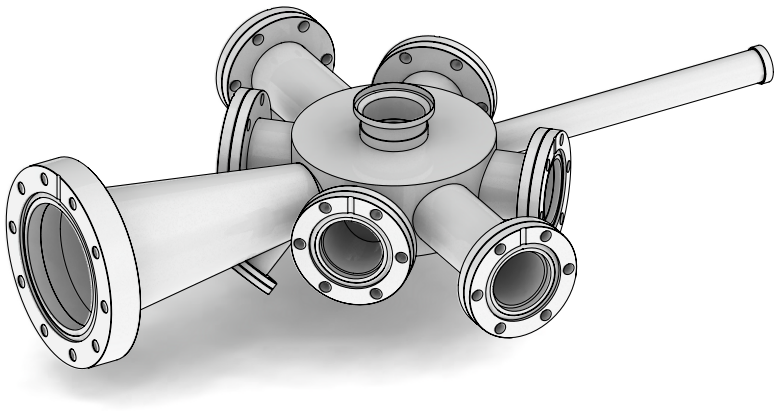

Figure 3.2: Drawing of the main chamber

RGA had been baked as well, turning it on released so much gas that the chamber had to be rebaked (probably electron desorption). For future bake-outs I would recommend to only use the RGA either continuously during bake-out or, even better, only on the rough vacuum side.

3.1.1 Main Chamber

The main chamber (figure 3.2) is a custom octagonal vacuum chamber made from 316-series stainless steel manufactured by Sharon Vacuum. It has ports for the magneto-optical trapping beams, the high-power optical dipole trap, and two electric feed-throughs for microwave antennae. For a more detailed description see my diploma thesis [134].

3.1.2 Glass Cell

The rectangular cuvette (figure 3.3) of the dimensions 45 mm × 35 mm × 110 mm with 5 mm walls was manufactured by Japan Cell and distributed by Triad Technology Inc.[1] The cell is made from UV grade fused silica and optically contacted, then heated to strengthen the bond. Despite the higher helium permeability of fused silica (about one order of magnitude

[1]The whole glass cell ordering process took more than a year from a first quote to the finished glass cell. I would like to warn everyone about this, who is considering using a glass cell as a vacuum chamber.

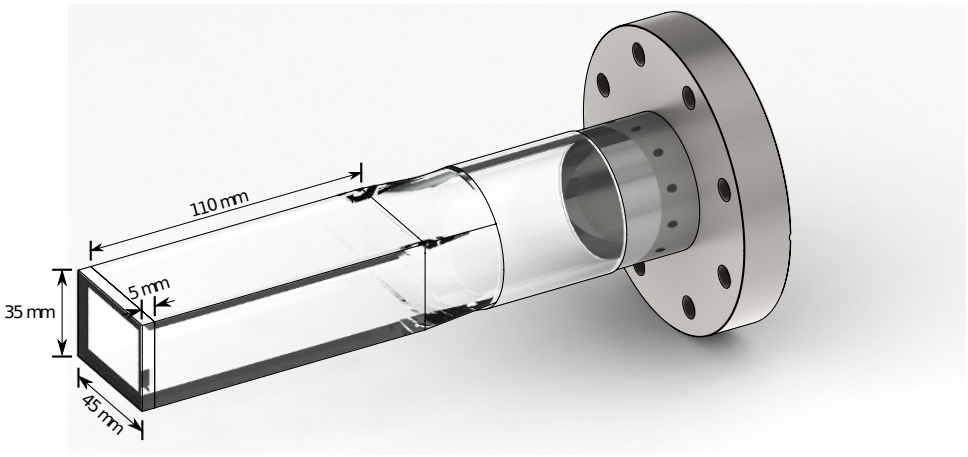

Figure 3.3: Drawing of the glass cell including the Conflat flange

worse than the best glasses) [135] this material was chosen because it is superior to e.g. borosilicates for applications requiring high laser intensities.

The glass cell does not have an anti-reflection coating on either side. The high power lattice beams (3.3.3) are entering the glass cell near Brewster's angle, so that the reflectivity is low even for uncoated glass [86].

There are small bubbles visible at the interface between the faces of cell, probably trapped water from the contacting process. Since none of them extend all the way to the vacuum side, they should not cause virtual leaks. The flatness at this stage was interferometrically measured to be on the order of $\lambda/6$ over 25 mm. Besides visual inspection all glass cells have been leak checked on a custom-machined flange with a silicone rubber seal to accommodate the rectangular open end of the cuvette. The cells were then sent to Precision Glassblowing to be fused onto a non-magnetic Bomco B1508S glass-to-molybdenum adapter with a rotateable 316 stainless steel $4^1/_2$ in Conflat flange. After fusing the whole cells were heated once more to relief the strain in the glass.

The multiple heating cycles then caused the surface flatness to slightly degrade. In addition, glass dust ($\approx$ 10 um and bigger) from repolishing the open end of the glass cell got baked onto the inside of the glass cell and was difficult to remove (see section 3.3.1.2).

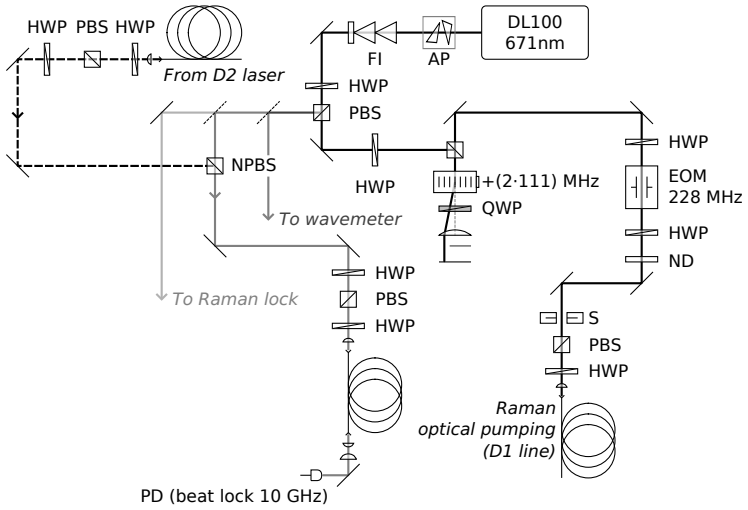

Figure 3.4: Optical setup of the D1 laser

3.2 Lasers

3.2.1 D2 Lasers

Our laser system consisting of home-built grating stabilized external cavity diode lasers and tapered amplifiers to create light that is resonant with the D_2 transition of $^6_3$Li is described in detail in Tobias Schuster's diploma thesis [136]. Although the setup has been modified over the years its basic principle remained identical.

Currently we are working on replacing the reference cell and the Doppler-free saturation spectroscopy with a new cell and modulation transfer spectroscopy [137] that should allow offset free locking.

3.2.2 D1 Laser And Raman Laser

The Raman cooling scheme (2) that we apply during the fluorescence imaging requires light resonant with the D_1 transition for optical pumping and light a few GHz red-detuned to drive Raman transitions.

To achieve a stable laser frequency the D_1 laser (figure 3.4) is locked to the D_2 laser via a frequency beat lock [100] at 10.007 GHz. This differs from the fine-structure splitting

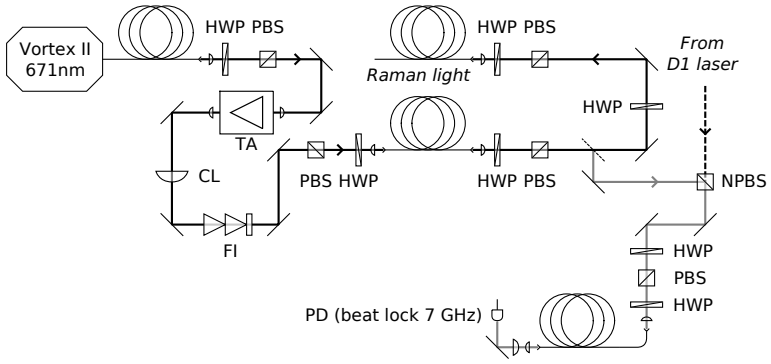

Figure 3.5: Optical setup of the Raman laser

because both the D_1 and D_2 lasers get frequency shifted using acousto-optical modulators before they reach the atoms. The Raman laser is then locked to the D_1 laser via another beat-lock at 7 GHz.

The beat signal in both cases is detected on a fiber coupled Hamamatsu G4176-03 photodetectors that are biased by a MiniCircuits ZX85-12G+ bias tee. The signal is then amplified twice with MiniCircuits ZX60-24-S+ amplifiers before the frequency gets stepped down with a RF Bay, Inc. FPS-6-12 pre-scaler, to bring the frequency into the range of our frequency detection circuit (below 3 GHz).

3.2.3 High Power ODT

In the experiment sequence (see 3.4.3) atoms from the magneto-optical trap get directly transferred into an optical dipole trap to perform evaporative cooling. At this stage the atoms are still relatively hot (about 1 mK) and therefore high laser powers are required to trap them in a conservative potential of a far off-resonant trap.

Although alternative solutions exist (e.g. cavity-enhanced trapping [138]), in our experiment the deep trapping potential is created by brute-force approach: a 300 W water-cooled 1070 nm frequency multimode, spatial single mode IPG Photonics YLR-300-LP-WC fiber laser focused to a Gaussian waist of 54 µm. The coherence length of this laser is measured to be 270 µm [100]. At full power this should yield a trap depth of about 4 mK – sufficiently deep to capture atoms directly from a compressed magneto-optical trap.

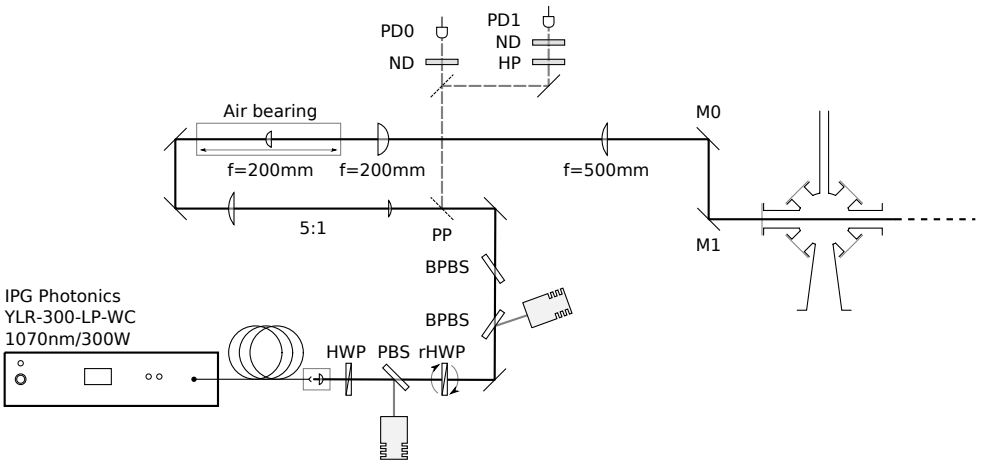

Figure 3.6: Optical setup of the high power optical dipole trap

At such high power levels transmission optics can exhibit *thermal lensing*. The main contributions are the temperature-dependent index of refraction $\mathrm{d}N/\mathrm{d}T$ and the coefficient of thermal expansion, which cause a locally varying index of refraction inside an optical element [139]. We did a more careful study in the context of our lattice lasers (section 3.2.5), for the optical dipole trap we avoided complications by not using an acousto-optical modulator and instead control the laser power using different means.

3.2.3.1 Power Stabilization

The laser itself can be directly modulated between full power and about 30 W at a bandwidth of a few 10s of kilohertz by controlling the current of its pump diodes. To get a higher dynamic range, we combined the current modulation with a stepper-motor driven variable attenuator consisting of a rotating half-wave plate and two Brewster plates. In addition, two separate photodiodes (PD0, PD1 in figures 3.6 and 3.7) with different levels of attenuation are used to cover power levels between a few mW and 300 W. Stabilizing the optical power in such a complex system can be challenging and is done best with a digital loop filter, in our case implemented using our FPGA-based experiment control system [100]. The power is always actively stabilized using the pump current, but the attenuation is varied by doing feed-forward-like control of the rotating waveplate (rHWP). The transmission η of the

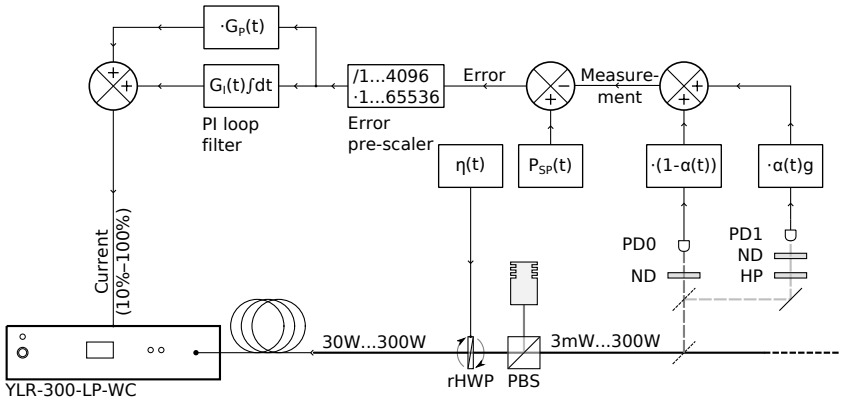

Figure 3.7: Simplified diagram of the feedback setup to stabilize the output power over a large dynamic range

waveplate polarizer setup as a function of the stepper motor position s and the number of steps per full period is given by

$$\eta(s) = (1 - \eta_0) \cos^2\left(\pi \frac{s}{s_0}\right) + \eta_0 \tag{3.1}$$

with a maximum extinction $\eta_0 \sim 1/1000$. At this high power levels polarizing beam splitter cubes should be avoided and Brewster polarizers should be used instead.

The small glitches from the finite resolution of the stepper motor and the motor bounce back are almost completely smoothed out by the active feedback. But when the attenuation is increased, the loop gain on the other hand effectively decreases. This can become a problem once the loop gain is too low to filter out the glitches. For example, when the setpoint is set to 50 W, but the current measurement is 60 W, the error is just 10 W, if there is no attenuation at all. If, however, the transmission is set to $1/2$ and the measured power after the attenuation again is 60 W, the laser is actually outputting twice that, namely 120 W. Although the measured error is still only 10 W, the laser pump current is an equivalent of 20 W too high. Hence the proportional and integral gain $G_{\mathrm{P,I}}$ should always be inversely proportional to the attenuator transmission η

$$G_{\mathrm{P,I}} = \frac{G^{(0)}_{\mathrm{P,I}}}{\eta}. \tag{3.2}$$

Since the gain needs to be adjusted over three orders of magnitude or 10 bits, the error

is first multiplied by an factor of 2^p ($p = -12 \ldots 16$) to preserve enough significant bits without running into truncation errors.

3.2.3.2 Closed Loop Ramp

During the first part of the optical evaporation (3.4.4) the laser power is ramped down to 30 W. This is done by reducing the pump current until the power setpoint is at 50 W and then the attenuator transmission is adjusted such that for any given setpoint P_{set} the actual laser output power P_{laser} stays around $P_0 = 50\,\text{W}$:

$$\eta(t) = \frac{P_{\text{set}}(t)}{P_0} \tag{3.3}$$

The stepper motor position is then calculated from the setpoint P_{set} by inverting equation (3.1) while assuming perfect extinction $\eta_0 \to 0$. From this point on the evaporation is done by feeding forward on the attenuator, the loop filter only needs to make small adjustments to the pump current.

When the laser power is ramped down further and reaches about 8 W, a hand-over between the high and the low power photodiode is performed. The measurement input V_{meas} of the loop filter can blend between the low power photodiode V_{low} to the high power photodiode V_{high}

$$V_{\text{meas}} = (1 - \alpha(t))V_{\text{high}} + \alpha(t)gV_{\text{low}}, \tag{3.4}$$

where g is the ratio of the laser power to voltage gains of the high and low power photodiodes and $\alpha(t)$ linearly changes from 0 to 1 in time. This procedure is somewhat related to *fuzzy logic* [100]. Once the transmission of the attenuator is limited by the finite extinction η_0 at laser powers of about 100 mW the loop filter compensates and starts to reduce the pump current to get to the desired setpoint.

3.2.3.3 Noise Performance

Fluctuations in the laser power on a timescale faster than the feedback bandwidth can lead to heating of the trapped atoms. Compared to our lattice lasers (3.2.5) the IPG fiber

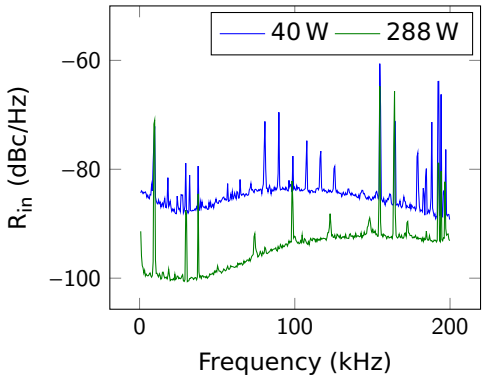

Figure 3.8: Residual amplitude noise of the IPG laser at different output powers

laser exhibits are large amount of residual amplitude noise with multiple peaks reaching to almost $-60\,^{\mathrm{dBc}}/_{\mathrm{Hz}}$ and a baseline noise between $-100\,^{\mathrm{dBc}}/_{\mathrm{Hz}}$ and $-80\,^{\mathrm{dBc}}/_{\mathrm{Hz}}$ depending on the output power level (see figure 3.8). This behavior is expected for an industrial laser designed for material processing. But besides it relatively high noise levels it has been working very reliably over the years. We avoid potential heating issues due to the amplitude noise (1.4.4) by only using this laser for the initial evaporation, while the atoms are still comparably hot and then hand over to different traps with almost negligible heating rates.

3.2.4 Dimple

In our experiment the atoms are trapped a few ¯m below a glass surface (see 3.3.1). Any beam hitting the atoms from the vacuum side of this surface is inevitably going to be partially reflected, even with a good anti-reflection coating. This reflection will form a standing wave pattern below the substrate.

To circumvent this problem, we send in beams from the glass side of the interface through our microscope objective (see 3.3.5). Since the objective contains multiple lenses, double reflection could still cause the light to interfere in the forward direction. By using an incoherent light source with a coherence length less than the typical thickness of a lens (few millimeters), multiple reflections do not interfere in the focus of the trap and cause short wavelength potential corrugations/disorder.

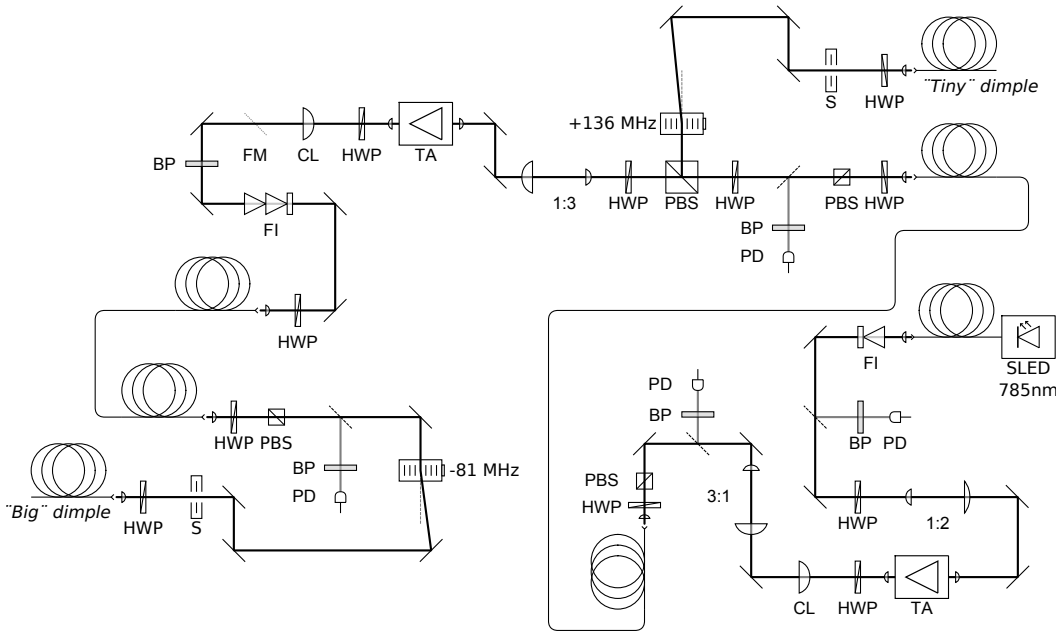

Figure 3.9: Optical setup of the low power optical dipole traps

To provide additional axial confinement in the high-power dipole trap (3.4.6) and during the accordion compression (3.4.7) we shine ∼700 mW broadband light through our objective.

3.2.4.1 Incoherent Light Source

The incoherent light for the tapered amplifiers is generated by a fiber-coupled Exalos superluminescent diode with a center wavelength of 786 nm and a bandwidth of 12 nm outputting 7.6 mW of incoherent light, 5.7 mW in a single polarization. With the temperature and current controller provided by Exalos the residual amplitude noise spectrum showed peaks at 157 kHz ($-107\,^{\mathrm{dBc}}/_{\mathrm{Hz}}$), 316 kHz ($-116\,^{\mathrm{dBc}}/_{\mathrm{Hz}}$), and 997 kHz ($-98\,^{\mathrm{dBc}}/_{\mathrm{Hz}}$). Replacing these with Thorlabs TEC200 and LDC202C resulted in a flat noise spectrum from 50 kHz to 1 MHz at a level of $-128\,^{\mathrm{dBc}}/_{\mathrm{Hz}}$.

3.2.4.2 Tapered Amplifier

The power from the incoherent light source is not sufficient to fully saturate an Eagleyard Photonics 780 nm, 2.2 W output power tapered amplifier. Therefore we use a two-stage

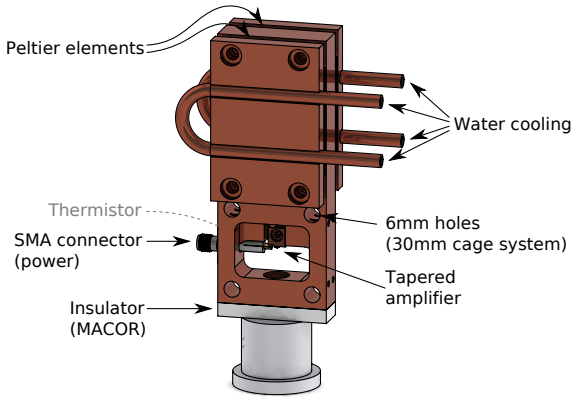

Figure 3.10: Picture of the tapered amplifier mount

tapered amplifier design to obtain powers $> 2\,\mathrm{W}$ out of the second stage amplifier for a seed power of 30 mW and a current of 3.9 A. When carefully mode matched with a cylindrical lens, powers $> 1.1\,\mathrm{W}$ can be achieved after a double-stage optical isolator and a single-mode fiber. Optimizing for fiber coupling efficiency is different from maximizing the bare output power of the tapered amplifier. It seems that the tapered amplifier is not purely single mode and can support multiple spatial modes. Lasing at multiple modes gives an overal higher output powers for the same electric current and seed power, but the fiber coupling efficiency is reduced.

At full power the tapered amplifier produces about 8 W of heat that is extracted using two water-cooled TE Technology, Inc. TE-71-1.4-1.5 Peltier thermoelectric coolers in series, stabilizing the temperature to 19.5°C at a steady-state current of 0.5 A.

Since the output facet of the tapered amplifiers is very elongated the divergence along the horizontal and vertical axis is vastly different. First the weakly diverging axis is collimated with a short focal length aspheric lens. Then the waist size along the other, still diverging axis is mapped out with a beam profiler along the optical axis and fitted to the waist of a propagating Gaussian beam $w(z - z_0)$ with the initial waist w_0 and the waist location z_0 as free parameters. This procedure assumes a perfect Gaussian beam. Allowing for a finite $M^2 > 1$ tends to give worse fit results. Once these parameters are known, one can read off the distance from the waist location z_0 to the point where the waists along both axes

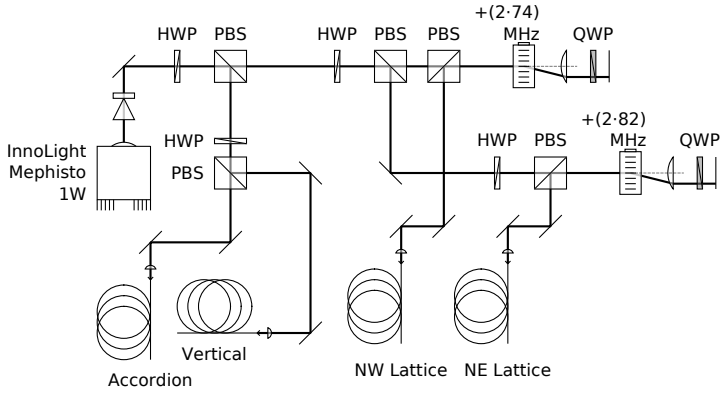

Figure 3.11: Diagram of the optical setup to seed the lattice fiber amplifiers

are equal. A cylindrical lens with that distance as its focal length collimates the beam to a circular near $TEM_{0,0}$ profile.

The final position of the cylindrical lens can be fine-tuned by focusing the beam with a long focal length lens ($\sim$1000 mm) onto a beam profiler and minimizing the astigmatism, i.e. making sure the focus for the two axes is at the same distance from the lens.

3.2.4.3 Blue Detuned Incoherent Light Source for Lithium

Currently a blue-detuned incoherent light source is added into the experiment as well. The basic principles are identical to red-detuned 785 nm system above. The seed is an Exalos EXS0650 free-space superlumindescent diode and a double-stage amplification with EagleYard EYE-TPA-0650-00250 tapered amplifiers. Compared to the infrared amplifiers these have little gain in comparison, only 7 dB, but nevertheless we obtain up to 180 mW of incoherent 650 nm light. This setup is going to be used in future to project repulsive potentials through the microscope.

3.2.5 Lattice

Our three optical lattice beams (3.3.3) and the accordion lattice (3.3.4) are generated from four Nufern NuAMP 50 W single mode fiber amplifiers, each seeded with $\sim$140 mW of 1064 nm light from a InnoLight Mephisto 1 W laser. Their frequencies are shifted with

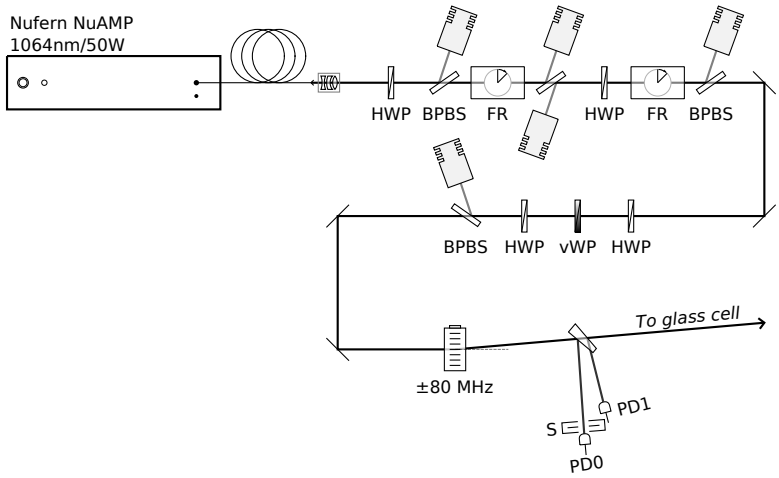

Figure 3.12: Diagram of the optical fiber amplifier power stabilization setup

acousto-optical modulators (figure 3.11).

For future experiments we wanted to potentially allow interference between the two radial lattice beams. Therefore their frequency is made tunable by using double-pass acousto-optical modulator setups. In addition to tuning their frequencies from 74 MHz and 82 MHz to 78 MHz, the polarizations of the lattice beams (3.3.3) will need to be rotated to be p-polarized with respect to the substrate.

3.2.5.1 Power Stabilization

In the experiment we need to be able to stabilize the power of the lattice beams at low power levels of $\mathcal{O}(10\,\mathrm{mW})$ for lattice depths in the Hubbard regime, as well as at high power levels $\mathcal{O}(10\,\mathrm{W})$ during the imaging. Each of the four beamlines has a galvo (Thorlabs GVS or Cambridge Technologies) with a z-cut quartz plate that acts as a variable waveplate depending the galvo angle. In combination with a polarizer this is used as a high-dynamic range attenuator. The beam displacement from the tilting plate is negligible since only small angle changes are necessary to change the retardation by $\lambda/2$.

In the low power regime ($\lesssim 150\,\mathrm{mW}$) the variable attenuation stage is held at a constant, low transmission. The actual power stabilization is done using a Crystal Technology, Inc. AOMO 3080-197 80 MHz acousto-optical modulator, whereas at high power levels the

modulator is operated at maximum diffraction efficiency and the power is controlled via slow digital PI feedback onto the galvo directly.

To have the lowest possible amount of noise added from the power stabilization, at low power levels the rf power going to the acousto-optical modulator is controlled with a mixer driven by a purely analog PI loopfilter designed in our group. To counteract the quadratic dependence of the mixed power on the control voltage, the loopfilter board has a built-in diode circuit that approximates a square-root transfer function.

The $\sim$80 MHz radio-frequencies are created by phase-locked-loop boards based on an Analog Devices ADF4002 locked to our lab rubidium frequency standard. This source has better noise properties than our DDS synthesizers while still being able to tune the frequencies to a particular value.

As for the high-power optical dipole trap (3.2.3), the laser power is measured with two photodiodes to cover a large range of power levels without sacrificing noise performance. Small fractions of the beam are split off with a single Thorlabs BSF10 beam sampler. The uncoated side of the fused-silica wedge is providing the signal for the low power photo diode, the weaker reflection off the side with anti-reflection coating is used for the high power stabilization.

3.2.5.2 Thermal Lensing

The fiber amplifiers were shipped with an $f = 25$ mm BK7 collimation lens. This material is known [139] to show a large amount of thermal lensing. We have observed thermal lensing with LightPath Technologies GRADIUM lenses, lenses with an axial gradient index that compensates for spherical aberrations.

In addition to the lensing issues with the original fiber collimator, the collimation lens is also mounted on-axis with the Losch LD-80 receiver, but the fiber itself is angle cleaved at a 4° angle, causing aberrations. In this case the beam from the fiber hits the collimation lens off-centered and under an angle.

We avoided both problems by using custom machined monolithic copper mounts that

take the polishing angle into account and by choosing OptoSigma 027-0510 $f = 20\,\mathrm{mm}$ fused-silica air-spaced triplet fiber laser focusing lenses for collimation. The large copper block also provides a good heat sink.

Other sources of thermal lensing are the optical isolators (two 30 dB stages, Thorlabs IO-5-1064-VHP) that are required to avoid back-coupling the retro-reflected lattice beams into the amplifiers. This would (and did) immediately destroy the fiber amplifier. Also the thermo-optic dependence of the Faraday rotation causes the isolation to change with optical power [140].

We replaced the cube polarizers in the isolators by Precision Photonics Brewster plate polarizers and only using the original faraday rotator. Since we are always running the fiber amplifiers at a constant output power and attenuate the beams further downstream, we can tolerate potential thermal lensing from the terbium gallium garnet faraday rotator. In addition, the isolators are mounted on water-cooled bases removing any excess heat.

Our acousto-optical modulators are also water-cooled to stabilize the temperature of the crystals and to avoid heating the optical table. No degradation of beam quality in first diffraction order has been observed. In the experiment the power at the acousto-optical modulators is below 200 mW most of the time, because the beam is already attenuated with the variable attenuators.

3.2.5.3 Noise Performance

The optical lattice lasers are most critical for the operation of the experiment. To achieve high fidelity quantum states heating caused by technical noise needs to be minimized. The biggest contribution herefore comes from the amplitude noise of the laser (see 1.4.4).

The seed laser alone has an impressively low noise floor of about $-155\,\mathrm{dBc/Hz}$, but the amplifiers (although in the saturated regime) add more noise on top of that. There are both technical and physical noise sources in the amplifiers.

NuFern in Conneticut generously let us take measurements on one of their test systems, before we ordered our own amplifiers. We minimized the stimulated Brillouin scatter-

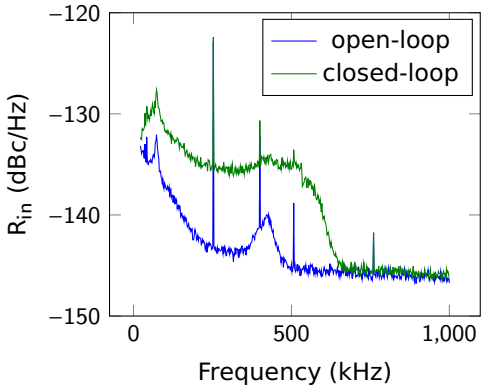

Figure 3.13: Measured residual amplitude noise of a lattice laser beam in open-loop and with active power stabilization

ing [141] in the delivery fiber by shortening them to 50 cm. Since stimulated Brillouin scattering depends exponentially on the laser power, the amplifiers are not running at the full 50 W output power. There is also a broad peak in the spectrum at around 0.7 MHz caused by the relaxation oscillations in the laser medium. It can be completely suppressed by the built-in noise eater in the MEPHISTO seed laser.

Besides those two sources producing broadband noise, there were many discrete peaks caused by various switching power supplies. We suppressed most of those peaks by adding MPE DS26387 line filters to the pump diode power supply, replacing the MEANWELL SP-75-24 power supplies driving the first stage and some of the electronics with a linear supply, and replacing the NATIONAL INSTRUMENTS USB-6008 OEM USB interface with a home-built galvanically isolated interface board. All the power supplies are now located outside the fiber laser enclosure.

Relocating the power supplies also solved a vibration issue: the fan of the power supplies caused the fiber tip to vibrate. These pointing fluctuations were clearly visible on a four-quadrant photo diode.

With all those modifications we significantly improved the residual amplitude of our lattice laser system and only add less than 10 dB of noise in the whole amplification process compared to the bare MEPHISTO noise floor. The achieved noise spectrum is shown in figure 3.13.

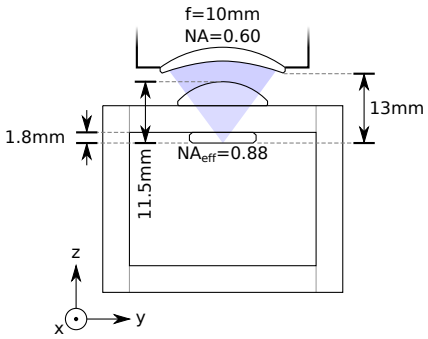

Figure 3.14: Diagram of the microscope setup on the glass cell

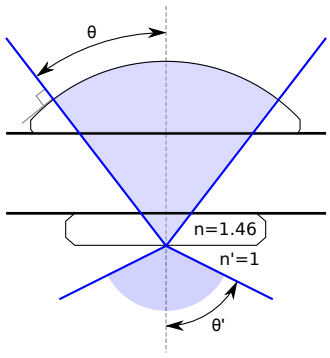

Figure 3.15: Enhancement of the numerical aperture by a hemispheric lens

3.3 Optics

3.3.1 Vertical Imaging: The Microscope

The heart of the imaging system consists of a commercial long working distance objective OPTEM High-Resolution 20X 28-20-46-00 (post-selected to have less than $\lambda/10$ transmitted wavefront error) with a numerical aperture of 0.60, a focal length of $f = 10\,\text{mm}$, and a working distance of 13 mm (see figure 3.15). Interestingly the objective is designed such that the principal plane [86] on the object side lies outside the physical objective, thus allowing a long working distance while still having a short focal length. The back principal plane lies 11.2 mm inside the objective.

3.3.1.1 Optical Resolution

To further enhance the optical resolution the microscope is combined with a hemispheric lens with a radius of curvature of $R = 11.5\,\text{mm}$. That hemisphere is formed by three glass pieces. On the objective side there is a ground down hemisphere with the same radius of curvature and thickness of 4.65 mm made by ROCKY MOUNTAIN INSTRUMENT CO. from fused silica. It is resting on the 5 mm thick glass cell (see 3.1.2) and glued in place with three drops of low outgassing TORR SEAL epoxy along the perimeter. On the vacuum side we optically contacted (see 3.3.1.2) a 1.8 mm thick superpolished substrate from GOOCH & HOUSEGO

with a combined mirror (for 1064 nm) and anti-reflection coating (671 nm and 780 nm) by Advanced Thin Films on the vacuum side that also serves as a mirror for the optical lattice setup (see 3.3.3) and was designed in our group. To guarantee flatness the back of the substrate is coated with silica. Without this compensation coating the stress induced by the anti-reflection/mirror coating on the other side would warp the thin substrate.

The center of the hemisphere is concentric with focus of the microscope. Rays from an on-axis collimated beam that then gets focused by the objective enter the hemisphere normal to the surface. Thus there is no refraction on this interface. But when the rays exit on the bottom, going from an index of refraction of $n = 1.46$ to vacuum with $n' = 1$, the rays get refracted according to Snell's law [86]

$$n \sin\theta = n' \sin\theta'. \tag{3.5}$$

For the marginal rays this directly gives the enhancement of numerical aperture $\mathrm{NA} = \mathrm{n} \sin \grave{}$ of

$$\mathrm{NA}_{\mathrm{eff}} = n\mathrm{NA} \tag{3.6}$$

Alternatively in the limit where the object (i.e. the atoms) are very close to the surface (less than a Rayleigh range) the hemisphere can also be understood as a solid immersion lens [142].

The maximum resolution that could be achieved theoretically with this setup with an effective numerical aperture of $\mathrm{NA}_{\mathrm{eff}} = 0.88$ would be (the so called Rayleigh criterion [86])

$$\Delta r = \frac{1.22}{\mathrm{NA}_{\mathrm{eff}}} \frac{\lambda}{2} = 467\,\mathrm{nm}, \tag{3.7}$$

but as described later, our system suffers from spherical aberration, because the object plane is not exactly at the superpolished surface (see 3.3.1.4). Correcting these aberrations by going away from infinite conjugation is going to slightly reduce the optical resolution. Simulations in Zemax indicate that in the corrected system's resolution should be about 475 nm, still smaller than the lattice spacing of 566 nm.

3.3.1.2 Optical Contacting

Mounting optics inside an ultra-high vacuum chamber is a challenge, because only low outgassing materials can be used. This excludes any (even low outgassing) glues. An additional complication in our experiment is the high laser power. Even a small fraction of the overall power absorbed on a metal piece in vacuum would heat it up quickly, because it only thermalizes through radiation unless it is heatsunk somehow to the air side. There obviously is no convection cooling in vacuum.

We decided to optically contact the superpolished substrate to the glass cell, a process where two sufficiently *flat* and *clean* glass surfaces bond together by van-der-Waals forces and hydrogen bonds — completely without any adhesive.

Superpolished substrate cleaning The superpolished substrates arrived already reasonably clean from the coating run. It is important that the edges are beveled and polished so that there are no glass crumbs being dragged across the superpolished surface in the cleaning process. Fused silica is hard enough to scratch fused silica (so are most metals that have a protective oxide layer, like aluminum, titanium, non-stainless steel)! Light scattering from imperfections in the surface can later create disorder in our optical potentials. Since the electric fields directly enter the interference term, not the intensities, a small amount of scattered light can create a surprisingly large corrugation. For example, 100 ppm scatter creates 1% disorder.

To remove residual dust particles the substrate was mounted on a MTI VTC-100 spin coater under a HEPA filter and spun at 2000 rpm. The spinning glass piece was flushed with high purity isopropanol C_3H_7OH and wiped several times radially from the center outwards with Coventry 52121 pillow tip swaps while still flushing it with isopropanol. The solvent was then flushed away with plenty of HPLC grade water H_2O and the substrates blown dry with ultra-high purity nitrogen gas N_2.

Attempts to etch/activate the superpolished surface with an aqueous solution of potassium hydroxide KOH failed, leaving a permanent milky finish on the surface, probably

because it increased the surface roughness, and attacking the anti-reflection coating.

Glass cell polishing and cleaning Our weapon of choice for cleaning the glass cell is RCA1 solution [143], a mixture of one part by volume 33% ammonia NH_4OH, two parts 30% hydrogen peroxide H_2O_2 (not stabilized), and seven parts HPLC grade water H_2O. It is used in the semiconductor industry and it can remove organic as well as particulate contamination. In addition it can alter the surface termination and create hydroxyl groups that aid the optical contacting to other surfaces. This effect is known as *chemically activated bonding*.

A first cleaning step was performed, removing all major contamination by the following procedure:

1. Sonicate[2] glass cell filled with RCA1 in a large beaker of pre-heated RCA1 at 80°C for 1 min.
2. Flush thoroughly with HPLC grade water H_2O.
3. Wipe outside of the glass cell with lint-free lens paper Berkshire Lensx 90, semiconductor grade methanol CH_3OH, and a large hemostat and a good amount of pressure.

It is important that the solvent bottles have not been opened before. Pure solvents attract water from the humidity of the air. After a few hours of exposure (even with the lid on) the water causes residue after the cleaning process.

To remove the remaining glass particles on the inside surfaces (see section 3.1.2) we tried several ways of polishing. The first attempt to use a modified electric toothbrush with a polishing pad glued to it turned out to be too tedious. A specially designed polishing jig made a more controlled process possible, but removed too much material (many λ in thickness). At the end it turned out to be sufficient to use 250 nm polishing paste (with rounded particles) directly on a polyester swap and only slightly scrub the inside only to

[2]Many people discuraged use of a ultrasound bath, because it could potentially undo the bonds. We have sonicated our glass cells many times without a single incident. Most likely this was possible, because our cells had been heated/annealed multiple times at various production steps as indicated by the degradation in surface flatness. I would *not* recommend to sonicate a "proper" glass cell.

remove particles stuck to the surface without repolishing the surface itself.

After the polishing the inside was now contaminated with polishing paste. This time more thorough cleaning steps were required:

1. Flush the inside with tap water under high pressure e.g. from a faucet, forced through a small nozzle.
2. Rinse with deionized water.
3. Blow dry with ultra-high purity dry nitrogen N_2 through with a 1 μm particle filter.
4. Repeat until there is no more residue from the (oil of the) polishing paste visible.
5. Soak in dichloromethane CH_2Cl_2 for 10 min.
6. Rinse with deionized water.
7. Fill with RCA1 and soak in RCA1 at 80°C for 25 min.
8. Sonicate in the RCA1 solution for 30 s.
9. Flush thoroughly with HPLC grade water.

Optical Contacting Since the glass cell was slightly concave after the flange had been fused on, mechanical force had to be applied inwards to bend the glass cell face until the inner face was convex (approximately one fringe over 1 cm). The pressure was applied by carefully tightening screws that pressed down a "X" shaped holder that, in turn, pressed on a thin Teflon ring sandwiched between the cell and a 1 in glass blank. The whole bending process was monitored in real-time in an white light interferometer and a low magnification microscope.

For the optical contacting the superpolished substrate was wetted with 3 μl of HPLC grade water. Adding a small amount of water can help, because it is possible to bond surfaces over a larger distance with the help of several hydrogen bonds in the gap [143].

The substrate itself was resting on a small lip on top of an inverted brass cone that was sitting in a hole of a long 1/4 in thick stainless steel bar. This way the substrate could still tip and tilt to conform to the surface in case the bar was not perfectly parallel to the glass cell. The plan was to lower the glass cell onto the substrate to perform the contacting. But when we slightly tapped the stainless steel bar with the substrate already parked below the correct

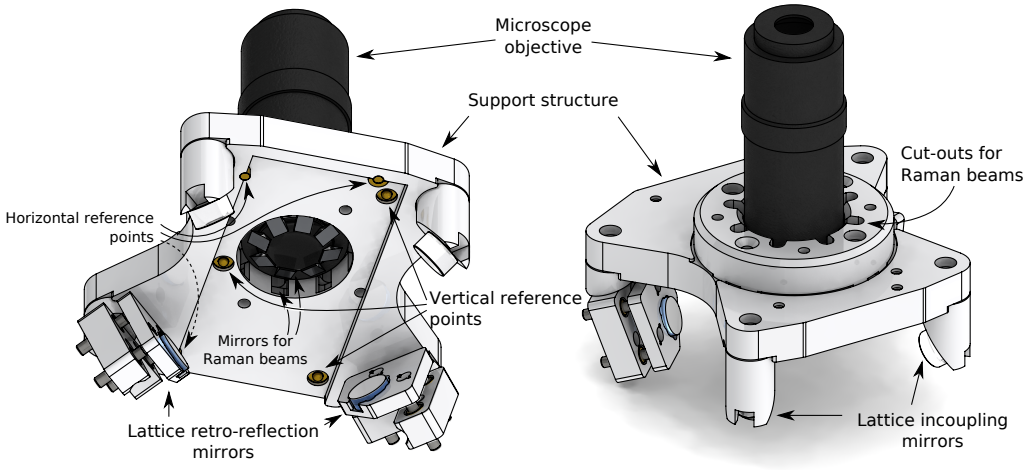

Figure 3.16: Ceramic support structure for the microscope objective and lattice mirrors

spot, it jumped up a little and immediately stuck to the glass cell. Even after releasing the bending clamp, baking-out under vacuum and other tortures it is still attached! The fact that the substrate is only 1.8 mm thick was essential to help to conform to the warped glass cell.

3.3.1.3 Objective Mount: Exoskeleton

It is crucial for the experiment that the position lattice with respect to the atoms in the optical lattice remains constant. Although we could tolerate slow lateral drift, the relative distance between the atoms and the objective needs to be stable since the depth of field is only $\sim$900 nm. Our approach to obtain the required stability is to mount the microscope objective and the lattice optics monolithically to a common support structure.

The vertical lattice ($\sim$0.5 µm spacing) from the bottom and the vertical contribution ($\sim$1.5 µm spacing) of the radial lattice are interferometrically referenced to the superpolished substrate of which they reflect off. A support structure holding the lattice in-coupling and retro-reflection optics (see figure 3.16) is glued to the top of the cell with five minute epoxy. This structure is completely made from machinable ceramic (Macor) that can withstand heat from an accidental hit with high power laser and is non-conductive and non-magnetic, so that it does not interact with the strong magnetic fields created by the Feshbach coils. To

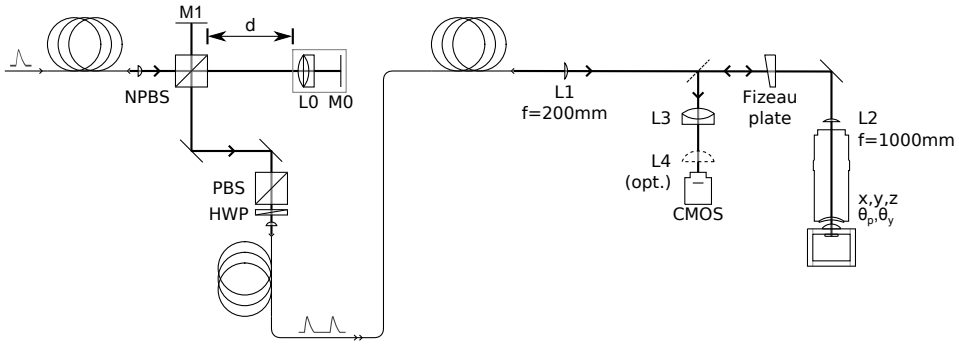

Figure 3.17: Objective alignment with delay line and Fizeau interferometer

provide a stable point of contact with glass three short brass pieces with round polished tips are rigidly screwed into the ceramic piece. To constrain the support in the horizontal plane we have three little brass cylinders that contact the outside of the glass cell. Brass has low electrical conductivity, is non-ferromagnetic (unlike stainless steel), and most importantly does not scratch glass (unlike aluminum, titanium, or most other metals with an oxide layer). The kinetic mirror mounts for the retro-reflectors are made from MACOR as well. Only the NEWPORT adjuster screws are from stainless steel.

After the objective had been correctly aligned (see next chapter 3.3.1.4) it was glued into a ring that is screwed to the support structure. Fine focusing is done using the camera position. If the objective ever has to be realigned, it is possible to undo the screws and swap out the objective including mounting ring.

3.3.1.4 Objective Alignment

To get the best optical performance the microscope objective needs to be aligned interferometrically to the hemisphere (concentric) and the superpolished substrate (normal). A conventional interferometer typically uses coherent laser light to interfere a reference beam with a reflected beam. In the case of a microscope objective with many internal lens surfaces there would be too many reflection to identify each surface individually. A solution to this problem is to use an incoherent light source and a *white light interferometer*, where the path lengths in both arms have to match within the coherence length of the light.

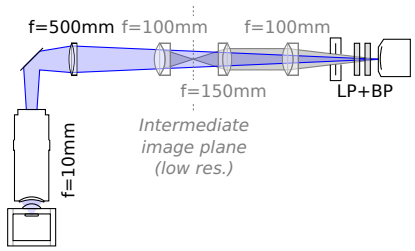

Figure 3.18: Optical setup for the high resolution vertical imaging with optional de-magnification for debugging purposes

Although in our setup we used the incoherent light from a superluminescent diode (see 3.2.4), it is conceptually easier to think about a pulsed laser. For simplicity of the setup near the objective we used a Fizeau interferometer [144], but there is no possibility to independently vary the path lengths of the interferometer arms. To circumvent this limitation a fiber-coupled optical delay line with a Michelson interferometer [86] (see figure 3.17) is used to generate incoherent light that has a tunable interference revival. Using a cat's eye reflector consisting of a lens and a flat mirror, the delayed arm remains fiber coupled while varying the distance d to "scan" through various glass surfaces inside the objective and the hemisphere. Only the reflected beams from the Fizeau plate and the "selected" surfaces interfere on the CMOS camera. For coarse alignment an additional lens L2 can be introduced to image the Fourier plane, where the reflected beams are just dots that need to be overlapped.

During the whole alignment process the objective is mounted on mirror mount with two rotational degrees of freedom and a three-axis translation stage, before it was permanently glued to the exoskeleton with Torr Seal epoxy. In the lateral direction the objective was focused with a 1 m lens (L1) attached to the back of the objective and then moved towards the hemisphere with a micrometer by 75 µm. This theoretically compensates for spherical aberation for an object plane 16 µm below the substrate. This lens was removed after the alignment and is not part of the imaging system.

3.3.1.5 High Resolution Imaging

The imaging system is completed with a THORLABS AC508-500-B 500 mm achromatic lens that images the atomic cloud onto our CCD camera. To align this lens we first setup a laser beam along the optical axis down into the microscope (without the lens in place) and made sure that all reflections from the objective lens/hemisphere are being reflected back into itself. This ensures that both the angle and position of this beam are aligned with the optical axis of the microscope. Finally the 500 mm lens is placed into the beam such that the reflection of the lens surface is going back the right way and that the reflections from the hemisphere/substrate are still aligned with the reference beam as well. Since we are not using the microscope in an infinite conjugate ratio setup our magnification is $M = 130$ instead of $f_{\mathrm{AC}}/f_{\mathrm{Objective}} = 50$. A sketch of the whole imaging setup is shown in figure 3.18.

In the coming weeks a custom correction plate will be mounted at the back of the objective to correct for some higher order aberations.

3.3.1.6 Low Resolution Imaging

The field of view of the high resolution imaging is about 200 µm × 200 µm. While this is more than plenty for imaging atoms inside an optical lattice, for time of flight imaging (to measure temperatures) or alignment we need the option to have a lower magnification/larger field of view. This is done by creating an intermediate image with lower magnification and then re-imaging this image with a $4f$ setup. This allows us to keep the camera in the same place as for the high-resolution imaging (3.3.1.5) and just drop in three lenses to reduce the magnification to $\times 10$ (see gray elements in figure 3.18). The intermediate image plane allowed us to use a mechanical chopper in the early stages of the Raman imaging (2.9).

3.3.2 Horizontal Imaging

For alignment and debugging purposes we also need to be able to do absorption imaging [85] a cloud of atoms near ($\sim$100 um and closer) the superpolished substrate (see section 3.3.1) from the side. It is difficult to image a cloud from the side due to knife-edge diffraction at

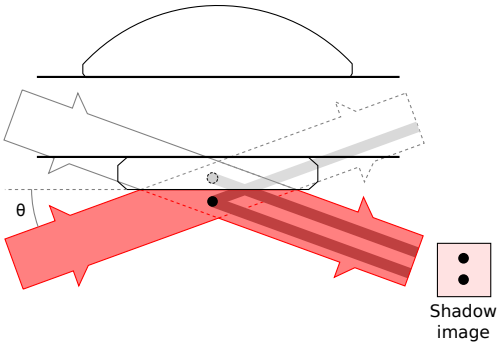

Figure 3.19: Absorption imaging of a cloud of atoms near the substrate

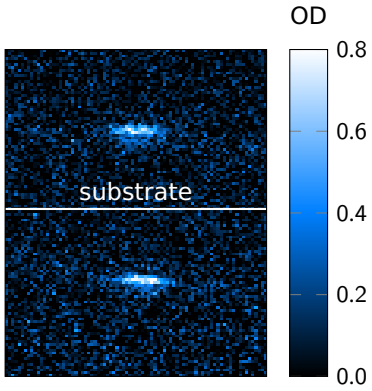

Figure 3.20: Atoms in a crossed optical dipole trap near the substrate with its mirror image

the side of the substrate. This is a well-known problem in the atom chip community [145] and can be somewhat improved by imaging in reflection under grazing incidence.

This imaging technique introduces another artifact, a double image. It can be understood as a second image that gets formed by the mirror image of the imaging beam getting attenuated by the mirror image of the atom cloud (see figure 3.19). Besides allowing to recover some signal that would be lost otherwise, the distance from the substrate can be extracted from the images (for rotationally symmetric clouds and/or small angles θ). It is located right in between the two images (see figure 3.20).

In our setup the imaging laser beam spans an angle of $\theta = 4.2°$ with the surface of the superpolished surface. Only a small fraction of the light is reflected due to the anti-reflection coating. That in turn means for a reasonably low saturation parameter, very little light gets actually reflected into the camera path. The atoms then are imaged with an Infinity K2 DistaMax lens with a CF-3 objective (85 mm–98 mm working distance, magnification of $\sim$3.5, and a theoretical resolution of 1.7 um) onto a PointGrey Flea3 FL3-GE-03S2M-C (7.4 µm pixel size, 648 × 488 pixels). Since the substrate blocks almost half of the numerical aperture of the lens, expected resolution is reduced. In addition even under such shallow angles a cloud of 50 µm horizontal depth, the geometric vertical spread is already about 4 µm. A calibration using atoms in the accordion lattice (3.3.4) at a suggests that the effective magnification in our setup is $2.3(2)\,{}^{\mu m}/_{px}$.

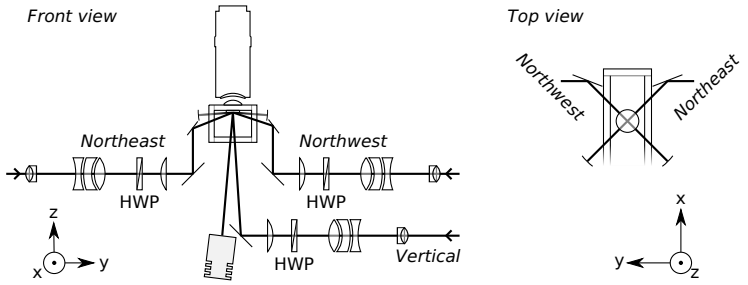

Figure 3.21: Mode matching and focusing optics of the optical lattice

3.3.3 Lattice

The condensed matter problems we are trying to address with our experiment fundamentally requires the presence of an optical lattice. While in most traditional optical lattice experiment this is done by overlapping three orthogonal optical lattices [101], our high-numerical aperture microscope takes away a large amount of the optical access. Therefore an alternative way introduce the optical lattice has been chosen with its own challenges and benefits that are described in the following.

3.3.3.1 Lattice Geometry

The optical lattice is created from three NUFERN NUAMP 50 W 1064 nm ytterbium-doped fiber amplifiers seeded by an INNOLIGHT MEPHISTO 1 W Nd:YAG laser (see section 3.2.5). Since all three lasers are frequency shifted in the current configuration there is no mutual interference (although they could be tuned to create double-well lattices for future experiments).

Geometrically it is impossible to send in the lattice beams parallel to the superpolished substrate and still have the atoms be trapped close to it. Our solution to this problem is to reflect the radial ($x + y$ and $x - y$ direction) lattice beams off the substrate under a $\theta \sim 20^\circ$ angle and then retro-reflect the beam back into itself (see figure 3.21). This creates an interfering $\phi = \pi/2$ lattice pattern (see equations (1.97) and (1.119)) in a horizontal plane. The distance of the retro-reflector to the atoms was chosen such that the radius of curvature of the mirror ($R = 50\,\text{mm}$) is identical to the wavefront curvature of the Gaussian

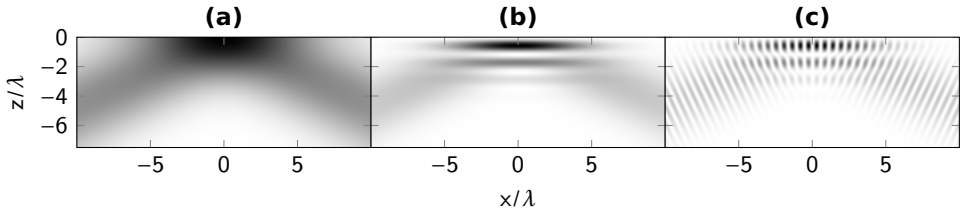

Figure 3.22: Intensity pattern of a completely incoherent beam (a), a coherent beam (b), and a retro-reflected coherent beam (c) reflected off the superpolished substrate with a Gaussian beam waist $\sim\mathcal{O}(\lambda)$ to exaggerate the differences

beam (1.65). The diffraction causes the radius of curvature to be greater than expected from geometrical optics. Therefore the mirror needs to be closer than its radius. Fine-tuning of the position can be achieved by turning all three adjusters of the retro-reflector kinematic mount by the same amount.

Since there are effectively four beams interfering, namely the incoming beam, the retro reflected beam, and their mirror images from the reflection on the substrate, the lattice depth is enhanced by a factor of four (see equation (1.99)) over the case where they would be just counterpropagating beams. This is especially useful for our imaging (see 2.9), where we require tight confinement and a deep optical lattice. One downside of this geometry is that the radial/horizontal ($x-y$) and axial/vertical (z) confinement is not decoupled.

A second beam in the same geometry, but rotated by 90° around the z axis, provides the optical lattice in the perpendicular direction in the $x-y$ plane. Looking from the top the resulting two dimensional lattice in that plane is a conventional non-interfering $\phi = 0$ lattice with a spacing of 566 nm in both directions. For the lattices to line up in the z direction, the angles have to be matched better than $\pm 0.3°$ for the maxima to line up within $\pm 10\%$ of the lattice spacing of 1.55 µm in that direction (see 3.3.3.2).

To increase the vertical (z direction) confinement the third lattice beam is directly reflected off the substrate at near-normal incidence ($\sim 5°$ degrees from normal to match the potential maxima with the large spacing vertical lattice created by the radial lattice beams) giving rise to a vertical lattice spacing of 534 nm.

3.3.3.2 Lattice Alignment

The superpolished substrate in our experiment serves as a reference surface. This significantly simplifies the alignment. Once one of the lattice beams (including the accordion lattice 3.3.4) is aligned to the correct spot in the horizontal (x, y) plane, its position on the substrate can be seen from below by looking at the Rayleigh scatter with a conventional camera (PointGrey Chameleon) with the infrared filter removed both on the camera itself and the lens (Edmund Optics 50 mm$/f2$). This allows us to coarsely align all the other beams to the same spot, including their retro-reflected beams, although the fine alignment still needs to be done using atoms.

In addition to the pointing the angles with respect to the superpolished substrate of the radial lattice beams have to be matched as explained above. At the time of this work the angles have only been matched by centering the beams on the retro-reflectors. Considering that it is possible to center it better than 1 mm and the retro-reflector is roughly 5 cm away from the center of the substrate, this procedure should yield in an uncertainty of $\sim 1^\circ$. Once the experiment is setup to only produce a single pancake, this alignment and the overlap with the 0.5 µm vertical lattice is going to become crucial and other means of aligning the angles have to be found. Possible techniques could be:

- Measure the differential ac Stark shift by imaging atoms in-trap. The shift should be maximized when all lattices are overlapped.
- Measure the vertical trap frequency. The frequency should be maximized when all lattices are overlapped. This method is less sensitive, because of the square-root dependence of the trap frequency.
- Make a molecular Li_2 Bose-Einstein condensate and perform Kapitza-Dirac scattering [146].
- Drive odd vibrational transitions in the vertical lattice created by the first lattice axis by modulating the depth of the second lattice axis.

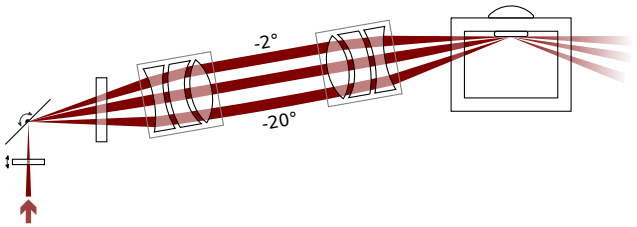

Figure 3.23: The surface of a galvo mirror is imaged onto the superpolished to create a variable spacing vertical optical lattice.

3.3.4 Accordion

To load the optical lattice near the superpolished substrate we first load the atoms into a vertical one-dimensional standing wave with tunable lattice spacing.

Initially the atoms are loaded into the fifth maximum of a $\sim$15 µm lattice that is then continuously compressed to 1.5 µm spacing while being transported upwards. The detailed loading and compression procedure is described in more detail in 3.4.7.

The lattice spacing is varied by changing the angle of incidence of the laser beam on the reflective coating of the superpolished substrate. This is achieved by imaging the surface of a galvo mirror (Thorlabs GVS301) on the substrate via an $4f$ imaging setup consisting of two OptoSigma 027-0540 $f = 50$ mm triplet lenses (see figure 3.24). A second Thorlabs galvo with a $t = 3$ mm thick anti-reflection coated glass window is used to dynamically correct the pointing by displacing the beam. The amount of displacement d as a function of

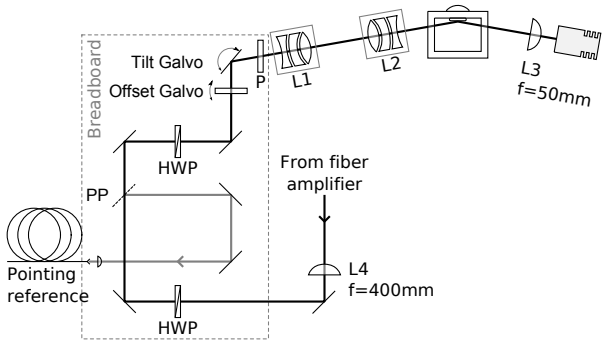

Figure 3.24: Optical setup of the accordion lattice

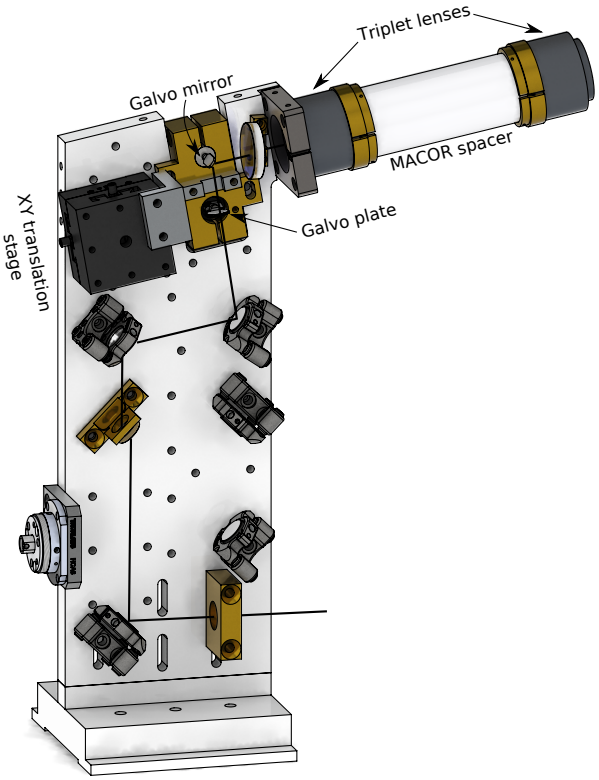

Figure 3.25: Mechanical setup of the accordion lattice

the angle of incidence θ is given by

$$d(\theta) = t \sin\left(1 - \frac{\cos\theta}{n' \cos\theta'}\right), \tag{3.8}$$

where the interior angle is given by Snell's law (3.5) $n' \sin\theta' = \sin\theta$ and n denotes the index of refraction ($n \sim 1.46$ for fused silica).

The $4f$ imaging telescope has to have a fairly large numerical aperture to cover the 20° angle range. This in turn requires the optics to be close to the glass cell and the Feshbach coils. To minimize eddy currents while still being non-ferromagnetic and structurally very rigid, the vertical bread board shown in figure 3.25 was machined from titanium. The lenses themselves are spaced with a ceramic tube with threaded brass rings glued on. The brass rings are slit to minimize eddy currents, although this is a very minor effect compared to the aluminum housing of the lenses. Fine positioning of the two galvos is achieved with a $x - y$ translation stage. The positions of the in-coupling mirrors were calculated a-priori, so

that they could be mounted directly onto the breadboard.

3.3.4.1 Astigmatism Compensation

The propagation of a laser beam through a tilted glass plates produces aberrations in the beam. Most dominantly these are astigmatism (different foci for two orthogonal axes) and coma [144, 86].

It is not straight forward to decide whether that plate should be parallel to the glass cell or have the opposite tilt. Those two cases correct different aberrations. For our beam parameters simulations with ZEEMAX that the minimum focus shift (as a function of the galvo tilt angle) was achieved by introducing an anti-reflection coated glass plate with the same thickness as the glass cell ($t = 5\,\mathrm{mm}$) before the telescope. The compensation plate is parallel to the side of the glass cell.

3.3.4.2 Accordion Alignment

For the initial coarse alignment we mounted a fiber coupled 1064 nm laser onto the vertical breadboard. This way we can move the assembly around without having to continuously realign the laser beam before the breadboard. As for the lattice alignment 3.3.3.2 we can use the Rayleigh scatter off the superpolished substrate to locate the accordion lattice beam.

Since the Gaussian beam waist is fairly large with 200 µm the axial alignment is not critical and the focus only has to be correct within a Rayleigh length (1.64) $z_\mathrm{R} \approx 12\,\mathrm{cm}$. It is more important that the focus is on the axis of rotation of the galvo mirror.

The fine alignment was done by slowly scanning the galvo between the two extreme angles ($2^\circ \ldots 20^\circ$) and adjusting the $x - y$ translation stage until it the spot on the substrate did not move anymore.

The astigmatism compensation plate (see 3.3.4.1) allows us also to calibrate the galvo tilt angle within machining and assembly tolerances. Herefore the galvo tilt is adjusted that the back reflection off the compensation plate goes back into itself. By design this corresponds to a 10° angle.

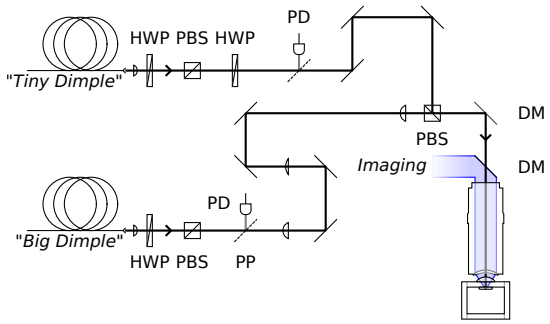

Figure 3.26: Optical setup of the tiny and big dimple trap

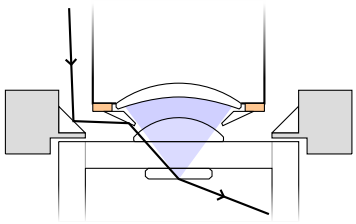

Figure 3.27: Close-up view of the σ Raman beam near the hemisphere

3.3.5 Dimples

Under shallow angles the accordion lattice provides very little confinement in one direction. To counteract it is overlapped with the "big dimple" trap, a perpendicular optical dipole trap with a $\sim$30 µm Gaussian beam waist that is sent through the microscope objective. To get such a large feature size in the image plane of the objective it is necessary to focus/collimate the ingoing beam at the Fourier plane (inside the objective) to $\sim$80 µm. This seems to cause slight aberrations in the image plane, a ring around the central spot, although we could never exclude that this was not an artifact of the imaging process.

For an alignment purposes and more efficient cooling [147] we also have a very tight optical dipole trap with $\sim$6 um Gaussian beam waist, the "tiny dimple". A similar trap has been used recently to produce samples of ^{6}Li with a fixed atom number [148].

The dimple beams get sent into the objective through the transmitted port of a dichroic mirror (DM) that splits off the fluorescence collection arm directly over the back of the lens. A second dichroic mirror combines the blue- and red-detuned lasers (see 3.2.4) at 650 nm and 785 nm.

All those beams can conveniently be aligned to the hemisphere. Coming out of the objective there are two major reflections: one reflected off the bottom of the superpolished substrate, and one from the hemisphere. The latter one is less sensitive to changes in the input alignment, because the hemisphere and the superpolished substrate for a "cat's

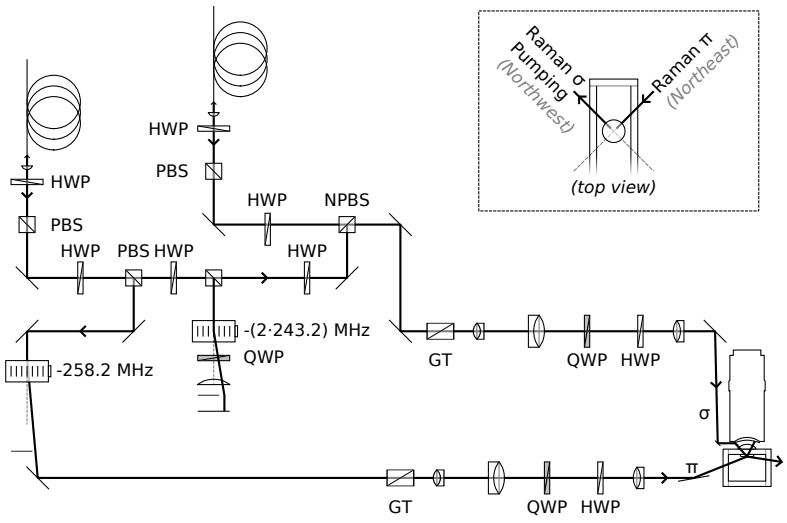

Figure 3.28: Optical setup of the Raman beams

eye" retro-reflector. Also the two reflection move the opposite direction. When all those reflections overlap, the beam is centered under the hemisphere.

3.3.6 Raman

To avoid differential phase noise between to the Raman legs, the Raman light originates from a single fiber and is then split in two on the optical table of the experiment. The π-component is shifted with a single pass that is also used to pulse the beam, the σ-component is shifted and shuttered with a double-pass acousto-optical modulator. By choosing the double-pass frequency one can control the two photon detuning of the Raman beam. The frequencies are also chosen such that electronic crosstalk between the two acousto-optical modulators is minimized.

The optical pumping beam is overlapped with the σ-polarized Raman beam and sent into the chamber through the hemisphere outside the numerical aperture of the objective $\sin\theta = 0.60$ ($\Rightarrow \theta = 36.9^\circ$), which limits the available angle range on one side. On the other side the angle is limited by the total internal reflection angle

$$\theta_{\mathrm{TIR}} = \arcsin\frac{1}{n'} = 42.3^\circ. \tag{3.9}$$

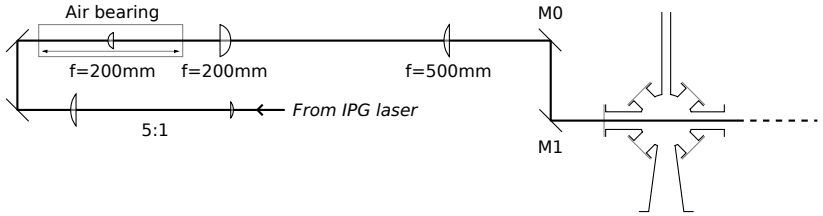

Figure 3.29: Optical setup of the high power dipole trap

We mounted eight small angle mirrors directly to the microscope objective, which allow us to send the beam into the hemisphere under an angle that is compatible with the constraints. A beam path is depicted in figure 3.28. In this configuration the Raman and optical pumping beam is along one of the radial lattice axes and $\sim$15° titled away from the superpolished substrate.

The π-polarized Raman beam on the other hand is introduced from below through the back of one of the lattice incoupling mirrors along the orthogonal radial lattice axis and $\sim$20° from the substrate. The whole setup is visualized in setup in figure 3.28.

3.3.7 High Power Optical Dipole Trap

The laser beam is focused onto a $\sim$20 µm spot with a $f = 200$ mm lens that is mounted onto a AEROTECH ABL10100 air bearing stage with $\sim$100 mm of travel. The ability to move the focus allows us to transport atoms in an red-detuned optical dipole trap [149]. A $4f$ imaging system with a magnification of $\times$2.5 enhances the effective travel by a factor of $2.5^2 = 6.25$ and enables us to transport over a distance of > 60 cm from the main chamber into the science chamber. The transport sequence is described in great detail in section 3.4.5.

In addition the second to last kinetic mirror mount M0 is motorized with two NEWPORT PicoMotors to align the position of the optical dipole trap in the science chamber on a daily basis. For continuous control over the vertical distance from the super polished substrate, another adjuster on M1 is controlled with a large-travel piezo.

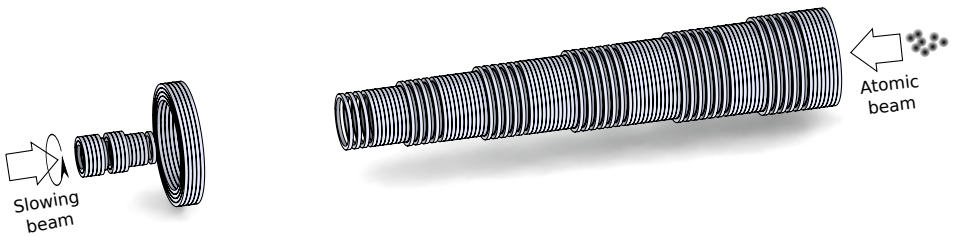

Figure 3.30: Coil pattern of the Zeeman slower

3.4 Sequence

3.4.1 Atomic Beam Source

The atomic beam emerges from a two-species sodium-lithium oven base on the MIT design [150]. For the experiments described in this work the sodium section has been turned off, with only the sodium nozzle left at 400°C. The lithium reservoir is heated to 380°C, being well in the liquid phase and giving a vapor pressure on the order of 10^{-4} torr [151]. To prevent clogging and formation of a sodium-lithium alloy the nozzle itself is heated to 450°C.

Downstream the beam is collimated by a 0.4 in bore in a copper coldplate at room temperature and then shuttered with a thin copper sheet mounted to a UHV Design MagiDrive magnetic rotary feedthrough operated by a hobby grade servo motor.

After five years of moderate operation the coldplate shows a significant layer of alkali metal, a few millimeter thick. Most certainly this is caused by the high sodium flux in the early stages of this experiment, but should not pose a problem in the current mode of operation with only lithium.

3.4.2 Zeeman Slower

In a Zeeman slower [57] atoms from an atomic beam moving at a velocity $\mathbf{v}$ get continuously slowed down by a counterpropagating resonant laser beam with the wavevector $|\mathbf{k}_\mathrm{L}| = 2\pi/\lambda$. To compensate for the change in doppler shift $-\mathbf{k}_\mathrm{L} \cdot \mathbf{v}$ due to the deceleration, a spatially varying magnetic field Zeeman shifts the atom transition back into resonance to fulfill the

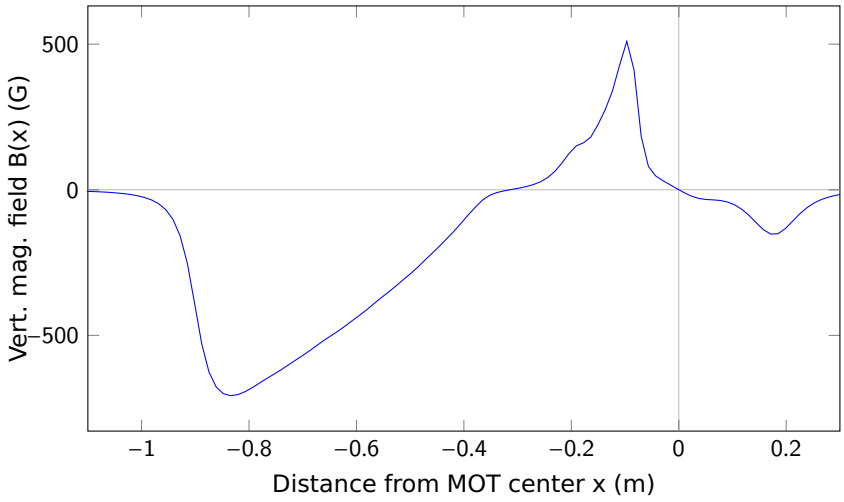

Figure 3.31: Calculated magnetic field profile of the Zeeman slower

resonance condition

$$-\frac{1}{\hbar}\boldsymbol{\mu}\cdot\mathbf{B}(z)-\mathbf{k}_{\mathrm{L}}\cdot\mathbf{v}(z)+\delta=0, \tag{3.10}$$

where $\delta = \omega_{\mathrm{L}} - \omega_0$ denotes the detuning of the laser frequency ω_{L} from the atomic resonance at zero field ω_0. The difference in magnetic moment μ of lithium atoms in the stretched states $\left|2^2\mathrm{S}_{1/2}(F = {}^3/_2, m_F = \pm{}^3/_2)\right\rangle$ and $\left|2^2\mathrm{P}_{3/2}(F = {}^5/_2, m_F = \pm{}^5/_2)\right\rangle$ is equal to one Bohr magneton $|\boldsymbol{\mu}| = \mu_{\mathrm{B}}$. A more detail description of the theory and design of our Zeeman slower can be found in [134].

After the sodium section of the oven had been retired, the Zeeman slower parameters were re-optimized to maximize the capture efficiency for the lithium atoms emerging from the oven. By running the slower at slightly higher currents yielding a magnetic field ranging from $B_0 = -707\,\mathrm{G}$ to $505\,\mathrm{G}$ (figure 3.11). By increasing the detuning to $\delta = -800\,\mathrm{MHz}$, the capture velocity

$$v_{\mathrm{cap}} = \frac{\frac{\mu}{\hbar}B_0 - \delta}{k_{\mathrm{L}}} \tag{3.11}$$

increases to $1200\,\mathrm{m/s}$.

Integrating up the velocity profile of the atomic beam [152]

$$\frac{\mathrm{d}N(v)}{\mathrm{d}v} = 2N\frac{v^3}{v_{\mathrm{p}}^4}\exp\left(-\frac{v^2}{v_{\mathrm{p}}^2}\right) \tag{3.12}$$

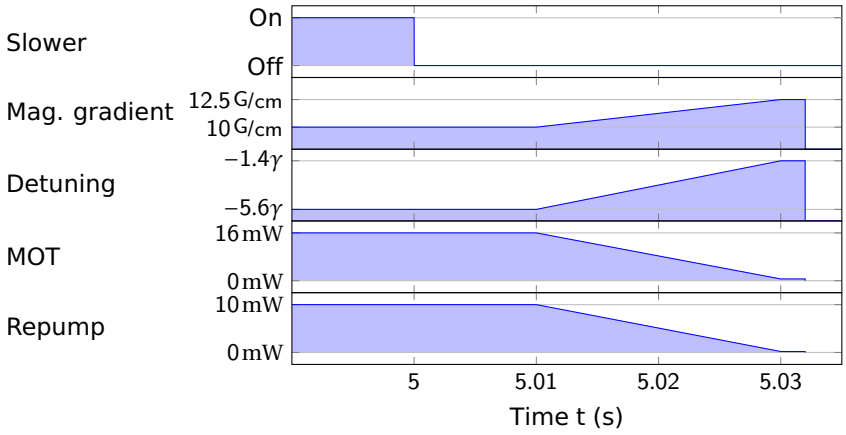

Figure 3.32: Magneto-optical trap loading sequence

below that capture velocity gives a theoretical efficiency of 16.5%. The most probable velocity v_p of a pure Maxwell-Boltzmann distribution is given by $v_p = \sqrt{2k_B T/m}$. This is different from the maximum of (3.12) $v'_p = \sqrt{3/2}v_p$.

The total laser power used in the Zeeman slower beam is about 60 mW, including 228 MHz sidebands created with an electro-optical modulator for repumping in the zero field region.

With this setup the final velocity is expected to be on the order of 60 m/s. Since collisions are negligible within the atomic beam, the resulting velocity distribution is technically not a thermal distribution. The most probable velocity would correspond to temperatures of about 1 K.

3.4.3 Magneto Optical Trap

To cool further decrease the temperature and increase phase space density, atoms leaving the Zeeman slower are captured in a magneto-optical trap (MOT) [153]. A magneto-optical trap can be understood as a three dimensional extension of a Zeeman slower, where atoms are experiencing a dissipative force from all sides, cooling and trapping them in the center of a quadrupole magnetic field and six laser beams. Our magneto-optical trap setup is already described in [134] and theory is extensively discussed in [57].

Initially the magneto-optical trap with $\approx 10^8$ atoms is loaded at a detuning of $\delta = -2\pi \cdot 33\,\mathrm{MHz} = -5.6\gamma$ and magnetic field gradient of $10\,\mathrm{G/cm}$ along the weaker axes of the quadrupole field for 5 s. Each laser beam typically has a laser power of about 16 mW on the $\left|2^2\mathrm{S}_{1/2}(F = 3/2)\right\rangle \rightarrow \left|2^2\mathrm{P}_{3/2}\right\rangle$ ("MOT") transition and 10 mW on the $\left|2^2\mathrm{S}_{1/2}(F = 1/2)\right\rangle \rightarrow \left|2^2\mathrm{P}_{3/2}\right\rangle$ ("repump") transition with a Gaussian beam waist $w_0 \approx 8\,\mathrm{mm}$. The actual laser power drifts slightly from day to day, because of slow polarization drifts in the fibers coming from the Evanescent Optics Inc. polarization maintaining fiber splitter used to combine the MOT and the repump light.

During the last 20 ms an optical dipole trap (see 3.2.3) overlapped with the magneto-optical trap is turned on. Its Gaussian beam waist is $w_0 = 54\,\mathrm{um}$ at a maximum laser power of 255 W and a center wavelength of $\bar{\lambda} = 1070\,\mathrm{nm}$. This corresponds to a trap depth of 3.3 mK, which is significantly deeper than the temperatures expected in the magneto-optical trap.

The mode overlap can be improved further by compressing the magneto-optical trap after the Zeeman slower has been turned off. In our setup this is done by reducing the detuning to $\delta = -2\pi \cdot 8\,\mathrm{MHz} = -1.4\gamma$ linearly over 20 ms, while also reducing the laser power to 0.6 mW for the MOT light and 0.2 mW for the repump light and increasing the magnetic field gradient to $12.5\,\mathrm{G/cm}$. This compressed magneto-optical trap (cMOT) is only a transient effect. In steady state a majority of atoms are lost, when going to very near detuned light.

By ramping the repump laser faster than the MOT laser, atoms start to get preferentially pumped into the $\left|2^2\mathrm{S}_{1/2}(F = 1/2)\right\rangle$ state, the lowest energy states of the system. There they are not subject to spin-changing collisions at the high densities in the optical dipole trap.

In our experiment we are not set up to directly measure the temperature in the magneto-optical trap. But the temperature after the transfer to the optical dipole trap is measured to be 800 μK, which is a few times higher than the Doppler temperature

$$T_\mathrm{D} = \frac{\hbar\gamma}{2k_\mathrm{B}} = 139\,\mu\mathrm{K}, \tag{3.13}$$

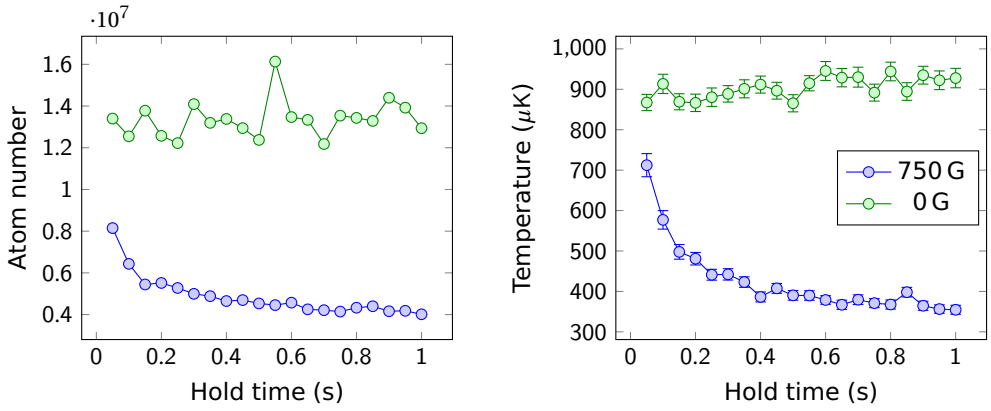

Figure 3.33: Plain evaporation in an optical dipole trap of 3 mK depth

the theoretical limit for Doppler cooling. A possible explanation for the higher temperatures in the optical dipole trap is the fluctuation dipole force heating caused by the large differential ac Stark shift on the order of 20 MHz between the $|2^2S_{1/2}\rangle$ and $|2^2P_{3/2}\rangle$ states.

Depending on the exact parameters and the alignment of the magneto-optical trap $1/e$ lifetimes of up to 8 min have been measured.

Due to the non-resolved $|2^2P_{3/2}\rangle$ excited state hyperfine structure conventional sub-doppler cooling techniques like polarization gradient cooling [57] are *not* expected to work for lithium and have not been demonstrated experimentally. Polarization gradient cooling would require a differential ac Stark shift for the different m_F states in $|2^2S_{1/2}\rangle$ ground state. Recent demonstrations of gray molasses cooling [154, 155], Sisyphus cooling [156], and cooling on the ultra-violet $|2^2S\rangle \rightarrow |3^2P\rangle$ transition [157] show ways to circumvent this limitation and potentially increase the atom number in the optical dipole trap.

3.4.4 Initial Optical Evaporation

After the initial laser cooling we are left with $\sim 10^7$ atoms in an optical trap with a Gaussian beam waist is $w_0 = 54$ um created by focusing a 255 W broadband 1070 nm fiber laser (see 3.2.3, 3.3.7, 3.4.4). Although the temperature of the atoms is already three times less than the theoretical trap depth of 3.3 mK, the phase-space density (see equation (1.52)) can be increased five-fold by just holding the atoms in the trap at a constant trap depth.

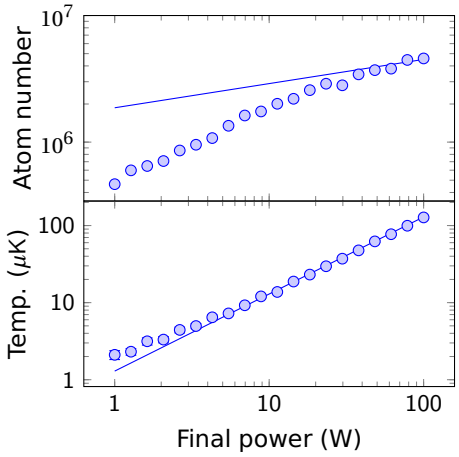

Figure 3.34: Atom number and temperature during the optical evaporation in the main chamber. The solid lines are calculations based on Luo et al.[159]

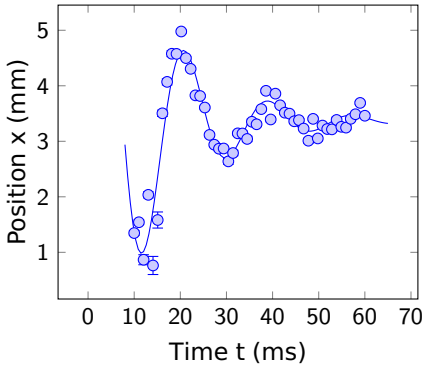

Figure 3.35: Center of mass oscillations of the atomic cloud in the optical dipole trap

Collisions inside the trap occasionally produces high energy atoms that then leave the trap and reduce average the temperature of the remaining atoms. This process is called *plain evaporation* [158]. For ^{6}Li atoms the collision rate can be significantly increased by the increased the interparticle scattering length a near the Feshbach resonance. Figure 3.33 shows the enhanced evaporation at 750 G ($a = 3500a_0$) compared to 0 G ($a = -13a_0$).

In the actual experiment we do not perform plain evaporation to minimize the time that the science chamber downstream of the dipole trap is exposed to high laser powers, but instead we immediately start forced evaporation after 5 ms. This has no significant effect on the atom number.

Forced evaporation is a process where the hottest atoms actively get removed from the system. In our experiment this is done by continuously lowering the trap depth. In comparison to evaporative cooling in a magnetic trap using a radio-frequency knife [160], reducing the laser power for optical evaporation also reduces the trap frequencies and thus the scattering rate. This is merely a problem, because typically the trap frequencies in optical traps, especially in a crossed optical dipole trap, are higher than in magnetic traps, leading to a faster evaporation. In the main chamber, however, we only use a single beam optical

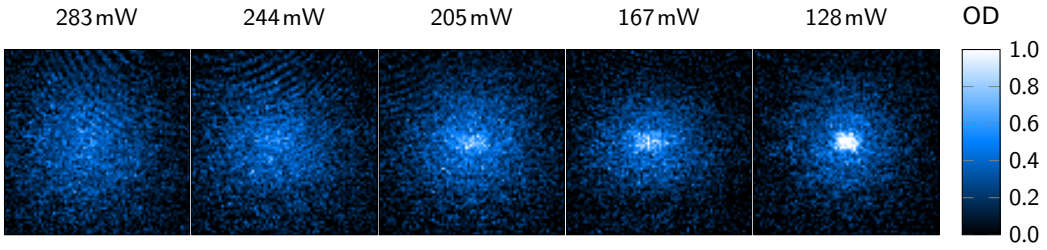

Figure 3.36: Emergence of a molecular Bose-Einstein condensate by forced evaporation in a single-beam optical dipole trap at after 11.2 ms of time of flight

dipole trap with a large aspect ratio of 225.

The laser intensity is ramped down over time using the temporal profile given in [161, 162, 159] for evaporation in the unitary limit

$$P(t) = P_0 \left(1 - \frac{t}{\tau}\right)^{2(\eta'-3)/(\eta'-6)} \tag{3.14}$$

with $P_0 = 255\,\mathrm{W}$, $\tau = 5\,\mathrm{s}$, $\eta' = \eta + (\eta - 5)/(\eta - 4)$, and $\eta = 10$. For this scaling law it is assumed that the ratio of temperature and trap depth $\eta = U(t)/(k_\mathrm{B}T(t))$ remains constant. O'Hara et al. [162] mention that a ratio of 10 is a typical value for harmonic traps. This seems to be a good approximation since in our system the ratio during plain evaporation (figure 3.33) approaches this value.

During our evaporation this ratio stays constant up to low trap depths, although the reduction in atom number is higher than expect from the scaling laws [159]. At low temperatures molecule formation should start to play a role since the binding energy at the given magnetic field is on the order of 2.4 μK [163].

The coils around the main chamber were initially designed as a quadrupole trap and then reconfigured as separate coils for the magneto-optical trap and Feshbach coils [100]. This causes the Feshbach field to be inhomogeneous. At a field of 750 G the Feshbach coil produces about 35 Hz or transverse confinement and 50 Hz of deconfinement in the axial/vertical direction.

This can be used to evaporate in a single beam optical dipole trap to quantum degeneracy. We have successfully created a Bose-Einstein condensate of Li_2 Feshbach molecules in

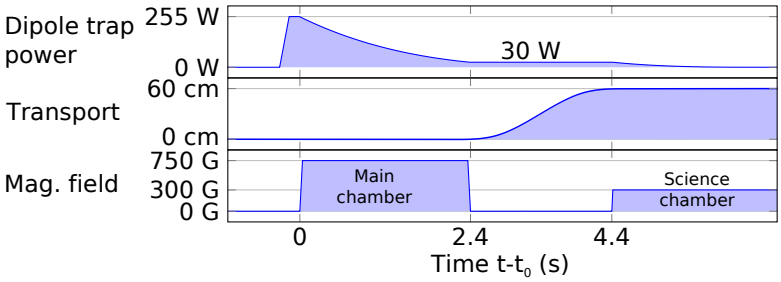

Figure 3.37: Experiment sequence of the all optical transport

this trap geometry. The smoking gun of the condensation is the emergence of the zero-momentum peak in time-of-flight images (figure 3.36). Before the release from the trap the intermolecular interaction was reduced by switching of the magnetic field and then quickly ramped up again during the last milliseconds of the time of flight. This way the momentum distribution does not get altered by interaction and shows the condensation into the zero-momentum state. Since this was only done to qualitatively test our evaporation, there is not exact atom number or temperature measurement, but estimated to have on the order of 10,000 molecules at a temperature of about 100 nK.

The trap frequency is determined by offsetting the trap minimum slightly during loading and exciting center of mass oscillations in the longitudinal direction. From the oscillation frequency ω and the damping coefficient λ of the fit function $x(t) = x_0 + x' \cos(\omega t + t_0) \exp(-\lambda t)$ one can extract the trap frequency for the undamped case

$$\omega_0 = \sqrt{\omega^2 + \lambda^2}.$$

For a given laser power it is possible to calculate the Gaussian beam waist from equation (1.80). The measurement in figure 3.35 indicates that Gaussian beam waist is $w_0 = 54.1(5)\,\mu\text{m}$. Note that this is ignoring systematic effects from the anharmonicity of the trap. To determine the trap frequency more accurately one would need to vary the initial displacement and extrapolate to small displacements.

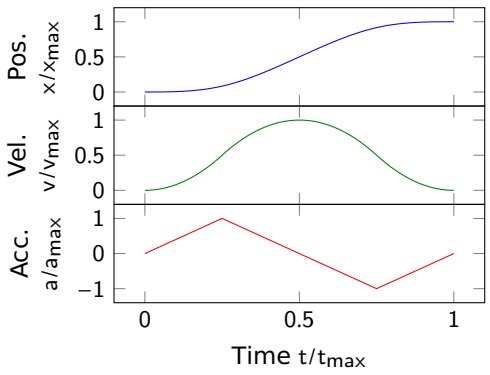

Figure 3.38: Position, velocity, and acceleration during the optical transport

3.4.5 All-optical Transport

After the first evaporation in the main chamber down to 30 W of laser power the atoms are at a temperature of about 40 µK. The final atom number after a second evaporation is independent of the transport power over a large range of parameters.

The transport over ∼60 cm into the science chamber is performed by slowly moving the focus of the optical dipole trap by translating the focusing lens [100]. The position of the atoms follows a "constant-jerk" profile where the acceleration is ramped piecewise-linearly in time yielding a piecewise quartic profile in position. For a transport over distance $x_{\max}$ in the time $t_{\max}$ the maximum required acceleration is $a_{\max} = 8x_{\max}/t_{\max}^2$ and the maximum velocity is $v_{\max} = 2x_{\max}/t_{\max}$. The jerk $\dot{a}(t)$ during the constant acceleration is $|\dot{a}| = 32x_{\max}/t_{\max}^3$. During the first half of the one-way transport the position is given by

$$x(t) = \begin{cases} 0 & t \leq 0 \\ \frac{2}{3}\frac{a_{\max}}{t_{\max}}t^3 & 0 < t \leq \frac{t_{\max}}{4} \\ a_{\max}\left(-\frac{4}{t_{\max}}t^3 + t^2 - \frac{3}{2}t_{\max}t + t_{\max}^2\right) & \frac{t_{\max}}{4} < t \leq \frac{t_{\max}}{2} \end{cases} . \tag{3.15}$$

The whole profile is visualized in figure 3.38.

At the transport power of 30 W we do not observe any heating or atom loss. Heating rate in figure 3.39 can be explained solely by the heating caused by the residual intensity noise on the trapping laser (3.2.3.3). The large spread of temperatures in the plot is attributed to

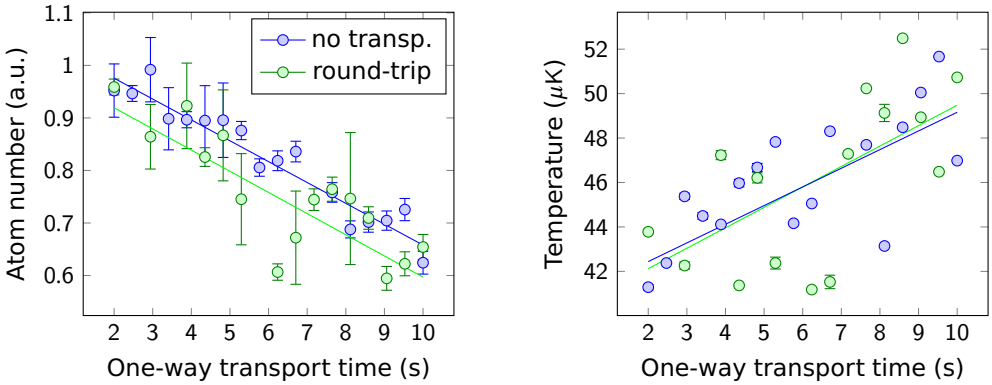

Figure 3.39: Transport heating for round-trip transport over 60 cm per leg

the poor image quality at zero-field imaging.

During the transport the high-power beam is aligned such that it exits the glass cell at the center. This leaves the atoms about 10 mm below the super-polished substrate at the end of the horizontal transport. In the next step the atoms are transported up vertically by tilting the dipole trap beam via the mirror M2 in figure 3.3.7 with a PIEZOSYSTEMS JENA MICI 200 SG amplified piezo. The vertical translation gain near the substrate is roughly $2 \ldots 4\,\mu\mathrm{m}/\mathrm{mV}$.

At this point the cloud is still very elongated along the direction of the laser and cannot be transported all the way up to its final position near the surface. It is evaporated further a few 100 µm away from the substrate before it is moved closer for the loading of the accordion lattice (3.4.7).

3.4.6 Final Optical Evaporation

The optical dipole trap is overlapped with a secondary dipole trap (see 3.3.5) formed by a 785 nm incoherent beam with 0.5 W of power and a Gaussian beam waist of 28 µm. This trap should theoretically be 55 µK deep, so that all atoms should "fall" into this trap right after the transport. But compared to the high-power dipole trap alone the volume is smaller so that it only becomes visible after further evaporation, hence the name "big dimple" trap.

For alignment purposes mirror M1 in figure 3.3.7 is equipped with two NEWFOCUS PICOMOTORS. Although we cannot move them in real-time, they are a valuable tools to do

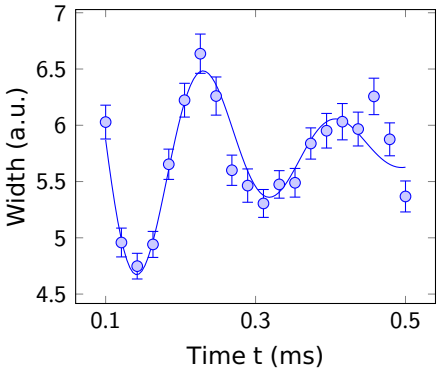

Figure 3.40: Oscillations of the cloud size after a quench of the trap depth of the "big dimple"

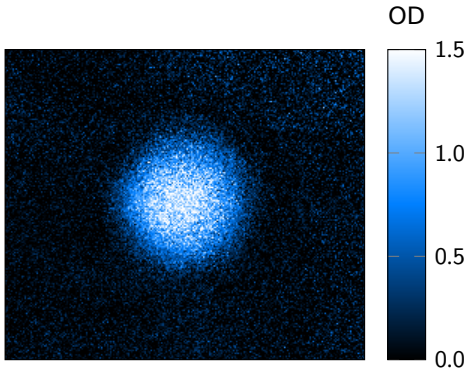

Figure 3.41: Degenerate Fermi gas of $N \sim 30000$ atoms at a temperature $T/T_F \sim 0.2$ after 0.87 ms time-of-flight

the fine alignment to overlap the high-power optical dipole trap (3.3.7) with the "big dimple" (3.3.5).

The trap frequency was measured by rapidly changing the trap depth to excite quadrupole oscillation/breathing mode oscillations in the direction of the high power dipole trap. This was done for several different powers and the waist was extracted with a fit to the theoretical curve. The oscillation frequency of the breathing mode is twice the trap frequency, since the spatial extent is identical when both sides of the cloud change sides in half an oscillation period.

The evaporation in the science chamber is again sped up by enhancing the interparticle scattering length near a Feshbach resonance. To avoid molecule formation the evaporation in the science chamber is performed on the attractive side of the Feshbach resonance near $B = 300\,\mathrm{G}$. The scattering length at this field is $a = -280\,a_0$. Although the scattering length is smaller than on the repulsive side, the evaporation can be extremely fast due to the high trap frequencies one the order of a kilohertz in the crossed optical dipole trap. In this trap configuration we successfully created a quantum degenerate Fermi gas with ∼30,000 atoms at a temperature of about $T = 0.2T_F$ (see 3.41).

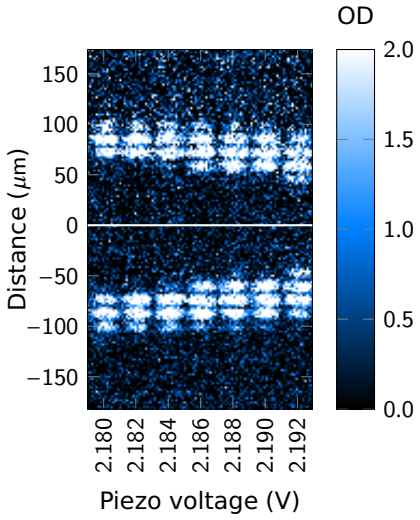

Figure 3.42: Loading the accordion lattice at 2° for different positions of the optical dipole trap. The atoms in the upper half are mirror images (see 3.19).

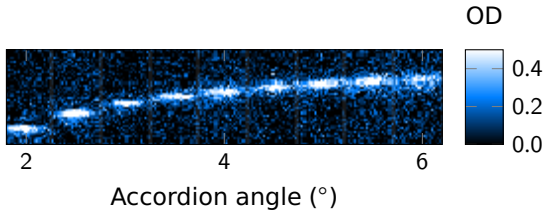

Figure 3.43: Atoms in the accordion lattice during the compression

3.4.7 Accordion Lattice Compression

It is geometrically not possible to position our high-power optical dipole trap closer than $\sim w_0$ under the substrate. In the experiment the atoms get transported in the optical dipole trap up to a distance of about 84 µm from the substrate before being loaded into the accordion lattice (see 3.3.4), a standing wave created by the reflection of a 1064 nm, 20 W laser beam with a Gaussian beam waist $w_0 = 290\,\mu\text{m}$ (see 3.2.5). The optical accordion simultaneously transports the atoms to their final distance of ∼10 µm and compresses the cloud. The transport is achieved by continuously increasing the angle of incidence from gracing incidence at 2° to 20°.

The distance is a multiple of the lattice spacing (1.91) and given by

$$d_n(\theta) = (n + \frac{1}{2})\frac{\lambda}{2\,|\sin\theta|} \tag{3.16}$$

for the nth "pancake" (starting with 0). The evolution of the lattice potential for the varying angles can be seen in figure 3.44. In the experiment we load into the fifth pancake which

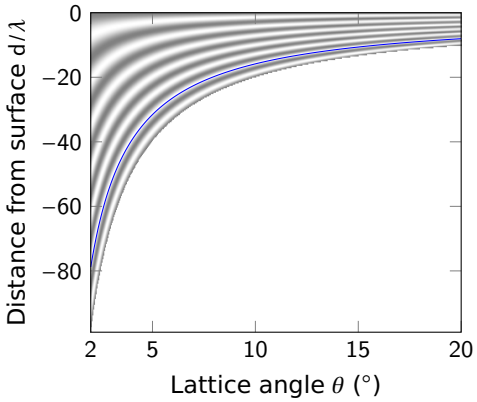

Figure 3.44: Lattice potential for the first seven sites during the accordion compression. The solid blue line is the actual trajectory in the experiment.

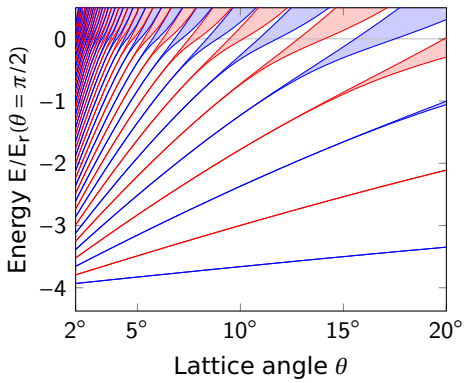

Figure 3.45: Evolution of the band structure during the accordion compression for a lattice depth of $4E_r(\theta = \pi/2)$.

trajectory is plotted in blue.

In the limit where the distance is small compared to the Gaussian beam waist we get full interference contrast for all angles. This, in turn, implies that the absolute lattice depth stays constant during the compression, while the trap frequency (1.93) and lattice recoil energy E_r (1.94) increase. Since the number of bound states decreases there is also forced evaporation during the compression (figure 3.45).

For shallow angles and realistic parameters this assumption is not justified (figure 3.17). The interference contrast away from the center gets reduced by the fact that the two interfering fields stem from the wings of the Gaussian beam. The potential depth z away from the substrate is reduced by

$$\frac{V}{V_{\max}} = \exp\left(-\frac{2\cos^2\theta}{1+\frac{z^2\lambda^2\sin^2\theta}{\pi^2 w_0^4}}\frac{z^2}{w_0^2}\right). \tag{3.17}$$

Therefore to efficiently load atoms into a shallow angle accordion lattice the waist has to be at least on the order of the distance to the mirror surface.

To smoothly transport the atoms without heating the distance is ramped with a tanh

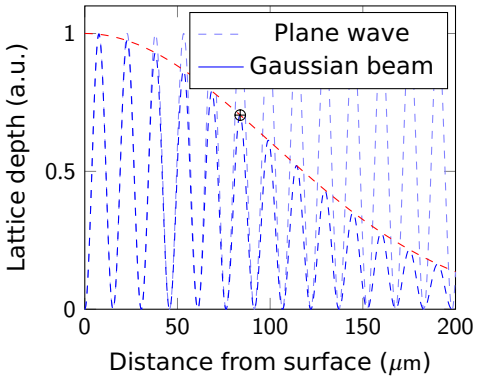

Figure 3.46: Reduction of the interference contrast away from the substrate for a wavelength of 1064 nm and a Gaussian beam waist of 200 μm. The fifth pancake is indicated by $\oplus$.

function, so that the control signal for the galvo controlling the tilt is given by

$$\theta(t) = \arcsin \frac{1}{c_0 + c_1 \tanh\left(c_2(t - t_r/2)\right)} \tag{3.18}$$

with the initial angle θ_0, the final angle θ_1, the ramp duration t_r, and the constants $c_0 = (1/\sin\theta_0 + 1/\sin\theta_1)/2$, $c_1 = (1/\sin\theta_0 + 1/\sin\theta_1)/\tanh(c_2 t_r)/2$, $c_2 = (1/\alpha^2 - 1)/t_r$, $\alpha = 1/2$.

Chapter 4

Experiment Control And Analysis Software

Our experiment control software, Blastia [100], is tailored to interface with the home-built FPGA-based Spectron hardware. The diagram 4.1 gives a brief overview how the software written in C# interacts with the Spectron hardware, as well as other non-Spectron hardware like a camera. In the following paragraphs I will elaborate on some of the concepts and technical details of our experiment control.

A single experimental run (capture atoms, cool, then image) is called a *shot*. A set of shots, where typically one or more parameters are varied, is called a *scan*. Each shot is a collection of *ramps*.

A ramp defines how a real number changes over time and is composed of piecewise linear ramp sections. This could control anything from a frequency generated by the Symphonia direct digital synthesizer boards to an analog voltage output by the Spectron digital-to-analog converter. Besides ramping real numbers a second kind of ramp controls logic/Boolean signals, like enabling or disabling the radio frequency output of the synthesizer. The ramps are regenerated every shot and can be parameterized using variables. In addition to real numbers (including units) and Boolean values, the experiment control system supports C-style enumerations (for example to switch between different coil configu-

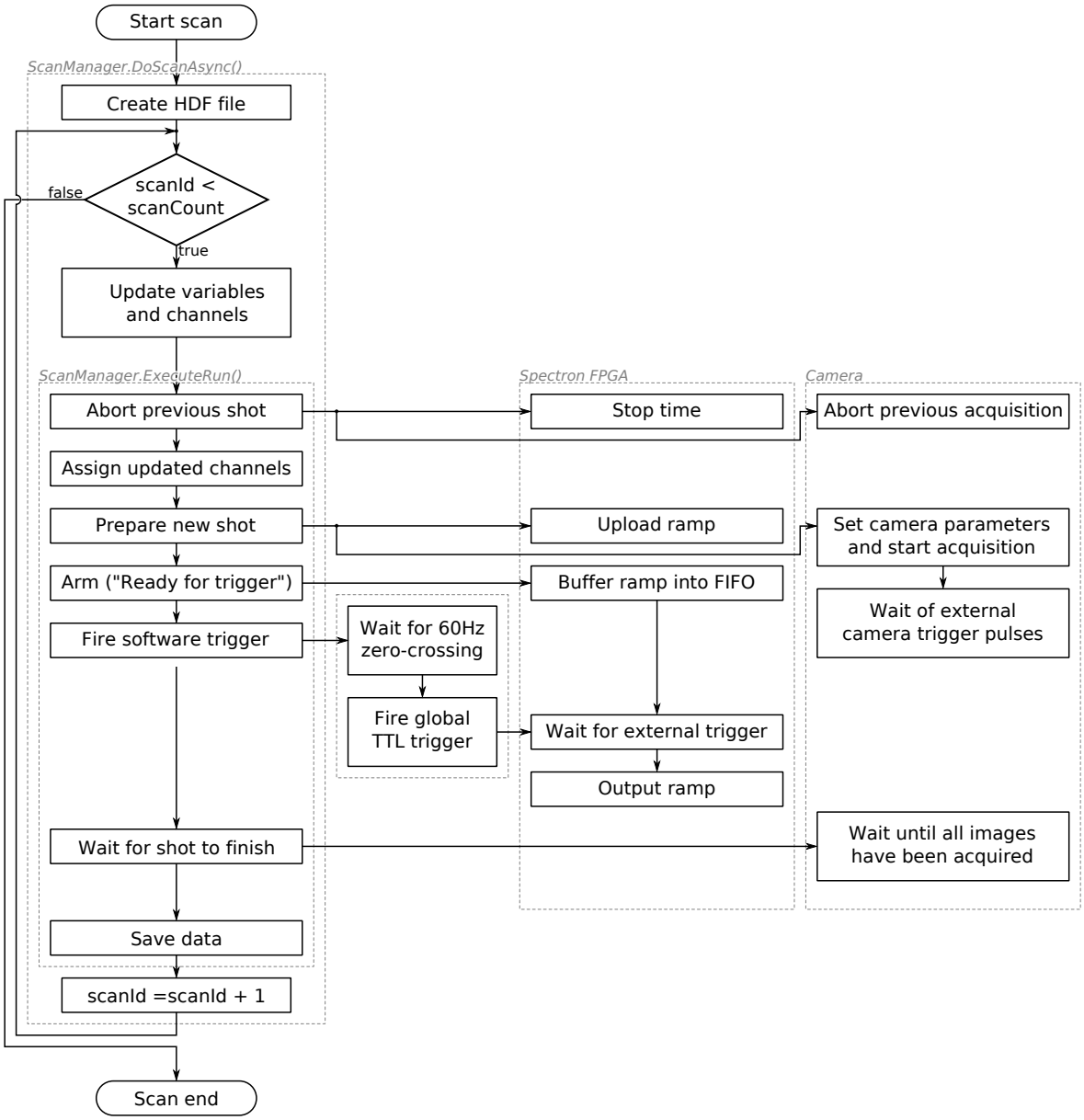

Figure 4.1: Simplified flow chart of a scan including the experiment control software and hardware

rations) and strings channels, although those have to be mapped to real ramps and Boolean pulse sequences before the ramp gets uploaded onto the FPGAs.

Before the start of each shot the ramps are uploaded onto the Spectron hardware via Ethernet connection using the Spectron Datagram Protocol SDP [100]. Since SDP is based on the User Datagram Protocol UDP [164] it is not guaranteed that the ramp was received correctly. For that purpose each hardware board returns another packet every time it receives a memory block. Should the transmission fail the memory block is sent again.

After that the hardware is asynchronously "armed" and is then waiting for an external trigger pulse. This state is called "Ready For Trigger". Once all ramps are successfully uploaded and all hardware is armed, a (internal) trigger of a particular device is initiated asynchronously in software. This device waits for the next zero-crossing of the 110 V/60 Hz line voltage and then creates a global TTL pulse sent to the external trigger of all devices that are part of the experiment. This pulse will start the output of the ramps. Any further trigger pulses are ignored until the sequence is aborted and all devices are armed again. The "abort" step necessary because there is no way for the hardware to know when a shot is completed.

Phase-locking the experiment to the line frequency has the advantage that 60 Hz noise created by various devices in the building are more or less the same from shot to shot. In the future it could be necessary to re-synchronize to the line frequency a second time during a shot, so that, for example, changing the experiment timing in the beginning of the sequence does not affect the absolute phase of the line at a later point. This is supported by a special channel called "GlobalPause": all outputs are held constant until the system receives another trigger.

4.1 Long Pulse Sequences: Burst Mode

The custom-built experiment control hardware has two major electronic boards, the Spectron Symphonia four-channel 1–400 MHz direct digital radio frequency synthesizer and the general purpose Spectron "Spy" boards with digital and analog daughter boards.

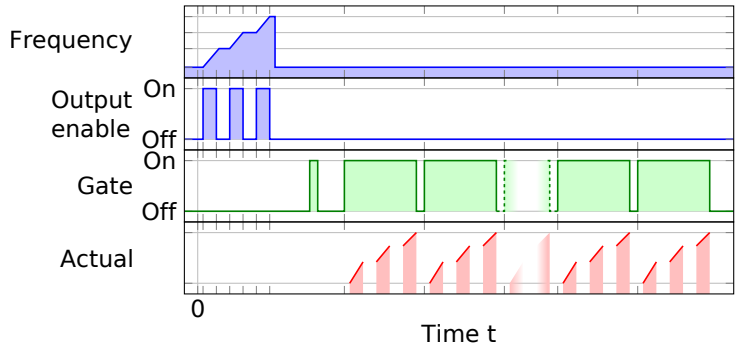

Figure 4.2: Example of a chirped pulse train using the burst mode described in the text

The available memory on the FPGA boards is limited by the size of the SRAM on the Dallas Logic modules. Its total capacity is 2048 so-called *quarter blocks*. Each quarter block can contain 64 entries (time stamp, value, and ramp rate, see [100]). The memory is shared amongst all "virtual" devices on a Spectron board, so that the number of chirped pulses for Raman imaging is limited to about 1500. On Symphonia boards the frequency channel (24 bits) and the radio frequency enable channel (amongst a few other logic functions, 8 bits total) are sharing a ramp table. Therefore a change in either frequency or the radio frequency enable will create a new entry in the ramp table (unless they happen simultaneously). On Spectron boards typically 32 Boolean channels are bundled into one ramp table. Again, a change in any of those channels will require a full entry in the ramp table and thus limit the number of maximum pulses that can be generated.

To circumvent this limitation we implemented burst mode: a ramp is programmed starting from $t = 0\,\mathrm{s}$, then later during the shot this ramp is spooled every time there is a rising edge on a separate "gate" channel. On the lowering edge of the gate pulse the ramps gets stopped and the FIFO buffer is filled again with the first block of the ramp table. Because of that double buffering one needs to allow for a sufficiently long time before the next trigger (on the order of $10\,\mu\mathrm{s}$).

In detail, the burst mode is implemented by intercepting the global signals (like timestamp, trigger, and abort) and creating a "local" time for the channel in burst mode, called the MicroTimeGenerator. It requires one "dummy" pulse on the gate channel to buffer the

FIFO for the first time on the falling edge of that pulse. An example sequence is depicted in figure 4.2, where the output of a Symphonia synthesizer is chirped in three pulses.

4.2 Python Data Analysis Framework

At the beginning of each shot all data required to reproduce it at a later time is saved into an HDF file [165]. The file includes all variables used to calculate the ramp forms as well as the ramps themselves. In addition, the source code for the ramp generation is saved into a separate ZIP file. At the end of each experimental run images are retrieved from the cameras and are then also added to the HDF file.

The Spectron and Symphonia boards both feature a software oscilloscope that can store 2048 8 bit values per channel in the FPGA's memory. The source of a channel can be an external analog-to-digital converter or any FPGA register for debugging purposes. The software oscilloscope is used to monitor various laser powers and currents in the magnetic field coils in the experiment. These data are saved in the HDF file after it is downloaded from the FPGAs via SDP communication.

For diagnostic purposes the software scope traces are analyzed by the C# experiment control software and values like maximum coil current or laser power for the magneto-optical trap are saved to the HDF file as well.

The structure of the resulting HDF file is shown in figure 4.3. Additional data are saved as attributes of the individual HDF groups and datasets, for example imaging parameters like exposure time and camera temperature are saved as attributes of each individual image.

Each HDF file can also contain Python source code that performs analysis of the scan it is a part of. The analysis software framework called Plastia makes extensive use of the NumPy and SciPy libraries [166], as well as MatplotLib [167] for plotting. Besides many wrapper classes (see 4.4) to simplify accessing the data in the HDF format, implement Blastia's unit system, and simplify non-linear fitting problems, it also features a platform independent graphical user interface. We have libraries to simplify the analysis, for example to automatically identify individual atoms in the fluoresence images via blob-detection and

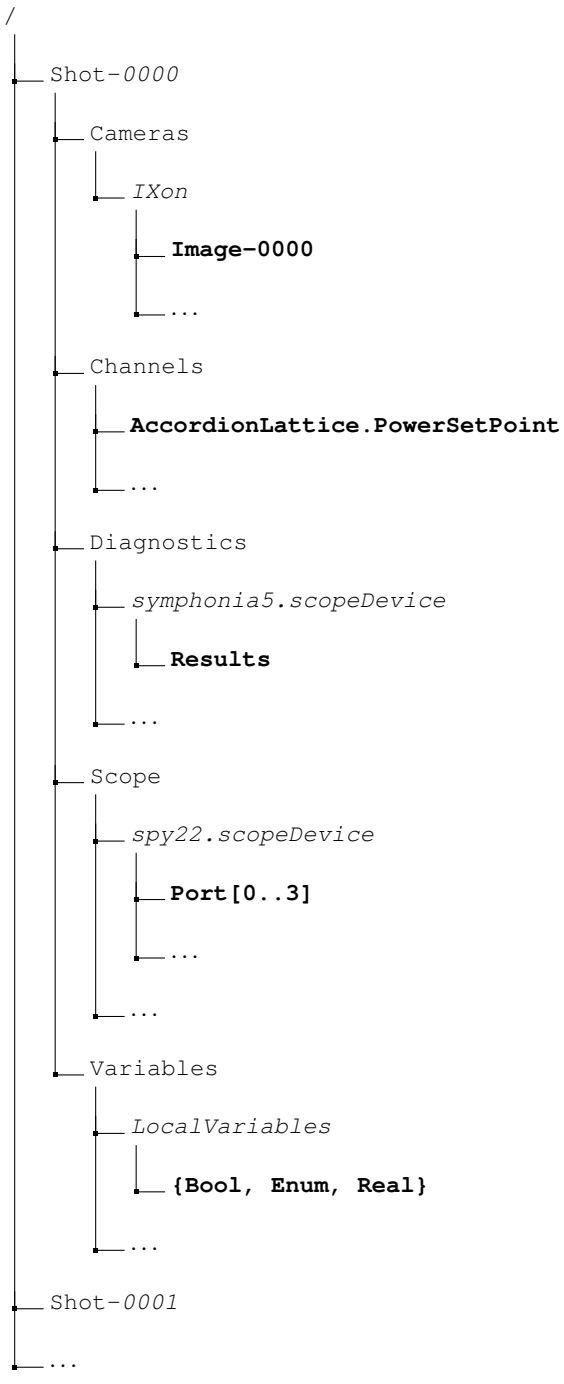

Figure 4.3: Structure of the experiment data saved to an HDF file

then fit a lattice to their positions.

The source code within the HDF file is separated into for blocks: Preamble for loading libraries and defining variables, a block that is executed for each shot (e.g. fit absorption imaging images), a block that is executed afterwards, for example, in lifetime measurements to fit an exponential decay to the atom number calculated in the previous step, and finally a postamble to plot the results and print a table with the results.

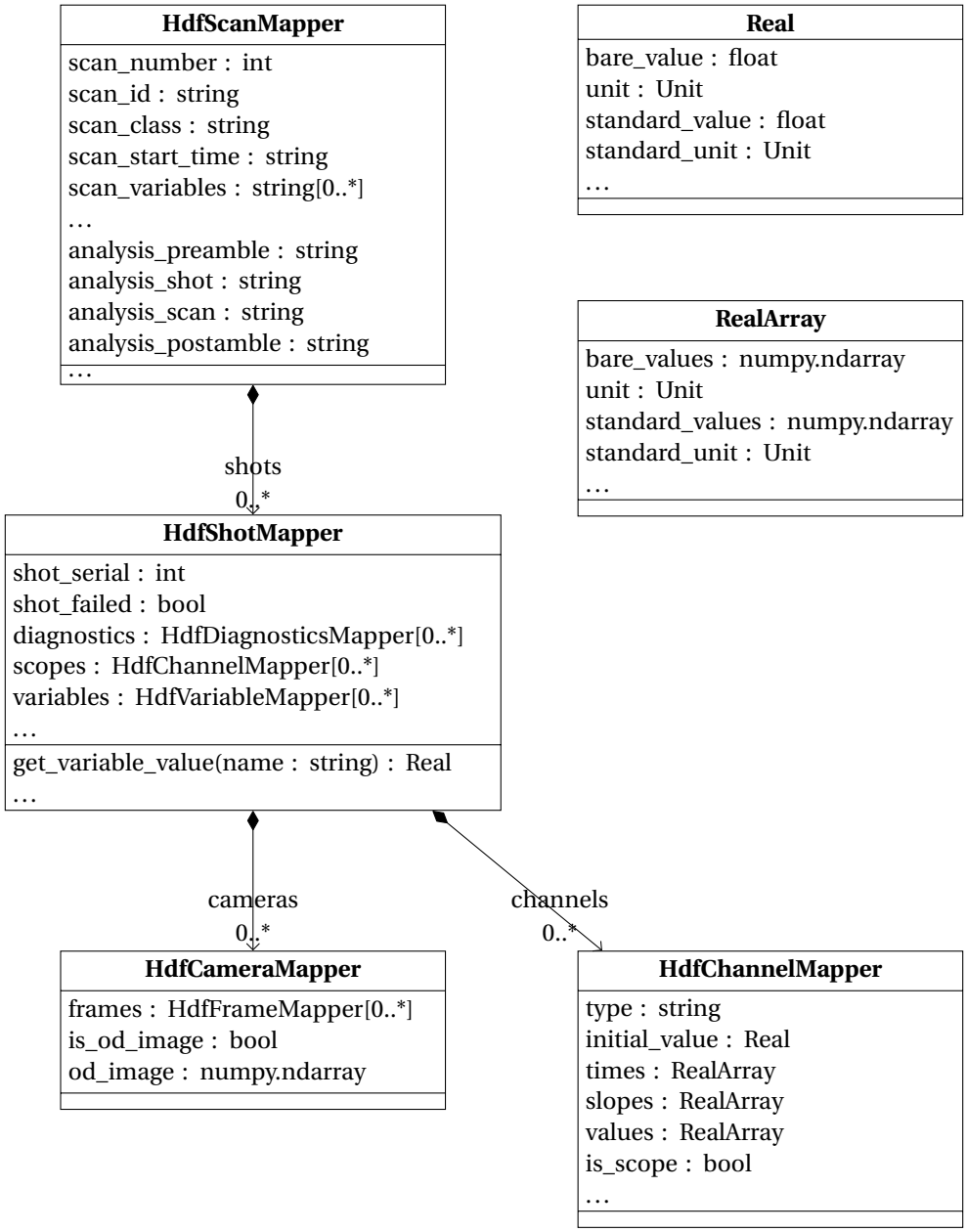

Figure 4.4: Simplified diagram of some of the wrapper classes for the analysis

Chapter 5

Outlook

5.1 The Temperature Problem

Even at room temperature the electrons in a conductor are highly quantum-degenerate with a

$$\left(\frac{T}{T_F}\right)_{el} \sim 0.004.$$

The lowest temperatures achieved sofar with ultracold fermions in an optical lattice is only [110]

$$\left(\frac{T}{T_F}\right)_{lat} \sim 0.15.$$

To observe magnetic ordering

$$\left(\frac{T}{T_F}\right)_{Neel} \lesssim 0.04$$

is required [168].

Possible solutions to this problems include starting with a extremly low spin-entropy state like a Mott insulator of a Bose-Einstein condensate of Li_2 molecules or a fermionic band insulator. Then the number of lattice sites have to be doubled to obtain half-filling. We are setup to do so by letting our two radial lattices interfere. Controlling the relative phase between the two axes allows us to adiabatically transform the lattice (see 1.17).

Serwane et al. [148] have reported low entropies for a few-particle system with a

technique similar to the Band insulator mentioned above in a single trap. Bernier et al. proposed a scheme to evaporate within an optical lattice [169] that requires projection of repulsive and attractive potentials, which would be easy to implement even with our existing hardware.

A completely different path could be to not encode the spin in the hyperfine states but rather in a 2×2 plaquette, as proposed by Rey et al. [170].

5.2 Digital Quantum Simulation

Another interesting direction would be to perform *digital simulation* [171] with our experimental setup. With digital quantum simulation Hamiltonians that have no direct mapping to the actual system can be simulated. The time evolution of a Hamiltonian can be done iteratively in small time slices (similar to numerical integration). For a Hamiltonian $\hat{H} = \sum_{i=1}^{s} \hat{H}_i$ the so called the *Trotter expansion* [172, 173] reads:

$$\exp(-i\hat{H}t) = \lim_{m\to\infty} \left(\exp\left(-i\hat{H}_1 \frac{t}{m}\right) \exp\left(-i\hat{H}_2 \frac{t}{m}\right) \ldots \exp\left(-i\hat{H}_s \frac{t}{m}\right) \right). \qquad (5.1)$$

For large m the sub-Hamiltonians commute approximately: $[\hat{H}_i, \hat{H}_j] \approx 0$. At each time step of duration $\Delta t = t/m$, the time evolution under the sub-Hamiltonian $\hat{H}_i$ can be simulated as a series of one- and two-qubit gates. The minimal requirement for the quantum system used as a universal simulator is that it must be possible to perform single qubit rotations around two directions and one universal two-qubit gate [174] (for example CNOT [175]). The simulation can be more efficient if parts of the sub-Hamiltonians are intrinsic to the simulating quantum system, but this is not a requirement since every Hamiltonian can be stroboscopically simulated by single and two-qubit operations.

5.2.1 Single Qubit Gates

Global qubit rotations can be performed using microwave transitions between the $|1\rangle$ and $|2\rangle$ states at large magnetic fields. In the large magnetic field regime ($B \gg h \cdot 228\,\mathrm{MHz}/\mu_\mathrm{B} = 163\,\mathrm{G}$, see 1.1.1) the transition frequency is insensitive to the field value (and therefore

magnetic field gradients). The three lowest magnetic fields shift by the same amount, leaving the differences constant.

Single qubit rotations require precise optical addressing (for example with a digital micro-mirror device [176]) or high magnetic field gradients [177]. The latter would require the addition of a substantially sized coil to the experiment. It would need to be able to create a gradient that causes a differential Zeeman shift between neighboring lattice sites greater than the desired Rabi frequency:

$$\hbar\Omega \ll \mu_{\mathrm{B}} \frac{\partial B}{\partial x} d_{\mathrm{lat}}.$$

A $2\pi \cdot 1\,\mathrm{MHz}$ Rabi frequency would require a gradient of $\sim 2\,\mathrm{kG/cm}$.

For optical addressing one can focus two Raman beams onto a single lattice site. Since Raman transitions are a two-photon process that is sensitive to the square of the laser intensity (see equation (2.9)) the spot size is effectively reduced by a factor of $1/\sqrt{2}$. Alternatively, one can reduce crosstalk between neighboring sites by ac Stark shifting one lattice site with a focused detuned laser beam and then selectively driving microwave transitions between the shifted states [37]. The ac Stark shift is also caused by a two-photon process and hence the same increase in optical resolution applies here. Both addressing schemes would even allow to manipulate multiple qubits at once if a pattern is projected instead of a single beam.

5.2.2 Two-Qubit Gate

Looking at the Heisenberg interaction introduced in 1.5.4.1 with a time dependent superexchange coupling $J(t)$

$$\hat{H}_J^{(2)} = J(t)\hat{\mathbf{S}}_{\mathrm{L}} \cdot \hat{\mathbf{S}}_{\mathrm{R}},$$

we can introduce a propagator assuming a constant coupling $J(t) = J$ while $\hat{H}_j^{(2)}$ is applied

$$U_J(\theta) = \exp\left(-i\theta J \hat{\mathbf{S}}_{\mathrm{L}} \cdot \hat{\mathbf{S}}_{\mathrm{R}}\right).$$

The coupling can be controlled by instantaneously changing the lattice depth to a larger (no tunneling, $J = 0$) or lower (tunneling, $J > 0$) value. By applying a large tunneling for a time τ the system evolves according to $U_j(\theta = \hbar J\tau)$.

There are two interesting cases of the propagator. On the one hand for a time such that $\theta = \pi$, the two atoms exchange their position according to

$$U_J(\pi) \propto \begin{array}{c} \\ \downarrow\downarrow \\ \downarrow\uparrow \\ \uparrow\downarrow \\ \uparrow\uparrow \end{array} \begin{array}{c} \begin{array}{cccc} \downarrow\downarrow & \downarrow\uparrow & \uparrow\downarrow & \uparrow\uparrow \end{array} \\ \begin{pmatrix} 1 & 0 & 0 & 0 \\ 0 & 0 & 1 & 0 \\ 0 & 1 & 0 & 0 \\ 0 & 0 & 0 & 1 \end{pmatrix} \end{array}. \tag{5.2}$$

This operation, called a SWAP gate, swaps the two atoms, but does not create entanglement between the two sites.

On the other hand, applying a $\pi/2$ pulse will create a superposition if the spins on the two sites were initially different ($|\uparrow\downarrow\rangle \rightarrow \frac{1}{\sqrt{2}}\left(|\uparrow\downarrow\rangle - i\,|\downarrow\uparrow\rangle\right)$). This so-called $\sqrt{\text{SWAP}}$ gate can be represented in matrix form as

$$U_J(\pi/2) = \begin{array}{c} \\ \downarrow\downarrow \\ \downarrow\uparrow \\ \uparrow\downarrow \\ \uparrow\uparrow \end{array} \begin{array}{c} \begin{array}{cccc} \downarrow\downarrow & \downarrow\uparrow & \uparrow\downarrow & \uparrow\uparrow \end{array} \\ \begin{pmatrix} 1 & 0 & 0 & 0 \\ 0 & \frac{1}{2}(1-i) & \frac{1}{2}(1+i) & 0 \\ 0 & \frac{1}{2}(1+i) & \frac{1}{2}(1-i) & 0 \\ 0 & 0 & 0 & 1 \end{pmatrix} \end{array}. \tag{5.3}$$

In thus description fermionic neutral atoms coupled via the superexchange interaction are equivalent to coupled solid-state quantum dots, another workhorse for quantum information processing.

To implement the $\sqrt{\text{SWAP}}$ gate it would be helpful if all lattice sites could be grouped into independent double wells. Double wells could be either created by overlapping the existing optical lattice with a second lattice with twice the spacing or by letting the two existing horizontal lattice interfere. By controlling the relative phase, a double-well structure

could be created (see 1.4.3.2). Alternatively, in the vertical direction we already have a double well when the additional vertical lattice beam is turned on.

Here I briefly sketched a path to use our system as a universal digital quantum simulator, but it is going to take a substantial amount of engineering to create a system with many qubits and fidelities comparable to existing trapped ion quantum simulators [178]. The benefit would be that it should be easier to scale our system to with hundreds or more qubits.

5.3 Multi-Species And Molecular Quantum Gas Microscope

Initially we considered to image the atoms in the optical lattice in a different way. Instead of continuously cooling the atoms during imaging, we proposed a rastered readout scheme, where one atom at a time gets ionized by a tightly focused ultraviolet beam (and potentially a second less focused infrared beam) to ionize the ^{6}Li atom via the $2s \rightarrow 3p \rightarrow \infty$ transition. The ion and the electrons are accelerated in a static electric field and detected in two electron multipliers (Dr. Sjuts KBL5RS) [100]. High-fidelity detection using fragment correlation has been shown for a single ^{87}Rb atom in an optical dipole trap [179].

This scheme can easily be extended to multiple species and even molecules by analyzing the arrival times of the ions similar to a time-of-flight mass spectrometer.

5.4 Conclusion

In this thesis I presented the first site-resolved images of ultracold lithium in an optical lattice. The successful extension and further development of quantum gas microscopy [35, 36] to a fermionic species will enable us to study different classes of condensed matter models. The ability to individually probe and manipulate the constituents of quantum many-body systems with single-site resolutions is an integral ingredient for understanding spatial correlations in those systems.

Due to their light mass, lithium atoms have the advantage of fast dynamics in the

strongly-correlated regime. However, the use of lithium presented challenges that compelled us to develop a novel application of Raman sideband cooling. This application of Raman sideband cooling in deep optical lattices has allowed us to scatter a sufficient number of photons to image individual atoms.

While this newly developed technique is a significant advance in studying quantum many-body systems, the approach is not fully developed. Presently, cooling both during the imaging and before the lattice loading needs to improved further before our system can realistically be used experiments exploring strongly-correlated physics. These opportunities for optimization will minimize tunneling during florescence imaging and allow us to detect magnetic ordering, the first step towards studying the Fermi-Hubbard model.

Whatever direction our experiment is going to take in the future, whether quantum simulation, quantum information processing, or the creation of new states of quantum matter, I am certain that the site-resolved imaging of atoms will be an important part of it.

References

[1] Chin, C, Julienne, P, & Tiesinga, E. Feshbach resonances in ultracold gases. *Rev. Mod. Phys.*, **82**(2):1225. doi: 10.1103/RevModPhys.82.1225 (2010). 18, 19

[2] Wikipedia. Observable Universe — Wikipedia, The Free Encyclopedia (2014). 1

[3] Metropolis, N, Rosenbluth, AW, Rosenbluth, MN, Teller, AH, & Teller, E. Equation of State Calculations by Fast Computing Machines. *J. Chem. Phys.*, **21**(6):1087. doi: 10.1063/1.1699114 (1953). 2

[4] Troyer, M & Wiese, UJ. Computational Complexity and Fundamental Limitations to Fermionic Quantum Monte Carlo Simulations. *Phys. Rev. Lett.*, **94**(17):170201. doi: 10.1103/PhysRevLett.94.170201 (2005). 2

[5] Handscomb, D. The Monte Carlo method in quantum statistical mechanics. *Math. Proc. Cambridge Philos. Soc.*, **58**(4):594. doi: 10.1017/S0305004100040639 (1962). 2

[6] Schollwöck, U. The density-matrix renormalization group. *Rev. Mod. Phys.*, **77**(1):259. doi: 10.1103/RevModPhys.77.259 (2005). 2

[7] Georges, A, Krauth, W, & Rozenberg, MJ. Dynamical mean-field theory of strongly correlated fermion systems and the limit of infinite dimensions. *Rev. Mod. Phys.*, **68**(1):13. doi: 10.1103/RevModPhys.68.13 (1996). 2

[8] Feynman, R. Simulating physics with computers. *Int. J. Theor. Phys.*, **21**(6-7):467. doi: 10.1007/BF02650179 (1982). 2

[9] Greiner, M, Mandel, O, Esslinger, T, Hänsch, TW, & Bloch, I. Quantum phase transition from a superfluid to a Mott insulator in a gas of ultracold atoms. *Nature*, **415**(6867):39. doi: 10.1038/415039a (2002). 3, 50

[10] Greiner, M, Regal, C, & Jin, D. Probing the Excitation Spectrum of a Fermi Gas in the BCS-BEC Crossover Regime. *Phys. Rev. Lett.*, **94**(7):70403. doi: 10.1103/PhysRevLett.94.070403 (2005). 3

[11] Zwierlein, MW, Abo-Shaeer, JR, Schirotzek, A, Schunck, CH, & Ketterle, W. Vortices and superfluidity in a strongly interacting Fermi gas. *Nature*, **435**(7045):1047. doi: 10.1038/nature03858 (2005). 3

[12] Struck, J, Ölschläger, C, Le Targat, R, Soltan-Panahi, P, Eckardt, A, Lewenstein, M, Windpassinger, P, & Sengstock, K. Quantum simulation of frustrated classical magnetism in triangular optical lattices. *Science*, **333**(6045):996. doi: 10.1126/science.1207239 (2011). 3

[13] Simon, J, Bakr, WS, Ma, R, Tai, ME, Preiss, PM, & Greiner, M. Quantum simulation of antiferromagnetic spin chains in an optical lattice. *Nature*, **472**(7343):307. doi: 10.1038/nature09994 (2011). 3

[14] Fallani, L, Lye, J, Guarrera, V, Fort, C, & Inguscio, M. Ultracold Atoms in a Disordered Crystal of Light: Towards a Bose Glass. *Phys. Rev. Lett.*, **98**(13):130404. doi: 10.1103/PhysRevLett.98.130404 (2007). 3

[15] Roati, G, D'Errico, C, Fallani, L, Fattori, M, Fort, C, Zaccanti, M, Modugno, G, Modugno, M, & Inguscio, M. Anderson localization of a non-interacting Bose-Einstein condensate. *Nature*, **453**(7197):895. doi: 10.1038/nature07071 (2008). 3

[16] Billy, J, Josse, V, Zuo, Z, Bernard, A, Hambrecht, B, Lugan, P, Clément, D, Sanchez-Palencia, L, Bouyer, P, & Aspect, A. Direct observation of Anderson localization of matter waves in a controlled disorder. *Nature*, **453**(7197):891. doi: 10.1038/nature07000 (2008). 3

[17] Uehlinger, T, Jotzu, G, Messer, M, Greif, D, Hofstetter, W, Bissbort, U, & Esslinger, T. Artificial Graphene with Tunable Interactions. *Phys. Rev. Lett.*, **111**(18):185307. doi: 10.1103/PhysRevLett.111.185307 (2013). 3, 37

[18] Jo, GB, Guzman, J, Thomas, CK, Hosur, P, Vishwanath, A, & Stamper-Kurn, DM. Ultracold Atoms in a Tunable Optical Kagome Lattice. *Phys. Rev. Lett.*, **108**(4):045305. doi: 10.1103/PhysRevLett.108.045305 (2012). 3

[19] Aidelsburger, M, Atala, M, Nascimbène, S, Trotzky, S, Chen, YA, & Bloch, I. Experimental realization of strong effective magnetic fields in optical superlattice potentials. *Appl. Phys. B*, **113**(1):1. doi: 10.1007/s00340-013-5418-1 (2013). 3

[20] Aidelsburger, M, Atala, M, Lohse, M, Barreiro, JT, Paredes, B, & Bloch, I. Realization of the Hofstadter Hamiltonian with Ultracold Atoms in Optical Lattices. *Phys. Rev. Lett.*, **111**(18):185301. doi: 10.1103/PhysRevLett.111.185301 (2013). 3

[21] Miyake, H, Siviloglou, GA, Kennedy, CJ, Burton, WC, & Ketterle, W. Realizing the Harper Hamiltonian with Laser-Assisted Tunneling in Optical Lattices. *Phys. Rev. Lett.*, **111**(18):185302. doi: 10.1103/PhysRevLett.111.185302 (2013). 3

[22] Lin, YJ, Compton, R, Perry, A, Phillips, W, Porto, J, & Spielman, I. Bose-Einstein Condensate in a Uniform Light-Induced Vector Potential. *Phys. Rev. Lett.*, **102**(13):130401. doi: 10.1103/PhysRevLett.102.130401 (2009). 3

[23] Lin, YJ, Jiménez-García, K, & Spielman, IB. Spin-orbit-coupled Bose-Einstein condensates. *Nature*, **471**(7336):83. doi: 10.1038/nature09887 (2011). 3

[24] Goldman, N, Kubasiak, A, Gaspard, P, & Lewenstein, M. Ultracold atomic gases in non-Abelian gauge potentials: The case of constant Wilson loop. *Phys. Rev. A*, **79**(2):023624. doi: 10.1103/PhysRevA.79.023624 (2009). 3

[25] Cooper, NR. Optical Flux Lattices for Ultracold Atomic Gases. *Phys. Rev. Lett.*, **106**(17):175301. doi: 10.1103/PhysRevLett.106.175301 (2011). 3

[26] Büchler, H, Hermele, M, Huber, S, Fisher, M, & Zoller, P. Atomic Quantum Simulator for Lattice Gauge Theories and Ring Exchange Models. *Phys. Rev. Lett.*, **95**(4):040402. doi: 10.1103/PhysRevLett.95.040402 (2005). 3

[27] Aguado, M, Brennen, G, Verstraete, F, & Cirac, J. Creation, Manipulation, and Detection of Abelian and Non-Abelian Anyons in Optical Lattices. *Phys. Rev. Lett.*, **101**(26):260501. doi: 10.1103/PhysRevLett.101.260501 (2008). 3

[28] Sau, JD, Sensarma, R, Powell, S, Spielman, IB, & Das Sarma, S. Chiral Rashba spin textures in ultracold Fermi gases. *Phys. Rev. B*, **83**(14):140510. doi: 10.1103/PhysRevB.83.140510 (2011). 3

[29] Giovanazzi, S. Hawking Radiation in Sonic Black Holes. *Phys. Rev. Lett.*, **94**(6):061302. doi: 10.1103/PhysRevLett.94.061302 (2005). 3

[30] Szpak, N & Schützhold, R. Quantum simulator for the Schwinger effect with atoms in bichromatic optical lattices. *Phys. Rev. A*, **84**(5):050101. doi: 10.1103/PhysRevA.84.050101 (2011). 3

[31] Leonhardt, U, Maia, C, & Schützhold, R. Focus on classical and quantum analogues for gravitational phenomena and related effects. *New J. Phys.*, **14**(10):105032. doi: 10.1088/1367-2630/14/10/105032 (2012). 3

[32] Georgescu, IM, Ashhab, S, & Nori, F. Quantum simulation. *Rev. Mod. Phys.*, **86**(1):153. doi: 10.1103/RevModPhys.86.153 (2014). 3

[33] Nelson, KD, Li, X, & Weiss, DS. Imaging single atoms in a three-dimensional array. *Nat. Phys.*, **3**(8):556. doi: 10.1038/nphys645 (2007). 3

[34] Gericke, T, Würtz, P, Reitz, D, Langen, T, & Ott, H. High-resolution scanning electron microscopy of an ultracold quantum gas. *Nat. Phys.*, **4**(12):949. doi: 10.1038/nphys1102 (2008). 3

[35] Bakr, WS, Peng, A, Tai, ME, Ma, R, Simon, J, Gillen, JI, Fölling, S, Pollet, L, & Greiner, M. Probing the superfluid-to-Mott insulator transition at the single-atom level. *Science*, **329**(5991):547. doi: 10.1126/science.1192368 (2010). 3, 50, 66, 137

[36] Sherson, JF, Weitenberg, C, Endres, M, Cheneau, M, Bloch, I, & Kuhr, S. Single-atom-resolved fluorescence imaging of an atomic Mott insulator. *Nature*, **467**(7311):68. doi: 10.1038/nature09378 (2010). 3, 137

[37] Weitenberg, C, Endres, M, Sherson, JF, Cheneau, M, Schauss, P, Fukuhara, T, Bloch, I, & Kuhr, S. Single-spin addressing in an atomic Mott insulator. *Nature*, **471**(7338):319. doi: 10.1038/nature09827 (2011). 3, 135

[38] Endres, M, Cheneau, M, Fukuhara, T, Weitenberg, C, Schauss, P, Gross, C, Mazza, L, Bañuls, MC, Pollet, L, Bloch, I, & Kuhr, S. Observation of correlated particle-hole pairs and string order in low-dimensional Mott insulators. *Science*, **334**(6053):200. doi: 10.1126/science.1209284 (2011). 3

[39] Cheneau, M, Barmettler, P, Poletti, D, Endres, M, Schauss, P, Fukuhara, T, Gross, C, Bloch, I, Kollath, C, & Kuhr, S. Light-cone-like spreading of correlations in a quantum many-body system. *Nature*, **481**(7382):484. doi: 10.1038/nature10748 (2012). 3

[40] Fukuhara, T, Kantian, A, Endres, M, Cheneau, M, Schauss, P, Hild, S, Bellem, D, Schollwöck, U, Giamarchi, T, Gross, C, Bloch, I, & Kuhr, S. Quantum dynamics of a mobile spin impurity. *Nat. Phys.*, **9**(4):235. doi: 10.1038/nphys2561 (2013). 3, 5

[41] Fukuhara, T, Schauss, P, Endres, M, Hild, S, Cheneau, M, Bloch, I, & Gross, C. Microscopic observation of magnon bound states and their dynamics. *Nature*, **502**(7469):76. doi: 10.1038/nature12541 (2013). 3

[42] Bakr, WS, Preiss, PM, Tai, ME, Ma, R, Simon, J, & Greiner, M. Orbital excitation blockade and algorithmic cooling in quantum gases. *Nature*, **480**(7378):500. doi: 10.1038/nature10668 (2011). 3

[43] Endres, M, Fukuhara, T, Pekker, D, Cheneau, M, Schauβ, P, Gross, C, Demler, E, Kuhr, S, & Bloch, I. The "Higgs" amplitude mode at the two-dimensional superfluid/Mott insulator transition. *Nature*, **487**(7408):454. doi: 10.1038/nature11255 (2012). 4

[44] Hubbard, J. Electron Correlations in Narrow Energy Bands. *Proc. R. Soc. A Math. Phys. Eng. Sci.*, **276**(1365):238. doi: 10.1098/rspa.1963.0204 (1963). 4, 51

[45] Lee, PA & Wen, XG. Doping a Mott insulator: Physics of high-temperature superconductivity. *Rev. Mod. Phys.*, **78**(1):17. doi: 10.1103/RevModPhys.78.17 (2006). 4

[46] Micnas, R, Ranninger, J, & Robaszkiewicz, S. Superconductivity in narrow-band systems with local nonretarded attractive interactions. *Rev. Mod. Phys.*, **62**(1):113. doi: 10.1103/RevModPhys.62.113 (1990). 4, 52

[47] Scalapino, D. The case for dx2-y2 pairing in the cuprate superconductors. *Phys. Rep.*, **250**(6):329. doi: 10.1016/0370-1573(94)00086-I (1995). 4

[48] Anderson, PW. Superconductivity in High Tc Cuprates: The Cause is No Longer A Mystery. *Phys. Scr.*, **T102**(1):10. doi: 10.1238/Physica.Topical.102a00010 (2002). 4

[49] Hofstetter, W, Cirac, J, Zoller, P, Demler, E, & Lukin, M. High-Temperature Superfluidity of Fermionic Atoms in Optical Lattices. *Phys. Rev. Lett.*, **89**(22):220407. doi: 10.1103/PhysRevLett.89.220407 (2002). 4, 53

[50] Corcovilos, TA, Baur, SK, Hitchcock, JM, Mueller, EJ, & Hulet, RG. Detecting antiferromagnetism of atoms in an optical lattice via optical Bragg scattering. *Phys. Rev. A*, **81**(1):13415. doi: 10.1103/PhysRevA.81.013415 (2010). 4, 53, 60

[51] Greif, D, Tarruell, L, Uehlinger, T, Jördens, R, & Esslinger, T. Probing Nearest-Neighbor Correlations of Ultracold Fermions in an Optical Lattice. *Phys. Rev. Lett.*, **106**(14):145302. doi: 10.1103/PhysRevLett.106.145302 (2011). 4

[52] Greif, D, Uehlinger, T, Jotzu, G, Tarruell, L, & Esslinger, T. Short-range quantum magnetism of ultracold fermions in an optical lattice. *Science*, **340**(6138):1307. doi: 10.1126/science.1236362 (2013). 4

[53] Gehm, ME. Properties of 6Li (2003). 7

[54] Arimondo, E, Inguscio, M, & Violino, P. Experimental determinations of the hyperfine structure in the alkali atoms. *Rev. Mod. Phys.*, **49**(1):31. doi: 10.1103/RevModPhys.49.31 (1977). 7

[55] Glauber, R. Coherent and Incoherent States of the Radiation Field. *Phys. Rev.*, **131**(6):2766. doi: 10.1103/PhysRev.131.2766 (1963). 10

[56] Allen, L & Eberly, JH. *Optical resonance and two-level atoms*, vol. 28. Dover Publications (1987). 10

[57] Metcalf, HJ & van der Straten, P. *Laser cooling and trapping*. Springer (1999). 11, 16, 111, 113, 115

[58] Lukin, M & Childress, L. Physics 285b. Modern Atomic and Optical Physics II. Lecture notes, Harvard University (2009). 11, 58

[59] Scully, MO & Zubairy, MS. *Quantum optics*. Cambridge University Press (1997). 11, 16, 59

[60] Safronova, MS, Safronova, UI, & Clark, CW. Magic wavelengths for optical cooling and trapping of lithium. *Phys. Rev. A*, **86**(4):042505. doi: 10.1103/PhysRevA.86.042505 (2012). 14, 67

[61] Landau, L. Zur Theorie der Energieübertragung II. *Phys. Z. Sowjet.*, (2):46 (1932). 15

[62] Zener, C. Non-Adiabatic Crossing of Energy Levels. *Proc. R. Soc. A Math. Phys. Eng. Sci.*, **137**(833):696. doi: 10.1098/rspa.1932.0165 (1932). 15

[63] Schwabl, F. *Statistical Mechanics*. Springer, 2nd editio ed. (2006). 15, 22, 24

[64] Köhler, T, Góral, K, & Julienne, P. Production of cold molecules via magnetically tunable Feshbach resonances. *Rev. Mod. Phys.*, **78**(4):1311. doi: 10.1103/RevModPhys.78.1311 (2006). 18

[65] Moerdijk, A, Verhaar, B, & Axelsson, A. Resonances in ultracold collisions of 6Li, 7Li, and 23Na. *Phys. Rev. A*, **51**(6):4852 (1995). 18

[66] Petrov, DS, Salomon, C, & Shlyapnikov, GV. Weakly Bound Dimers of Fermionic Atoms. *Phys. Rev. Lett.*, **93**(9):090404. doi: 10.1103/PhysRevLett.93.090404 (2004). 18, 19

[67] Zürn, G, Lompe, T, Wenz, AN, Jochim, S, Julienne, PS, & Hutson, JM. Precise Characterization of 6Li Feshbach Resonances Using Trap-Sideband-Resolved RF Spectroscopy of Weakly Bound Molecules. *Phys. Rev. Lett.*, **110**(13):135301. doi: 10.1103/PhysRevLett.110.135301 (2013). 19

[68] Ottenstein, T, Lompe, T, Kohnen, M, Wenz, A, & Jochim, S. Collisional Stability of a Three-Component Degenerate Fermi Gas. *Phys. Rev. Lett.*, **101**(20):203202. doi: 10.1103/PhysRevLett.101.203202 (2008). 19

[69] Strecker, KE, Partridge, GB, & Hulet, RG. Conversion of an Atomic Fermi Gas to a Long-Lived Molecular Bose Gas. *Phys. Rev. Lett.*, **91**(8):080406. doi: 10.1103/PhysRevLett.91.080406 (2003). 19

[70] O'Hara, KM, Hemmer, SL, Granade, SR, Gehm, ME, & Thomas, JE. Measurement of the zero crossing in a Feshbach resonance of fermionic 6Li. *Phys. Rev. A*, **66**(4):1. doi: 10.1103/PhysRevA.66.041401 (2002). 19

[71] Du, X, Luo, L, Clancy, B, & Thomas, JE. Observation of Anomalous Spin Segregation in a Trapped Fermi Gas. *Phys. Rev. Lett.*, **101**(15):150401. doi: 10.1103/PhysRevLett.101.150401 (2008). 19

[72] Dürr, S, Volz, T, Marte, A, & Rempe, G. Observation of Molecules Produced from a Bose-Einstein Condensate. *Phys. Rev. Lett.*, **92**(2):020406. doi: 10.1103/PhysRevLett.92.020406 (2004). 19

[73] Olshanii, M. Atomic Scattering in the Presence of an External Confinement and a Gas of Impenetrable Bosons. *Phys. Rev. Lett.*, **81**(5):938. doi: 10.1103/PhysRevLett.81.938 (1998). 20

[74] Dickerscheid, D & Stoof, H. Feshbach molecules in a one-dimensional Fermi gas. *Phys. Rev. A*, **72**(5):053625. doi: 10.1103/PhysRevA.72.053625 (2005). 20

[75] Moritz, H, Stöferle, T, Günter, K, Köhl, M, & Esslinger, T. Confinement Induced Molecules in a 1D Fermi Gas. *Phys. Rev. Lett.*, **94**(21):210401. doi: 10.1103/PhysRevLett.94.210401 (2005). 20

[76] Haller, E, Mark, MJ, Hart, R, Danzl, JG, Reichsöllner, L, Melezhik, V, Schmelcher, P, & Nägerl, HC. Confinement-Induced Resonances in Low-Dimensional Quantum Systems. *Phys. Rev. Lett.*, **104**(15):153203. doi: 10.1103/PhysRevLett.104.153203 (2010). 20

[77] Busch, T, Englert, B, Rzażewski, K, & Wilkens, M. Two Cold Atoms in a Harmonic Trap. *Found. Phys.*, **28**(4):549 (1998). 20

[78] Stöferle, T, Moritz, H, Günter, K, Köhl, M, & Esslinger, T. Molecules of Fermionic Atoms in an Optical Lattice. *Phys. Rev. Lett.*, **96**(3):030401. doi: 10.1103/PhysRevLett.96.030401 (2006). 20

[79] Dickerscheid, D, Al Khawaja, U, van Oosten, D, & Stoof, H. Feshbach resonances in an optical lattice. *Phys. Rev. A*, **71**(4):043604. doi: 10.1103/PhysRevA.71.043604 (2005). 20

[80] Gubbels, KB, Dickerscheid, DBM, & Stoof, HTC. Dressed molecules in an optical lattice. *New J. Phys.*, **8**(8):151 (2006). 20

[81] Sakurai, JJ & Tuan, SF. *Modern quantum mechanics*, vol. 104. Addison-Wesley Reading (1994). 20, 54

[82] Abramowitz, M & Stegun, IA. *Handbook of Mathematical Functions with Formulas, Graphs, and Mathematical Tables*. Dover, New York (1964). 21, 23, 29, 57

[83] Butts, Da & Rokhsar, DS. Trapped Fermi gases. *Phys. Rev. A*, **55**(6):4346. doi: 10.1103/PhysRevA.55.4346 (1997). 22, 24, 25

[84] Ketterle, W & Zwierlein, MW. Making, probing and understanding ultracold Fermi gases. *Riv. del Nuovo Cim.*, **31**(5):247. doi: 10.1393/ncr/i2008-10033-1 (2008). 22

[85] Ketterle, W, Durfee, DS, & Stamper-Kurn, DM. Making, probing and understanding Bose-Einstein condensates. In Inguscio, M, Stringari, S, & Wieman, CE (eds.), *Bose-Einstein Condens. At. gases*. Varenna (1999). 26, 100

[86] Saleh, BEA & Teich, MC. *Fundamentals of photonics*, vol. 22. Wiley New York (1991). 26, 78, 92, 93, 99, 107, 153

[87] Lasers and laser-related equipment – Test methods for laser beam widths, divergence angles and beam propagation ratios. Norm ISO 11146 (2005). 29, 30

[88] Chu, S, Bjorkholm, J, Ashkin, A, & Cable, A. Experimental Observation of Optically Trapped Atoms. *Phys. Rev. Lett.*, **57**(3):314. doi: 10.1103/PhysRevLett.57.314 (1986). 31

[89] Grimm, R, Weidemüller, M, & Ovchinnikov, Y. Optical dipole traps for neutral atoms. *Adv. At. Mol. Opt. Phys.*, **42**:95. doi: 10.1016/S1049-250X(08)60186-X (2000). 31, 33

[90] Davidson, N, Jin Lee, H, Adams, C, Kasevich, M, & Chu, S. Long Atomic Coherence Times in an Optical Dipole Trap. *Phys. Rev. Lett.*, **74**(8):1311. doi: 10.1103/PhysRevLett.74.1311 (1995). 32

[91] Kuga, T, Torii, Y, Shiokawa, N, Hirano, T, Shimizu, Y, & Sasada, H. Novel Optical Trap of Atoms with a Doughnut Beam. *Phys. Rev. Lett.*, **78**(25):4713. doi: 10.1103/PhysRevLett.78.4713 (1997). 32

[92] Friedman, N, Khaykovich, L, Ozeri, R, & Davidson, N. Single-Beam Dark Optical Traps for Cold Atoms. *Opt. Photon. News*, **10**(12):36. doi: 10.1364/OPN.10.12.000036 (1999). 32

[93] Adams, C, Lee, H, Davidson, N, Kasevich, M, & Chu, S. Evaporative Cooling in a Crossed Dipole Trap. *Phys. Rev. Lett.*, **74**(18):3577. doi: 10.1103/PhysRevLett.74.3577 (1995). 32

[94] Jackson, JD. *Classical Electrodynamics*. Wiley, third ed. (1998). 34

[95] Savard, T, O'Hara, K, & Thomas, J. Laser-noise-induced heating in far-off resonance optical traps. *Phys. Rev. A*, **56**(2):1095. doi: 10.1103/PhysRevA.56.R1095 (1997). 39

[96] Gehm, M, Savard, T, & Thomas, J. Dynamics of noise-induced heating in atom traps. *Phys. Rev. A*, **58**(5):3914. doi: 10.1103/PhysRevA.58.3914 (1998). 39

[97] Zhu, M & Hall, JL. Stabilization of optical phase/frequency of a laser system: application to a commercial dye laser with an external stabilizer. *J. Opt. Soc. Am. B*, **10**(5):802. doi: 10.1364/JOSAB.10.000802 (1993). 40

[98] Ashcroft, NW & Mermin, ND. Solid State Physics. *Rinehart Winston, New York*, **19761** (1976). 41

[99] Sigrist, M. Solid State Theory. Lecture notes, ETH Zürich (2013). 47

[100] Setiawan, W. Fermi Gas Microscope. Phd thesis, Harvard University (2012). 48, 67, 75, 79, 80, 81, 83, 117, 119, 125, 127, 128, 137

[101] Bloch, I & Zwerger, W. Many-body physics with ultracold gases. *Rev. Mod. Phys.*, **80**(3):885. doi: 10.1103/RevModPhys.80.885 (2008). 48, 102

[102] Greiner, M. Ultracold quantum gases in three-dimensional optical lattice potentials. Phd thesis, Ludwig-Maximilians-Universität Muünchen (2003). 48

[103] Jaksch, D, Bruder, C, Cirac, JI, Gardiner, CW, & Zoller, P. Cold Bosonic Atoms in Optical Lattices. *Phys. Rev. Lett.*, **81**(15):3108. doi: 10.1103/PhysRevLett.81.3108 (1998). 49, 50, 51

[104] Gemelke, N, Zhang, X, Hung, Cl, & Chin, C. In situ observation of incompressible Mott-insulating domains in ultracold atomic gases. *Nature*, **460**(7258):995. doi: 10.1038/nature08244 (2009). 50

[105] Georges, A. Condensed-matter physics with light and atoms: Strongly correlated cold fermions in optical lattices. In Inguscio, M, Ketterle, W, & Salomon, C (eds.), *Ultra-cold Fermi gases*. Varenna (2007). 51

[106] Ma, R. Engineered Potentials and Dynamics Of Ultracold Quantum Gases Under The Microscope. Phd thesis, Harvard University (2014). 51

[107] Esslinger, T. Fermi-Hubbard Physics with Atoms in an Optical Lattice. *Annu. Rev. Condens. Matter Phys.*, **1**(1):129. doi: 10.1146/annurev-conmatphys-070909-104059 (2010). 52

[108] Ho, a, Cazalilla, M, & Giamarchi, T. Quantum simulation of the Hubbard model: The attractive route. *Phys. Rev. A*, **79**(3):1. doi: 10.1103/PhysRevA.79.033620 (2009). 52

[109] Jordens, R, Strohmaier, N, Gunter, K, Moritz, H, Esslinger, T, Jördens, R, & Günter, K. A Mott insulator of fermionic atoms in an optical lattice. *Nature*, **455**(7210):204. doi: 10.1038/nature07244 (2008). 53

[110] Schneider, U, Hackermüller, L, Will, S, Best, T, Bloch, I, Costi, TA, Helmes, RW, Rasch, D, Rosch, A, & Hackermuller, L. Metallic and insulating phases of repulsively interacting fermions in a 3D optical lattice. *Science*, **322**(5907):1520. doi: 10.1126/science.1165449 (2008). 53, 133

[111] Mathy, C & Huse, D. Accessing the Néel phase of ultracold fermionic atoms in a simple-cubic optical lattice. *Phys. Rev. A*, **79**(6):063412. doi: 10.1103/PhysRevA.79.063412 (2009). 53

[112] Strohmaier, N, Greif, D, Joerdens, R, Tarruell, L, Moritz, H, & Esslinger, T. Observation of Elastic Doublon Decay in the Fermi-Hubbard Model. *Phys. Rev. Lett.*, **104**(8):1. doi: 10.1103/PhysRevLett.104.080401 (2010). 53, 60

[113] Duan, LM, Demler, E, & Lukin, M. Controlling Spin Exchange Interactions of Ultracold Atoms in Optical Lattices. *Phys. Rev. Lett.*, **91**(9):090402. doi: 10.1103/PhysRevLett.91.090402 (2003). 54

[114] Dalibard, J & Cohen-Tannoudji, C. Laser cooling below the Doppler limit by polarization gradients: simple theoretical models. *J. Opt. Soc. Am. B*, **6**(11):2023. doi: 10.1364/JOSAB.6.002023 (1989). 55

[115] Cohen-Tannoudji, C, Dupont-Roc, J, & Grynberg, G. *Atom—photon Interactions*. Wiley-VCH Verlag GmbH. doi: 10.1002/9783527617197.ch5 (2008). 55

[116] Stellmer, S, Pasquiou, B, Grimm, R, & Schreck, F. Laser Cooling to Quantum Degeneracy. *Phys. Rev. Lett.*, **110**(26):263003. doi: 10.1103/PhysRevLett.110.263003 (2013). 55

[117] Monroe, C, Meekhof, D, King, B, Jefferts, S, Itano, W, Wineland, D, & Gould, P. Resolved-Sideband Raman Cooling of a Bound Atom to the 3D Zero-Point Energy. *Phys. Rev. Lett.*, **75**(22):4011. doi: 10.1103/PhysRevLett.75.4011 (1995). 55

[118] Wineland, D & Itano, W. Laser Cooling of Atoms. *Phys. Rev. A*, **20**(4):1521 (1979). 56

[119] Kerman, AJ. Raman Sideband Cooling and Cold Atomic Collisions in Optical Lattices. Phd thesis, Stanford University (2002). 57

[120] Cohen-Tannoudji, C & Reynaud, S. Dressed-atom description of resonance fluorescence and absorption spectra of a multi-level atom in an intense laser beam. *J. Phys. B At. Mol. Phys.*, **10**(3):345. doi: 10.1088/0022-3700/10/3/005 (1977). 59

[121] Mollow, B. Power Spectrum of Light Scattered by Two-Level Systems. *Phys. Rev.*, **188**(5):1969. doi: 10.1103/PhysRev.188.1969 (1969). 59

[122] Grove, RE, Wu, FY, & Ezekiel, S. Measurement of the spectrum of resonance fluorescence from a two-level atom in an intense monochromatic field. *Phys. Rev. A*, **15**(1):227. doi: 10.1103/PhysRevA.15.227 (1977). 59

[123] Berman, P. Light scattering. *Contemp. Phys.*, **49**(5):313. doi: doi:10.1080/00107510802551572 (2008). 60

[124] Weitenberg, C, Schauss, P, Fukuhara, T, Cheneau, M, Endres, M, Bloch, I, Kuhr, S, & Schauss, P. Coherent Light Scattering from a Two-Dimensional Mott Insulator. *Phys. Rev. Lett.*, **106**(21):215301. doi: 10.1103/PhysRevLett.106.215301 (2011). 60

[125] Hamann, S, Haycock, D, Klose, G, Pax, P, Deutsch, I, & Jessen, P. Resolved-Sideband Raman Cooling to the Ground State of an Optical Lattice. *Phys. Rev. Lett.*, **80**(19):4149. doi: 10.1103/PhysRevLett.80.4149 (1998). 60

[126] Han, DJ, Wolf, S, Oliver, S, McCormick, C, DePue, MT, & Weiss, DS. 3D Raman Sideband Cooling of Cesium Atoms at High Density. *Phys. Rev. Lett.*, **85**(4):724. doi: 10.1103/PhysRevLett.85.724 (2000). 60

[127] Kerman, A, Vuletic, V, Chin, C, & Chu, S. Beyond optical molasses: 3D raman sideband cooling of atomic cesium to high phase-space density. *Phys. Rev. Lett.*, **84**(3):439 (2000). 60

[128] Vuletić, V, Chin, C, Kerman, A, & Chu, S. Degenerate Raman Sideband Cooling of Trapped Cesium Atoms at Very High Atomic Densities. *Phys. Rev. Lett.*, **81**(26):5768. doi: 10.1103/PhysRevLett.81.5768 (1998). 60

[129] Perrin, H, Kuhn, a, Bouchoule, I, & Salomon, C. Sideband cooling of neutral atoms in a far-detuned optical lattice. *Europhys. Lett.*, **42**(4):395. doi: 10.1209/epl/i1998-00261-y (1998). 60

[130] Weiner, J & Julienne, PS. Experiments and theory in cold and ultracold collisions. *Rev. Mod. Phys.*, **71**(1):1. doi: 10.1103/RevModPhys.71.1 (1999). 65, 66

[131] Gallagher, A & Pritchard, D. Exoergic collisions of cold Na*-Na. *Phys. Rev. Lett.*, **63**(9):957. doi: 10.1103/PhysRevLett.63.957 (1989). 65

[132] Wei, R & Mueller, EJ. Magnetic-field dependence of Raman coupling in alkali-metal atoms. *Phys. Rev. A*, **87**(4):042514. doi: 10.1103/PhysRevA.87.042514 (2013). 66

[133] O'Hanlon, JF. *A User's Guide to Vacuum Technology*. John Wiley & Sons (2005). 76

[134] Huber, F. A Novel Apparatus for Experiments with Ultracold Fermions. Diploma thesis, Technical University of Munich (2009). 77, 112, 113

[135] Altemose, VO. Helium Diffusion through Glass. *J. Appl. Phys.*, **32**(7):1309. doi: 10.1063/1.1736226 (1961). 77

[136] Schuster, T. A Novel Apparatus for Experiments with Ultracold Sodium and Lithium. Diploma thesis, Harvard University/University of Heidelberg (2008). 79

[137] Jaatinen, E & Brown, N. A simple external iodine stabilizer applied to 633 nm, 612 nm and 543 nm He-Ne lasers. *Metrologia*, **32**(2):95 (1995). 79

[138] Mosk, A, Jochim, S, Moritz, H, Elsässer, T, Weidemüller, M, & Grimm, R. Resonator-enhanced optical dipole trap for fermionic lithium atoms. *Opt. Lett.*, **26**(23):1837. doi: 10.1364/OL.26.001837 (2001). 80

[139] Mansell, JD, Hennawi, J, Gustafson, EK, Fejer, MM, Byer, RL, Clubley, D, Yoshida, S, & Reitze, DH. Evaluating the effect of transmissive optic thermal lensing on laser beam quality with a shack-hartmann wave-front sensor. *Appl. Opt.*, **40**(3):366 (2001). 81, 89

[140] Khazanov, E, Andreev, N, Mal'shakov, A, Palashov, O, Poteomkin, A, Sergeev, A, Shaykin, A, Zelenogorsky, V, Ivanov, I, Amin, R, Mueller, G, Tanner, D, & Reitze, D. Compensation of thermally induced modal distortions in Faraday isolators. *IEEE J. Quantum Electron.*, **40**(10):1500. doi: 10.1109/JQE.2004.834766 (2004). 90

[141] David, A & Horowitz, M. Low-frequency transmitted intensity noise induced by stimulated Brillouin scattering in optical fibers. *Opt. Express*, **19**(12):11792 (2011). 90

[142] Mansfield, SM & Kino, GS. Solid immersion microscope. *Appl. Phys. Lett.*, **57**(24):2615. doi: 10.1063/1.103828 (1990). 93

[143] Tong, QY & Goesele, U. *Semiconductor Wafer Bonding: Science and Technology*. John Wiley New York (1999). 95, 96

[144] Born, M & Wolf, E. *Principles of optics: electromagnetic theory of propagation, interference and diffraction of light*. Cambridge University Press, 7th expand ed. (1999). 99, 107

[145] Smith, Da, Aigner, S, Hofferberth, S, Gring, M, Andersson, M, Wildermuth, S, Krüger, P, Schneider, S, Schumm, T, & Schmiedmayer, J. Absorption imaging of ultracold atoms on atom chips. *Opt. Express*, **19**(9):8471 (2011). 101

[146] Campbell, GK. Rubidium Bose-Einstein Condensates in Optical Lattices. Phd thesis, Massachussets Institute of Technology (2006). 104

[147] Weber, T, Herbig, J, Mark, M, Nägerl, HC, & Grimm, R. Bose-Einstein condensation of cesium. *Science*, **299**(5604):232. doi: 10.1126/science.1079699 (2003). 108

[148] Serwane, F, Zürn, G, Lompe, T, Ottenstein, TB, Wenz, AN, & Jochim, S. Deterministic preparation of a tunable few-fermion system. *Science*, **332**(6027):336. doi: 10.1126/science.1201351 (2011). 108, 133

[149] Gustavson, TL, Chikkatur, AP, Leanhardt, AE, Görlitz, A, Gupta, S, Pritchard, DE, & Ketterle, W. Transport of Bose-Einstein Condensates with Optical Tweezers. *Phys. Rev. Lett.*, **88**(2):20401. doi: 10.1103/PhysRevLett.88.020401 (2001). 110

[150] Stan, Ca & Ketterle, W. Multiple species atom source for laser-cooling experiments. *Rev. Sci. Instrum.*, **76**(6):63113. doi: 10.1063/1.1935433 (2005). 111

[151] Nesmeyanov, AN. *Vapor pressure of the chemical elements*. North-Holland, Amsterdam (1963). 111

[152] Naik, DE. Bose-Einstein Condensation: Building the Testbeds to Study Superfluidity. Phd thesis, Georgia Institute of Technology (2006). 112

[153] Raab, E, Prentiss, M, Cable, A, Chu, S, & Pritchard, D. Trapping of Neutral Sodium Atoms with Radiation Pressure. *Phys. Rev. Lett.*, **59**(23):2631. doi: 10.1103/PhysRevLett.59.2631 (1987). 113

[154] Rio Fernandes, D, Sievers, F, Kretzschmar, N, Wu, S, Salomon, C, & Chevy, F. Sub-Doppler laser cooling of fermionic 40 K atoms in three-dimensional gray optical molasses. *Europhys. Lett.*, **100**(6):63001. doi: 10.1209/0295-5075/100/63001 (2012). 115

[155] Grier, AT, Ferrier-Barbut, I, Rem, BS, Delehaye, M, Khaykovich, L, Chevy, F, & Salomon, C. Λ-enhanced sub-Doppler cooling of lithium atoms in D_{1} gray molasses. *Phys. Rev. A*, **87**(6):063411. doi: 10.1103/PhysRevA.87.063411 (2013). 115

[156] Hamilton, P, Kim, G, Joshi, T, Mukherjee, B, Tiarks, D, & Müller, H. Sisyphus cooling of lithium. *Phys. Rev. A*, **89**(2):023409. doi: 10.1103/PhysRevA.89.023409 (2014). 115

[157] Duarte, PM, Hart, Ra, Hitchcock, JM, Corcovilos, Ta, Yang, TL, Reed, a, & Hulet, RG. All-optical production of a lithium quantum gas using narrow-line laser cooling. *Phys. Rev. A*, **84**(6):061406. doi: 10.1103/PhysRevA.84.061406 (2011). 115

[158] Luiten, O, Reynolds, M, & Walraven, J. Kinetic theory of the evaporative cooling of a trapped gas. *Phys. Rev. A*, **53**(1):381 (1996). 116

[159] Luo, L, Clancy, B, Joseph, J, Kinast, J, Turlapov, A, & Thomas, JE. Evaporative cooling of unitary Fermi gas mixtures in optical traps. *New J. Phys.*, **8**(9):213. doi: 10.1088/1367-2630/8/9/213 (2006). 116, 117

[160] Anderson, MH, Ensher, JR, Matthews, MR, Wieman, CE, & Cornell, EA. Observation of bose-einstein condensation in a dilute atomic vapor. *Science*, **269**(5221):198. doi: 10.1126/science.269.5221.198 (1995). 116

[161] O'Hara, KM. Optical Trapping and Evaporative Cooling of Fermionic Atoms. Phd thesis, Duke University (2000). 117

[162] O'Hara, K, Gehm, M, Granade, S, & Thomas, J. Scaling laws for evaporative cooling in time-dependent optical traps. *Phys. Rev. A*, **64**(5):1. doi: 10.1103/PhysRevA.64.051403 (2001). 117

[163] Williams, JR. Universal Few-Body Physics In A Three-Component Fermi Gas. Phd thesis, Pennsylvania State University (2010). 117

[164] Postel, J. User Datagram Protocol. Tech. rep., Information Sciences Institute (1980). 127

[165] The HDF Group. Hierarchical Data Format, version 5 (1997). 129

[166] Oliphant, TE. Python for scientific computing. *Comput. Sci. Eng.*, **10**(2007):9. doi: 10.1109/MCSE.2007.58 (2007). 129

[167] Hunter, JD. Matplotlib: A 2D Graphics Environment. *Comput. Sci. Eng.*, **9**(3):90. doi: 10.1109/MCSE.2007.55 (2007). 129

[168] Werner, F, Parcollet, O, Georges, A, & Hassan, S. Interaction-Induced Adiabatic Cooling and Antiferromagnetism of Cold Fermions in Optical Lattices. *Phys. Rev. Lett.*, **95**(5):056401. doi: 10.1103/PhysRevLett.95.056401 (2005). 133

[169] Bernier, JS, Kollath, C, Georges, A, De Leo, L, Gerbier, F, Salomon, C, & Köhl, M. Cooling fermionic atoms in optical lattices by shaping the confinement. *Phys. Rev. A*, **79**(6):1. doi: 10.1103/PhysRevA.79.061601 (2009). 134

[170] Rey, AM, Sensarma, R, Fölling, S, Greiner, M, Demler, E, & Lukin, MD. Controlled preparation and detection of d-wave superfluidity in two-dimensional optical superlattices. *EPL (Europhysics Lett.*, **87**(6):60001. doi: 10.1209/0295-5075/87/60001 (2009). 134

[171] Jané, E, Vidal, G, Dür, W, Zoller, P, & Cirac, J. Simulation of quantum dynamics with quantum optical systems. *Quantum Inf. Comput.*, **3**(1):15 (2003). 134

[172] Trotter, HF. On the product of semi-groups of operators. *Proc. Am. Math. Soc.*, **10**(4):545. doi: 10.1090/S0002-9939-1959-0108732-6 (1959). 134

[173] Suzuki, M. Generalized Trotter's formula and systematic approximants of exponential operators and inner derivations with applications to many-body problems. *Commun. Math. Phys.*, **51**(2):183. doi: 10.1007/BF01609348 (1976). 134

[174] Deutsch, D, Barenco, A, & Ekert, A. Universality in Quantum Computation. *Proc. R. Soc. London. Ser. A Math. Phys. Sci.*, **449**(1937):669. doi: 10.1098/rspa.1995.0065 (1995). 134

[175] Nielsen, MA & Chuang, IL. *Quantum computation and quantum information*. Cambridge University Press (2010). 134

[176] Zupancic, P. Dynamic Holography and Beamshaping using Digital Micromirror Devices. Master's thesis, Harvard University (2013). 135

[177] Karski, M, Förster, L, Choi, JM, Steffen, A, Belmechri, N, Alt, W, Meschede, D, & Widera, A. Imprinting patterns of neutral atoms in an optical lattice using magnetic resonance techniques. *New J. Phys.*, **12**(6):065027. doi: 10.1088/1367-2630/12/6/065027 (2010). 135

[178] Lanyon, BP, Hempel, C, Nigg, D, Müller, M, Gerritsma, R, Zähringer, F, Schindler, P, Barreiro, JT, Rambach, M, Kirchmair, G, Hennrich, M, Zoller, P, Blatt, R, & Roos, CF. Universal digital quantum simulation with trapped ions. *Science*, **334**(6052):57. doi: 10.1126/science.1208001 (2011). 137

[179] Henkel, F, Krug, M, Hofmann, J, Rosenfeld, W, Weber, M, & Weinfurter, H. Highly Efficient State-Selective Submicrosecond Photoionization Detection of Single Atoms. *Phys. Rev. Lett.*, **105**(25):253001. doi: 10.1103/PhysRevLett.105.253001 (2010). 137

Appendix A

Transfer Matrix Method In Optics

The *transfer matrix method* is a useful tool to simulate beam propagation through cylindrically symmetric, on-axis, and paraxial optical systems. Each optical component is represented as a real 2×2 matrix of the form

$$\mathcal{M} = \begin{pmatrix} A & B \\ C & D \end{pmatrix}. \tag{A.1}$$

Because of this parameterization this method is often also called *ABCD matrix method*.

A.1 Geometric Optics

In geometric optics the propagation of a light ray in an uniform medium is simply described by a line. Therefore for a given point z_0 along the optical axis of an optical system the ray can be fully described by two conjugate variables, its angle with respect to the optical axis $\theta(z_0)$ and its distance from the optical axis. The latter corresponds to the real space, while the first describes the ray properties in Fourier space. Those two parameters can be conveniently written in the form of a *ray vector*

$$\mathbf{r}(z_0) = \begin{pmatrix} x(z_0) \\ \theta(z_0) \end{pmatrix}. \tag{A.2}$$

Free-space propagation over the distance z along the optical axis does not alter the

angle, only the offset increases linearly to $x(z_0 + z) = x(z_0) + z \sin\theta(z_0)$. In the paraxial approximation ($\sin\theta \approx \theta$) this transformation can be written as a 2×2 matrix of the following form

$$\mathcal{T}_z = \begin{pmatrix} 1 & z \\ 0 & 1 \end{pmatrix}, \tag{A.3}$$

such that

$$\mathbf{r}(z_0 + z) = \mathcal{T}_z \mathbf{r}(z_0).$$

In a similar fashion one can derive the transfer matrix for refraction on a flat interface going from an index of refraction of n_1 to n_2

$$\mathcal{F}_{n_1 \to n_2} = \begin{pmatrix} 1 & 0 \\ 0 & \frac{n1}{n2} \end{pmatrix} \tag{A.4}$$

and on a curved interface with radius of curvature R

$$\mathcal{C}_{n_1 \to n_2, R} = \begin{pmatrix} 1 & 0 \\ \frac{1}{R}\frac{n_1 - n_2}{n_2} & \frac{n1}{n2} \end{pmatrix}. \tag{A.5}$$

A thin lens with folcal length f can be modelled as two curved interfaces with opposite radius of curvature $R_2 = -R_1$. Using the lens maker's equation [86]

$$\frac{1}{f} = (n-1)\left(\frac{1}{R_1} - \frac{1}{R_2}\right) \tag{A.6}$$

one can derive the transfer matrix for a thin lens

$$\mathcal{L}_f = \begin{pmatrix} 1 & 0 \\ -\frac{1}{f} & 1 \end{pmatrix}. \tag{A.7}$$

A.2 Gaussian Optics

Although the transfer matrices above where derived for ray optics, they still can be used to calculate the propagation of Gaussian beams. The complex amplitude of a Gaussian beam

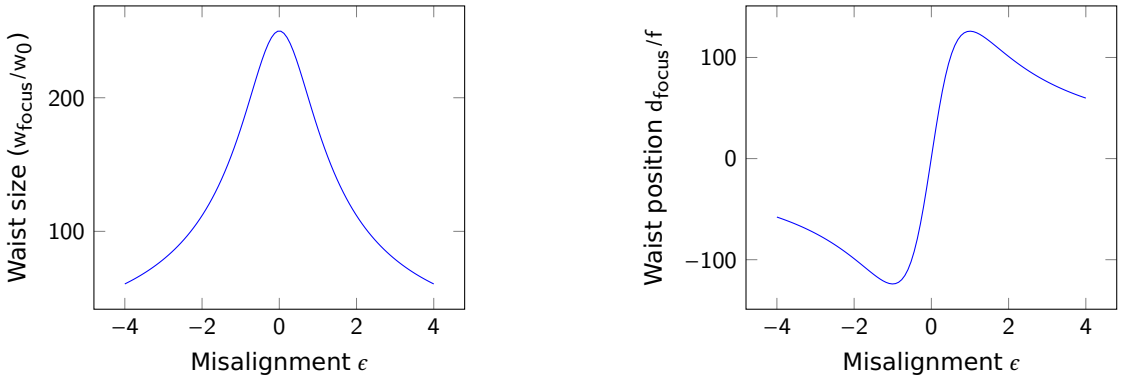

Figure A.1: Collimating a beam with a lens $f = 250 z_R$

(see (1.62)) can also be defined as

$$E(r,z) = \frac{1}{\sqrt{q(z)}} \exp\left(-\frac{i}{2} k \frac{r^2}{q^2(z)}\right), \tag{A.8}$$

where the *complex beam parameter* is given by

$$\frac{1}{q(z)} = \frac{1}{R(z)} - i\frac{\lambda}{\pi w^2(z)}. \tag{A.9}$$

For a given $ABCD$ matrix the beam parameter transforms as

$$q'(z) = \frac{A + \frac{B}{q}}{C + \frac{D}{q}}. \tag{A.10}$$

A.2.1 Example: Fiber collimation

In this section I want to demonstrate the transfer matrix method on a topic that often leads to some confusion: collimating the output of an optical fiber. Consider a single mode optical fiber, which emits a Gaussian beam with a waist at the fiber tip of w_0. Fiber manufacturers typically specify the (wavelength dependent) *mode field diameter*, which is equal to twice the Gaussian beam waist. Alternatively the beam parameters can be calculated from the fiber's numerical aperture, which is identical to the far-field divergence (1.67):

$$w_0 = \frac{\lambda}{\pi \mathrm{NA}} \qquad\qquad z_R = \frac{\lambda}{\pi \mathrm{NA}^2}.$$

Most Nufern/Thorlabs fibers have a numerical aperture of about 0.12.

To collimate the diverging beam from the fiber a single lens with focal length f is placed $d = f + \epsilon z_R$ away from the fiber tip. After the lens the beam is propagating in free space for a distance z. The resulting transfer matrix is then given by

$$\mathcal{S} = \mathcal{T}_z \mathcal{L}_f \mathcal{T}_{f+\epsilon z_R} = \begin{pmatrix} 1 - \frac{z}{f} & \frac{f-z}{f} z_R \epsilon \\ -\frac{1}{f} & -\frac{z_R}{f}\epsilon \end{pmatrix}.$$

Right after the collimation lens ($z = 0$) the Gaussian beam radius only depends weakly on the misalignment ϵ

$$w(z=0) = w_0 \sqrt{1 + \left(\frac{f}{z_R} + \epsilon\right)^2} \approx \frac{f w_0}{z_R} + \epsilon w_0 + \mathcal{O}(z_R) + \mathcal{O}(\epsilon^2).$$

But the location of the minimum Gaussian waist (i.e. the focus/the point where the beam is collimated)

$$d_{\text{focus}} = f\left(1 + \frac{f}{z_R}\frac{\epsilon}{1+\epsilon^2}\right) \tag{A.11}$$

has a stronger dependence on the misalignment ϵ. For typical collimation setups $f/z_R \sim 250$. Furthermore the minimum Gaussian waist size

$$w_{\text{focus}} = \frac{f}{z_R}\frac{w_0}{\sqrt{1+\epsilon^2}}$$

even scales $\mathcal{O}(\epsilon^2)$ for small misalignments with a large prefactor of f/z_R.

From (A.11) one can see that there is a *maximum* focusing distance given by

$$d_{\max} = f\left(\frac{f}{z_R} + 1\right) \tag{A.12}$$

at misalignment of

$$\epsilon_{\max} = \pm 1.$$

Therefore it is not possible to collimate a Gaussian beam by trying to "focus" it at at infinity (i.e. "far away"). This procedure would result in a focussed beam at a distance from the focusing lens given by (A.12) and a Gaussian beam waist that is $\sqrt{1/2}$ times the waist one would naively expect. The only consistent method to collimate a Gaussian beam is to focus

at the collimation lens. This is best done interferometrically with a shearing interferometer or iterativley with a beam profiler.